การศึกษาดาวนิวตรอนที่มีมวลมากโดยมีแกนกลางเป็นโฮโลกราฟิกมัลติควาร์ก

นายสิทธิชัย ปิ่นกาญจนโรจน์

A STUDY OF MASSIVE NEUTRON STARS WITH HOLOGRAPHIC MULTIQUARK
CORES

Mr. Sitthichai Pinkanjanarod

A Dissertation Submitted in Partial Fulfillment of the Requirements
for the Degree of Doctor of Science Program in Physics
Department of Physics
Faculty of Science
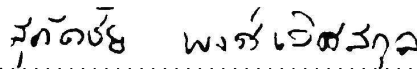Chulalongkorn University
Academic Year 2021

Thesis Title   A STUDY OF MASSIVE NEUTRON STARS WITH HOLOGRAPHIC
                  MULTIQUARK CORES
By   Mr. Sitthichai Pinkanjanarod
Field of Study   Physics
Thesis Advisor   Associate Professor Piyabut Burikham, Ph.D.

_____

        Accepted by the Faculty of Science, Chulalongkorn University in Partial Fulfillment of
the Requirements for the Doctoral Degree

        .... Dean of the Faculty of Science
        (Professor Polkit Sangvanich, Ph.D.)

THESIS COMMITTEE

        .... Chairman
        (Supakchai Ponglertsakul, Ph.D.)

        .... Thesis Advisor
        (Associate Professor Piyabut Burikham, Ph.D.)

        .... Examiner
        (Associate Professor Udomsilp Pinsook, Ph.D.)
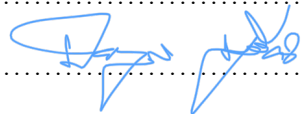
        .... Examiner
        (Assistant Professor Pawin Ittisamai, Ph.D.)

        .... Examiner
        (Thiparat Chotibut, Ph.D.)

สิทธิชัย ปิ่นกาญจนโรจน์ : การศึกษาดาวนิวตรอนที่มีมวลมากโดยมีแกนกลางเป็นโฮโลกราฟิกมัลติ
ควาร์ก. (A STUDY OF MASSIVE NEUTRON STARS WITH HOLOGRAPHIC MULTIQUARK
CORES) อ.ที่ปรึกษาวิทยานิพนธ์ : รศ. ดร.ปิยบุตร บุรีคำ 108 หน้า.

ปัจจุบันยังคงไม่มีความชัดเจนเกี่ยวกับสถานะของสสารภายในใจกลางดาวนิวตรอนที่มีมวลมาก มี
ความเป็นไปได้ว่าภายในแกนกลางของดาวนิวตรอนที่มีมวลมากนั้น ความหนาแน่นและความดันภายในดาว
มีค่ามหาศาลจนกระทั่งสสารภายในดาวอยู่ในสถานะไม่กักขังเช่นสถานะควาร์ก-กลูออนพลาสมา ไม่นาน
มานี้ ผลการวิเคราะห์จากงานวิจัย [1] ที่ทำการพิจารณาคำนวณการรบกวนทางทฤษฎีร่วมกับการใช้ข้อมูล
จากการสังเกต [2, 3] แสดงให้เห็นว่ามีความเป็นไปได้ที่สสารซึ่งมีควาร์กเป็นองค์ประกอบจะอยู่ในใจกลาง
ของดาวนิวตรอนที่มีมวลมากกว่า 2.0 $M_\odot$ อย่างไรก็ตาม สถานะควาร์ก-กลูออนพลาสมามีอยู่ได้ที่อุณหภูมิ
สูงมากๆเท่านั้น หากเทียบกันแล้ว อุณหภูมิของดาวนิวตรอนจะมีค่าต่ำกว่ามาก และเป็นไปได้ว่าสถานะใน
ใจกลางของดาวนิวตรอนที่มีมวลมากนั้นไม่ได้อยู่ในสถานะของควาร์ก-กลูออนพลาสมา แต่จะอยู่ในรูปขอ
งมัลติควาร์กซึ่งไม่ถูกกักขัง และมีการเสียสมมาตรไครัล ปัญหาสำคัญประการหนึ่งคือเราไม่สามารถพิจารณา
สถานะของมัลติควาร์กโดยการรบกวนเล็กๆได้ จึงทำให้การบรรยายเชิงปริมาณของสถานะมัลติควาร์ผ่าน
การคำนวณทางทฤษฎีสนามควอนตัมเชิงรงค์โดยวิธีปกติพบกับปัญหามากมาย และไม่สามารถให้ค่าที่เชื่อ
ถือได้ ในวิทยานิพนธ์นี้ เราจะพิจารณาใช้ทฤษฎีสนามควอนตัมเชิงรงค์ตามหลักการของโฮโลกราฟิกเพื่อ
ทำการคำนวณและบรรยายสถานะมัลติควาร์กในเชิงปริมาณ [4, 5] ผ่านแบบจำลองของซาไก-ซูกิโมโต จาก
นั้นเราจะพิจารณาใช้สมการสถานะของมัลติควาร์กในการเชื่อมขอบเขตของสมการสถานะที่รู้กันเป็นอย่างดี
ระหว่างสมการสถานะควาร์ก-กลูออนอิสระที่ความหนาแน่นสูงมากๆ และ สถานะนิวเคลียร์จากทฤษฎีสนาม
ยังผลแบบไครัลที่ความหนาแน่นต่ำ ลักษณะสมการสถานะของมัลติควาร์กที่ได้จากการคำนวณจะมีความแข็ง
เนื่องจากทนการอัดได้มาก แต่จะอ่อนลงที่ความหนาแน่นสูงๆ เราพบว่าเมื่อความดันและความหนาแน่นของ
สถานะมีค่าสูงกว่าค่าที่จุดเปลี่ยนเฟส สสารมัลติควาร์กจะมีความเสถียรในเชิงอุณหพลศาสตร์มากกว่าสสาร
นิวเคลียร์ จากการคำนวณดาวนิวตรอนที่มีมวลมากและมีแกนกลางดาวเป็นมัลติควาร์กจะมีมวลของดาวใน
ช่วง $14.3 - 11.8$ $(14.0 - 11.1)$ กิโลเมตร สำหรับค่า $\epsilon_s = 26$ (28) GeV fm^{-3} ตามลำดับ จากการศึกษาผล
ของสัดส่วนระหว่างโปรตอนต่อแบริออนในสมการสถานะของแบริออนพบว่าเมื่อสัดส่วนโปรตอนมีค่ามากขึ้น
จะทำให้มีการลดลงรัศมีของดาวนิวตรอนไม่เกิน 1 กิโลเมตร นอกจากนี้เรายังคำนวนค่าตัวเลขของเลิฟ และค่า
การผิดรูปไทดัลแบบไร้มิติ พบว่าค่าที่ได้อยู่ในช่วงที่เป็นไปได้เมื่อพิจารณาในเชิงกายภาพภายใต้ข้อจำกัดจาก
การสังเกตการณ์ ท้ายที่สุดเราได้คำนวณหาความถี่ของการสั่นในแนวรัศมีของแกนดาวที่เป็นมัลติควาร์กตั้งแต่
โหมดที่ 0 ถึง 5 ตลอดช่วงมวลที่เป็นไปได้ พบว่าโหมดพื้นฐานมีความถี่ประมาณ 2.5 กิโลเฮิรตซ์ เมื่อกำหนด
ให้ค่าสเกลความหนาแน่นของพลังงาน ตามแบบจำลองเชิงโฮโลกราฟิกของซาไก-ซูกิโมโต $\epsilon_s = 23.2037$ GeV
fm^{-3} โดยความถี่นี้จะมีค่าแปรผันกับ $\sqrt{\epsilon_s}$

ภาควิชา ฟิสิกส์ .... ลายมือชื่อนิสิต ....

สาขาวิชา ฟิสิกส์ .... ลายมือชื่อ อ.ที่ปรึกษา ....
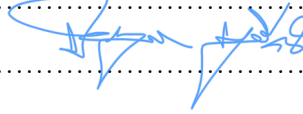
ปีการศึกษา 2564 ....

6273060623 : MAJOR PHYSICS

KEYWORDS : MASSIVE NEUTRON STAR, HOLOGRAPHIC QCD, MULTIQUARK CORE

SITTHICHAI PINKANJANAROD : A STUDY OF MASSIVE NEUTRON STARS WITH HOLOGRAPHIC MULTIQUARK CORES . ADVISOR : ASSOC. PROF. PIYABUT BURIKHAM, Ph.D. 108 pp.

Up to now, the state of matter inside a massive neutron star (NS) is still unclear. In the core of the massive NS, density and pressure become large until the matter inside could turn into deconfined matter e.g. quark-gluon plasma (QGP). Recently, results from a model-independent analysis [1] from a combination of perturbative theoretical calculations with observational data [2, 3] shows that quark matter could exist in the cores of massive NS with masses above 2.0 $M_\odot$. However, the QGP exists at a very high temperature. Compared to the relatively low temperature of the NS, the exotic quark matter might not be the free QGP but instead, the deconfined and chiral symmetry broken bound state called "multiquark". Due to the non-perturbative nature of the multiquark state, the usual description of the multiquark state as based on QCD faces many difficulties and becomes unreliable. In this thesis, we use a holographic QCD approach to describe the multiquark [4, 5] based on the Sakai-Sugimoto (SS) model and implement the equation of states (EoS) of multiquark matter to interpolate between the two known limits: the pQCD EoS at high densities, and the nuclear CET EoS at low densities. The multiquark EoS is relatively stiff at low densities and becomes softer at high densities. Thermodynamically, we found that the multiquark phase is more preferred over the extended CET nuclear matter above the transition points. From our study, the massive NS with a holographic multiquark core could have masses in the range between $1.96 - 2.23$ $(1.64 - 2.10)M_\odot$ and radii between $14.3 - 11.8$ $(14.0 - 11.1)$ km for $\epsilon_s = 26$ (28) GeV fm^{-3} respectively. Effects of proton-baryon fractions are also studied for a certain type of baryonic EoS. We found that larger proton fractions could reduce the radius of the NS with the multiquark core by less than a kilometre. Additionally, we calculate the tidal Love number and dimensionless deformation parameter, k_2 and Λ, and they are found to be within the limit of the physically viable range under the present constraints. Finally, we calculate radial pulsation frequencies of the multiquark core for $n = 0 - 5$ modes for the entire mass range. As a result, for $M_{\text{core}} \simeq 2M_\odot$, the fundamental-mode frequency is around 2.5 kHz given that the energy density scale of the holographic SS model $\epsilon_s = 23.2037$ GeV fm^{-3}, this frequency is proportional to $\sqrt{\epsilon_s}$.

Department : Physics .... Student's Signature ....

Field of Study : Physics .... Advisor's Signature ....

Academic Year : 2021 ....

Acknowledgements

I would like to express my appreciation to my supervisor, Assoc. Prof. Dr. Piyabut Burikham, for giving me guidance on performing research in the field of theoretical high-energy physics and theoretical astrophysics. Without his support, there would be no publications or this thesis in the related fields.

I am very grateful to my thesis committee: Assoc. Prof. Dr. Udomsilp Pinsook, Asst. Prof. Dr. Pawin Ittismai, Dr. Thiparat Chotibut, and Dr. Supakchai Ponglertsakul. All of their cooperation, suggestions, and comments are valuable to me.

I am sincerely honoured for having been selected to receive the PhD scholarship from the Second Century Fund, Chulalongkorn University (C2F). I am deeply thankful for the support.

Finally, my gratitude goes to my parents and my family. This dissertation was written in dedication to their love and support. I am deeply indebted to them for their encouragement and consolation.

Table of Contents

Chapter **page**

List of Tables

List of Figures

Figure   **page**

Figure   **page**

CHAPTER I

Introduction

Generally, the stars collapse under extreme gravitation as thermonuclear fuel depletes at the ultimate fate. However, the quantum degeneracy pressure of fermions goes against the collapses. According to Refs. [6, 7], the degeneracy pressure caused by neutrons could withstand gravitational collapses of any stars with masses below $0.7M_\odot$. According to the Ref. [8], those less massive than 1.4 solar masses would remain dwarf stars forever. For the stars with $M > 1.4M_\odot$, additional repulsive nuclear force is required to support the gravitational collapses. Those with $M >> 1.4M_\odot$ will undergo a late state of thermonuclear fusion and eventually explode violently called supernovae. After the explosions, their remnants could turn into neutron stars or black holes, depending on the remaining masses.

From various observations, the minimum mass of neutron star is around $1.1M_\odot$ while the upper mass limit of a neutron star, sometimes called the Tolman–Oppenheimer–Volkoff limit, is around $2.1M_\odot$, in accordance with [9, 10]. Nevertheless, a recent estimation shows that the upper limit is at $2.16M_\odot$, as reported by [11]. According to the discovery of a pulsar called "PSR J0740+6620" [12], the upper mass limit of neutron stars is around $2.16M_\odot$. It is likely that below the Chandrasekhar limit or $1.39M_\odot$, any compact stars are generically white dwarfs, while those with a mass between $1.4M_\odot$ and $2.16M_\odot$ are presumably neutron stars. However, there is an observational mass range overlap between low-mass neutron stars and high-mass white dwarfs in the order of around a few tenths of a solar mass. Beyond $2.16M_\odot$ gravitational collapse of the mass of the stellar remnant may overcome the strong force repulsion and neutron degeneracy pressure and eventually turn the remnants into a black hole. However, the lightest observed mass of a stellar black hole until now is about $5M_\odot$. Those between $2.16M_\odot$ and $5M_\odot$ may be hypothetical intermediate-mass stars, e.g. quark stars and electroweak stars. Nevertheless, none of them has been confirmed.

Recently, there was a model-independent analysis to study the probability of quark matter in the NS proposed by the Ref. [1]. This work uses a method called "new sound-of-speed interpolation" that the sound speed squared c_s^2, depending on the baryon chemical potential μ, was used to determine other thermodynamic functions especially the pressure $P(\mu)$ and energy

density $\rho(\mu)$ which represent the model-independent equation of state(EoS). Then, the new sound-of-speed method was used repeatedly to generate around 570,000 individual EoSs ranging from soft to hard. Additionally, this work imposes the following two astrophysical constraints on the EoS: (a) the requirement of supporting a 1.97 $M_\odot$ NS [2, 3] and (b) the tidal deformability Λ for a 1.4 $M_\odot$ star lie within observational range [13, 14]. Roughly 160,000 of these fulfil the astrophysical constraints. This research discloses that the interpolation between low density the Chiral Effective Field Theory (CET) [15] and high-density perturbative QCD [16, 17] (pQCD) could be described simply by two effective power-law equations of states (EoS). The empirical EoS yields the adiabatic index and sound speed indicating that the NS has a quark core.

Fundamentally, the behaviour of free quarks and gluons at very high energy could be described by pQCD. Quarks interact with each other via exchanging colour charges. At low temperatures, quarks exist inside hadrons, e.g. neutrons and protons, known as stable bound states of quarks since they are all colourless. In other words, this means that there are no exchanging colour charges between stable bound states. Instead, the effective interactions between neutrons and protons could be described by CET where nucleons interact with each other via exchanging π mesons. Note that the CET resembles the π mesons theory at low energies. However, at low temperature and high density, the bound states of quarks could become deconfined, since one quark might drip from one to another, while they are still bounded by gravity inside the star. The deconfined bound states of quarks at low temperature and high density are later called the multiquark states. The multiquarks interact with each other through the remaining Coulomb-like strong interaction mediated by unconfined gluons and effectively via mesons. For decades, multiquark candidates like tetraquark and pentaquark have been gathered from several observations; see, for example, Ref. [18] for the most recent report. Typically, an abundance of multiquarks could be found at the cores of compact stars, where deconfined quarks are squeezed firmly together.

At low temperatures and moderately high densities, multiquarks interact strongly with each other. Therefore, the behaviour of the multiquark could not be described by the perturbative calculation as being used in pQCD. We need non-pQCD approaches to describe the multiquarks. However, there are many issues when using the non-pQCD approaches e.g. the increasing computational difficulty and the sign problem of lattice QCD approach as the baryon chemical potential increases, or MIT bag as a model for analysing the behaviour of deconfined quarks and gluons in dense stars has a reliability concern. Therefore, using the non-pQCD approaches derived from the fundamental QCD is still problematic.

Alternatively, the AdS/CFT correspondence [19, 20, 21] is a supplementary and powerful tool that could be used for investigating strongly-coupled gauge theory by considering the weakly gravity theory. Based on the gauge/gravity duality, the two theories specified in separate

dimensions are conjectured to be equivalent under a strong-weak duality, which is important to describe highly coupled QCD. Higher-dimensional configurations consisting of open strings and D-branes in a given background could be used to represent mesons and baryons (see e.g. Refs. [22, 23, 24] for earlier works and Ref. [25] for more recent development). According to Ref. [4], the holographic multiquark (MQ) phase in the deconfined background with broken chiral symmetry based on the Sakai-Sugimoto [26, 27, 28, 29] is more thermodynamically preferred over the QGP phase at low to moderate temperatures up to the QGP phase transition around trillion Kelvins. The multiquark phase EoS was calculated and applied to the hypothetical multiquark star and NS with the multiquark core in Ref. [5]. According to preliminary calculations, NS with a multiquark core mass of $3M_\odot$ could exist.

With the possibility of quark matter cores in massive NS above $2M_\odot$ from the empirical analysis, it's worth looking at how the holographic multiquark EoS fits into the observational limits. Aside from the mass M and radius R of the star, the compactness of the star, as described by a ratio of M/R, is also important to determine the exact EoS of the matter inside the NS as well as other probable extreme compact objects like quark stars. Tidal deformability of the star parametrized by Love number k_2 [30, 31, 32, 33] and the dimensionless parameter Λ described in Chapter 6 are also useful probe the NS's interior. Typically, the tidal deformability and other parameters such as the moment of inertia of the star and sound speed in quark and nuclear matter inside the star, are also estimated holographically in Refs. [34, 35, 36, 37].

In this research, we re-examine the holographic model developed in Ref. [5] and show how well it can interpolate between the low and high-density EoS by matching the EoS of multiquark matter with the low and high-density EoS. We further demonstrate that the masses of NSs with multiquark cores are consistent with the existing observations, permitting NS $M \gtrsim 2M_\odot$ [2, 3]. We demonstrate that the mass of any NS with a multiquark core could be as high as $2.2 - 2.3M_\odot$ depending on the colour states of multiquarks, which is still too light to be a candidate for the object recently discovered by LIGO/Virgo [38], that requires mass about $2.50 - 2.67M_\odot$. Then, using Chiral Effective Field Theory (CET) EoS [15] and FYSS [39, 40, 41] for the nuclear crust, we determine the Love number k_2 and Λ of the NS with the multiquark core. In addition, the multiquark star (MQS) deformation parameters will be calculated in comparison.

This dissertation is organized as the following. A review of standard nuclear matter theory at finite densities from ultra-low densities to intermediate densities will be in Chapter 2. The EoS of multiquark nuclear matter is presented in Chapter 3, which discusses the holographic model investigated in Ref. [5]. The EoS from CET and piecewise polytrope utilised in interpolation, as well as the EoS of the multiquark core in the high-density region, are summarised in Chapter 4. This chapter also covers the thermodynamics of a phase transition between baryonic matter and multiquark matter. A revision of Tolman–Oppenheimer–Volkoff equations required

for stellar modelling, mass-radius diagram, mass-central density relation as well as thermody-namic properties of NS with multiquark core are explored in Chapter 5. The tidal deformation of the NS with multiquark core and MQS are calculated in Chapter 6. Then, the adiabatic index and sound speed of the multiquark core are explored, as well as the radial pulsations of the stars are discussed in Chapter 7. Finally, Chapter 8 concludes this dissertation.

CHAPTER II

Nuclear Matter at Finite Densities

In this chapter, we consider a review of nuclear matter in equilibrium at zero temperature and finite densities from very low densities up to the order of a nuclear saturation density ρ_s, following Refs. [42, 43, 44, 45]. At very low densities, matter in its ground state is mainly composed of ^{56}Fe nuclei, arranged into a lattice to minimize their Coulomb interaction energy. As density increases, the electron chemical potential (Fermi energy including its rest mass), μ_e also increases. The nuclear matter in this range could be described by EoS from Ref. [42]. Beyond $\rho \sim 10^4$ g cm^{-3}, electrons become free. Additionally, above $\sim 10^7$ g cm^{-3}, electrons become fully relativistic. For electron chemical potential $\mu_e \gtrsim 1$ MeV or density $\rho \gtrsim 8 \times 10^6$ g cm^{-3}, ^{56}Fe nuclei are no longer in their lowest energy state; however, the energy can be lowered by having nuclei capture energetic electrons then losing energy via neutrino emission, and become more neutron-rich. Beyond this point, the lowest energy state of nuclear matter is a lattice of ^{62}Ni nuclei. With increasing density, the lattice in equilibrium becomes progressively richer in neutrons. The characteristic of nuclear matter in this range could be described by the standard nuclear calculations, according to Ref. [43]. At density $\rho \simeq 4.3 \times 10^{11}$ g cm^{-3}, neutrons start dripping out of the nuclei and the continuum neutrons states become dominated. We used the description of nuclear matter in this range from Ref. [44]. Above $\rho \sim 2 \times 10^{14}$ g cm^{-3}, boundary of each nuclei are no longer exist. Nuclear matter becomes a uniform mixture of primary neutrons, protons, and electrons. With densities increasing further, we consider the behaviour of nuclear matter described by the chiral effective field theory or CET [45].

2.1 Nuclear Matter at Ultra-Low Densities

A revision in this section follows Ref. [43]. From densities between 10^4 and 4.3×10^{11} g cm^{-3}, free neutrons as well as free electrons begin to appear and soon become relativistic. The nuclei are balanced against beta decay by the occupied electron Fermi sea. EoS of nuclear matter in

this density range could be determined from the configuration of the nuclei in beta-equilibrium. The major contributions to the energy in this regime are nuclear energy, free electron energy, and negative lattice energy. Detailed calculations were given by Ref. [46].

While lattice only contributes to a small part ($\sim Z^{2/3}e^2$) of total pressure, it has a significant role to determine the equilibrium of the nucleus at higher densities. The equilibrium is determined by a competition between the nuclear surface energy, which favours nuclei with a large number of nucleons, A, and the Coulomb energy that favours small-A nuclei. The Coulomb energy is the sum of the positive nuclear Coulomb self-energy and the negative lattice Coulomb energy.

Above 4.3×10^{11} g cm^{-3}, the EoS of nuclear matter in the free-neutron regime had been proposed by Ref. [44] in 1971. The main difficulty in this range is to determine the masses of nuclei. Nuclei in this regime are very neutron-rich and immersed in a sea of free neutrons exerting pressure on the surface of nuclei. In this regime, the lattice Coulomb energy becomes extremely important to determine nuclear size since the lattice Coulomb energy is almost in the same order of magnitude and of opposite sign to the nuclear Coulomb self-energy. As the density increases, there will be more and more nuclei filling up the space. Eventually, at the density 2.4×10^{14} g cm^{-3}, the nuclei begin to touch each other. Then there would be a first-order phase transition where density suddenly changes to about 3×10^{14} g cm^{-3}.

The standard techniques for nuclear-matter theory can be applied to determine EoS in the regime with some confidence up to about 5×10^{14} g cm^{-3}. Beyond this density, EoS is very uncertain since there is little information and knowledge of interactions between exotic hadrons e.g. various hyperons. As density is sufficiently high, the conventional techniques in nuclear-matter theory require modification.

2.1.1 EoS for Nuclear Matter at Ultra-Low Densities

Consider nuclei present at any density below the neutron drip. Assume that the nuclear matter is composed of nuclei with nucleon number A and relative charge Z with a number of nuclei per unit volume n_N. The total energy per unit volume for the system of nuclei at densities below the neutron drip is given by

$$\epsilon_{\text{tot}}(A, Z, n_N) = n_N \left(W_n + W_L \right) + \epsilon_e(n_e) \tag{2.1}$$

where $W_n(A, Z)$ is the total energy of an isolated nucleus with contribution of nucleons rest mass but without electron energy. The total electron energy per unit volume is denoted by $\epsilon_e(n_e)$, where the mean electron's number density is

$$n_e = Z n_N. \tag{2.2}$$

The lattice energy per nucleon W_L for a body-centred cubic (bcc) lattice described by Ref. [47] is lowered for a specified density of nuclei with charge Z, written as

$$W_L = -1.819620 Z^2 e^2 / a \qquad (2.3)$$

where a is the lattice constant written as a function of n_N is given by

$$a^3 = 2/n_N. \qquad (2.4)$$

Beyond 10^4 g cm^{-3}, electrons could be considered to be free so that

$$
\begin{aligned}
\epsilon_e &= \frac{1}{\pi^2} \int_0^{k_e} dk k^2 (k^2 + m_e^2)^{1/2} \\
&= \frac{m_e^4}{8\pi^2} \left[(2t^2 + 1) t (t^2 + 1)^{1/2} - \log(t + (t^2 + 1)^{1/2}) \right]
\end{aligned}
\qquad (2.5)
$$

where k_e is the electron Fermi wavenumber and $t = k_e/m_e$. Note that all equations from here on will be written in Planck units. For ultra-relativistic electrons, $t \gg 1$. Therefore,

$$\epsilon_e = \frac{3}{4} n_e m_e t. \qquad (2.6)$$

The values of A and Z for nuclei in equilibrium at any density below neutron drip are those minimizing ϵ_{tot} at fixed baryon's number density n_B. The number density of nuclei and electrons are given in terms of n_B by

$$n_N = n_B/A, \qquad n_e = n_B Z/A. \qquad (2.7)$$

Here we have the rest masses of electrons subtracted out of the nuclear energies, but not the atomic-electron binding energy. The reason for not to exclude the atomic-electron binding energy is that the electron density distribution in the solid is uniform to the first approximation. Consequently, the interaction energy is included in the lattice energy W_L. However, due to electron-screening effects, there are slight deviations of electron distribution from being uniform, that produce an energy per nucleus [48]

$$W_{\text{screening}} = -0.2535 Z^{7/3} \mu_e e^4 \qquad (2.8)$$

where the electron Fermi energy including the rest mass is given by

$$\mu_e = \frac{\partial \epsilon_e}{\partial n_e}. \qquad (2.9)$$

Comparing to the electron Fermi energy excluding the rest masses, of an insulated atom, is given, in the Thomas-Fermi approximation, by

$$W_{\text{atom}} = -0.766 Z^{7/3} m_e e^4. \qquad (2.10)$$

We could make an error with the same order of magnitude by not subtracting the electronic contribution out of the binding energy as the $W_{\text{screening}}$ is neglected in ϵ_{tot}

Nucleus	BE/A (MeV)	Z/A	$\rho_{\max}$ (g cm^{-3})	μ_e (MeV)	$\frac{\Delta\rho}{\rho}$ (%)
^{56}Fe	8.7905	0.4643	8.1×10^{6}	0.95	2.9
^{62}Ni	8.7947	0.4516	2.7×10^{8}	2.6	3.1
^{64}Ni	8.7777	0.4375	1.2×10^{9}	4.2	7.9
^{84}Se	8.6797	0.4048	8.2×10^{9}	7.7	3.5
^{82}Ge	8.5964	0.3902	2.2×10^{10}	10.6	3.8
^{80}Zn	8.4675	0.3750	4.8×10^{10}	13.6	4.1
^{78}Ni	8.2873	0.3590	1.6×10^{11}	20.0	4.6
^{76}Fe	8.9967	0.3421	1.8×10^{11}	20.2	2.2
^{124}Mo	8.8577	0.3387	1.9×10^{11}	20.5	3.1
^{122}Zr	8.6705	0.3279	2.7×10^{11}	22.9	3.3
^{120}Sr	8.4522	0.3166	3.7×10^{11}	25.2	3.5
^{118}Kr	8.7202	0.3051	4.3×10^{11}	26.2	$\cdots$

Table 2.1: Nuclear data for equilibrium nuclei below neutron drip: obtained from Ref. [43]

As the pressure, P increases continuously with increasing depth until the density ρ reaches the neutron drip, there would be a first-order transition where the density undergoes sudden change resulting in abrupt density discontinuity. Note the pressure before the neutron drip is due to the electron kinetic energy to the first approximation. Therefore, the electron number density is required to be continuous across each transition. However, the number density of baryons is given by $n_e A/Z$. Therefore, across the transition from nucleus (A, Z) to nucleus (A', Z'), a change in baryon number density is given by

$$n'_B - n_B \approx n_e \left(\frac{A'}{Z'} - \frac{A}{Z} \right). \tag{2.11}$$

The fractional change in the density, $\rho = \epsilon_{\text{tot}}$ is approximately given by

$$\frac{\Delta\rho}{\rho} \approx \frac{\Delta n_B}{n_B} \approx \frac{Z/A}{Z'/A'} - 1. \tag{2.12}$$

From the Table 2.1, there is a sudden change in density associated with each transition e.g. in the first transition from ^{56}Fe to ^{62}Ni, density increases by 2.9 %. Due to these discontinuities, it is essential to make a plot of P versus $1/n_B$ to determine which transition takes place. It is noted from Ref. [46] that the quantity to be minimized at the fixed P is the baryon chemical potential

$$\mu_B = \frac{\epsilon_{\text{tot}} + P}{n_B}, \tag{2.13}$$

where the pressure could be determined from

$$P = n_B^2 \frac{\partial(\epsilon_{\text{tot}}/n_B)}{\partial n_B} \bigg|_{Z,A}. \tag{2.14}$$

Using Eq. (2.1) and Eq. (2.7), the pressure becomes

$$P = P_e + \frac{1}{3}W_L n_N \tag{2.15}$$

where first term is the electronic pressure, given by

$$P_e = n_e \frac{\partial \epsilon_e}{\partial n_e} - \epsilon_e, \tag{2.16}$$

whereas the second term is the negative pressure of the lattice. Then,

$$\mu_B = (W_N + \frac{4}{3}W_L + Z\mu_e)/A \tag{2.17}$$

Note that μ_B is continuous across a transition. To minimize μ_B, it is required that P, A, and Z solves Eq. (2.16) for the electronic number density $n_N = n_e/Z$. By using Eq. (2.17), n_e and μ_B could be evaluated with the tabulated value of $W_N(A, Z)$ given by

$$W_N = m_n(A - Z) + m_e Z - bA \tag{2.18}$$

where $b \equiv BE/A$ is binding energy BE per nucleon.

Table 2.1 provides information about the binding energies, with maximum density $\rho_{\max}$, and electron chemical potential at which they occur. The fractional mass density $\frac{\Delta\rho}{\rho}$ increases notably across the transition to the next nuclide while the ratio Z/A decreases with the increasing density.

Given that A and Z minimize

$$\frac{\epsilon_{\text{tot}}}{n_B} = \frac{W_N + W_L}{A} + \frac{\epsilon_e(n_B Z/A)}{n_B} \geq 0, \tag{2.19}$$

at fixed n_B, This implies that, for $\Delta A \ll A$ and $\Delta Z \ll Z$

$$\Delta\left(\frac{W_N + W_L}{A}\right) + \left(\frac{\Delta Z}{A} - \frac{Z}{A^2}\Delta A\right)\mu_e. \tag{2.20}$$

The lattice energy W_L is directly proportional to $Z^2/A^{1/3}$, at fixed n_B. Therefore,

$$\Delta W_L = W_L\left(\frac{2\Delta Z}{Z} - \frac{\Delta A}{3A}\right). \tag{2.21}$$

Combining Eq. (2.17) and Eq. (2.21) together, we obtain

$$\Delta W_N \geq \mu_B \Delta A - \left(\mu_e + \frac{2W_L}{Z}\right)\Delta Z. \tag{2.22}$$

With $\Delta Z = 0$, the change in the lattice Coulomb energy due to ΔA is

$$\Delta_A W_N \geq \mu_B \Delta A, \tag{2.23}$$

while for $\Delta A = 0$,

$$\Delta_Z W_N \geq -\left(\mu_e + \frac{2W_L}{Z}\right)\Delta Z. \tag{2.24}$$

The condition is for beta-equilibrium of the nuclei analogous to the usual beta-stability criterion for isolated nuclei:

$$\Delta_Z W_L \geq -m_e \Delta Z. \tag{2.25}$$

The amount of baryons in the system increases by A as the density rises before free neutrons emerge. This could be accomplished by introducing a nucleus (A, Z) and Z electrons into the system, which demands such energy.

$$\left(\frac{\partial \epsilon_{\text{tot}}}{\partial n_N} \right)_{n_e = Z n_N} = \mu_B A, \tag{2.26}$$

or equivalently by adding A neutrons in continuum states, which raises the energy per particle by $(m_n + \epsilon_{n,0})A$ where $\epsilon_{n,0}$ is the lowest energy for a neutron in continuum state in the lattice. The condition before neutron starts dripping can be expressed as

$$\mu_B < m_n + \epsilon_{n,0}. \tag{2.27}$$

Neutron drip starts when the chemical potential μ_B reaches $m_n + \epsilon_{n,0}$. After that, the free neutrons start becoming populated. Because of the interaction of a free neutron with the nuclei, the lowest energy per neutron in the lattice $\epsilon_{n,0}$ deviates somewhat from zero. It can be estimated by considering the average potential of a slow neutron passing through a nucleus like ^{118}Kr to be attractive within the order of a few tens of MeV. Because neutron drip occupy only about $\rho/(3 \times 10^{14} \text{ g cm}^{-3}) \sim 10^{-3}$ of space, the average neutron potential is $\sim -10^{-2}$ MeV $\approx \epsilon_{n,0}$. It was found in Ref. [43] that neutron drip starts at $\rho \simeq 4.3 \times 10^{11} \text{ g cm}^{-3}$, at the point where the electron chemical potential is 26.2 MeV. The corresponding equilibrium nucleus is ^{118}Kr, which is still the most favourable nucleus even at slightly higher densities.

The EoS below 10^4 g cm^{-3} could be considered from the Ref. [42] while the EoS between 10^4 g cm^{-3} and 4.3×10^{11} g cm^{-3} is calculated here. The description for EoS between 4.3×10^{11} g cm^{-3} and 5×10^{14} g cm^{-3} can be obtained from the Refs. [44, 49] and would be considered in the next section.

2.2   Nuclear Matter at Low Densities

In this section, we consider the conventional nuclear theory that is still valid for densities ranging between 4.3×10^{11} g cm^{-3}, where neutrons start leaking out, to roughly 5×10^{14} g cm^{-3}. This section's content is taken entirely from Ref. [43]. The energy of nuclei in the free neutron regime has three distinct characteristics: (i) similarity between bulky nuclear matter inside nuclei and free neutron gas outside nuclei; (ii) the emergence of free neutron gas, which diminishes the nuclear surface energy; and (iii) the growing importance of the Coulomb interaction between nuclei as the spacing among nuclei approaches the nuclear radius.

2.2.1 Equilibrium Conditions for Nuclear Matter at Low Densities

The nuclear matter in the free neutron regime comprises a lattice of nuclei drowned in neutrons and electron gas, with densities ranging from 4.3×10^{11} g cm^{-3} to roughly 2.5×10^{14} g cm^{-3}. Free protons, on the other hand, are absent here, until just before they break down. Lattice nuclei, free neutrons, and free electrons are all present in the system. The conditions for a system of nuclear matter in equilibrium at zero temperature are discussed in this section.

Given that a volume V contains number of neutrons outside the nuclei N_n and the number of nuclei N_N. The total volume outside the nuclei is $V - N_N V_N$. Therefore, neutron number density is given by

$$n_n = \frac{N_n}{V - N_N V_N}. \tag{2.28}$$

The electrons completely pass through the lattice of nuclei and have a uniform density n_e because the electron screening length is quite long. The charge neutralization of electrons and protons requires that

$$n_e = \frac{Z N_N}{V} \equiv Z n_N, \tag{2.29}$$

where n_N is nuclei density. The total energy density of the system, including all rest masses, is given by

$$\epsilon_{\text{tot}}(A, Z, n_N, V_N, n_n) = n_N(W_N + W_L) + (1 - V_N n_N)\epsilon_N(n_n) + \epsilon_e(n_e) \tag{2.30}$$

where $W_N(A, Z, V_N, n_n)$ is the nuclear matter-energy, $W_L(Z, n_N) = -1.819620 Z^2 e^2/(2/n_N)^{1/3}$ is the lattice energy, ϵ_N is the energy density of nuclei, and ϵ_e is that of electrons gas.

Similar to the previous section, we could determine the equilibrium conditions by minimizing ϵ_{tot} concerning its arguments A, Z, n_N, V_N, and n_n at a given average baryon density n_B as follows

$$n_B = A n_N + (1 - V_N N_N) n_n. \tag{2.31}$$

Given that nuclei contain a fixed amount of $n_N Z$ protons and $n_N(A - Z)$ neutrons in a unit volume, as well as a fixed amount of overall fraction $n_N V_N$ of the volume filled by nuclei. The nucleons number A could be optimized by minimizing ϵ_{tot} with respect to A itself at fixed $n_N A$, $n_N Z$, $n_N V_N$, and n_n. The energy per nucleon in nuclei is minimized when

$$\frac{\partial}{\partial A}\left(\frac{W_N + W_L}{A}\right)\bigg|_{x, n_N A, n_N V_N, n_n} = 0, \tag{2.32}$$

where it is convenient to consider a proton fraction in nuclei

$$x = \frac{Z}{A} \tag{2.33}$$

instead of the proton number Z.

Secondly, the nuclei must be in beta equilibrium. Since beta decay turns a neutron into a proton (and electron) and raises the total energy, electron capture converts the proton (and electron) back to the neutron then lowers the total energy of the system. In other word, ϵ_{tot} is minimized with respect to variation in Z at fixed A, n_N, V_N and n_n. Minimizing ϵ_{tot} with charge neutrality condition in Eq. (2.29) gives the condition that

$$\mu_e = -\frac{\partial}{\partial Z}(W_N + W_L)\bigg|_{A,n_N,V_N,n_n} = -\frac{\partial}{\partial x}\left(\frac{W_N + W_L}{A}\right)\bigg|_{A,n_N,V_N,n_n}, \tag{2.34}$$

where the electron chemical potential (including the rest mass) is

$$\mu_e = \frac{\partial \epsilon_e}{\partial n_e}. \tag{2.35}$$

Adding a neutron into a nucleus requires minimum energy or the chemical potential for the neutrons in the nuclei given by

$$\mu_n^{(N)} = \frac{\partial}{\partial A}(W_N + W_L)\bigg|_{Z,n_N,V_N,n_n} - m_n. \tag{2.36}$$

Correspondingly, the chemical potential for appending a proton into the nuclei (measured with respect to the neutron rest mass m_p) is

$$\mu_p^{(N)} = \frac{\partial}{\partial Z}(W_N + W_L)\bigg|_{A-Z,n_N,V_N,n_n} - m_p. \tag{2.37}$$

The beta equilibrium condition for chemical potentials of the proton and neutron is provided by

$$\mu_e - (m_n - m_p) = \mu_n^{(N)} - \mu_p^{(N)}. \tag{2.38}$$

There would be no neutron gas outside the nuclei unless $\mu_n^{(N)}$ were negative. Neutrons start trickling out of nuclei as $\mu_n^{(N)}$ grows with baryon number density. The neutron chemical potential in gas $\mu_n^{(G)}$ must be the same as that in nuclei $\mu_n^{(N)}$ for the neutron gas to be in equilibrium. Minimizing ϵ_{tot} with regard to A while fixing Z, nN, V_N, and n_B yields the equilibrium condition. Since n_B is fixed,

$$\frac{\partial n_n}{\partial A} = -\frac{n_N}{1 - V_N n_N} \tag{2.39}$$

then

$$\frac{\partial \epsilon_{\text{tot}}}{\partial A}\bigg|_{Z,n_N,V_N,n_B} = 0$$

$$n_N\left[\frac{\partial}{\partial A}(W_n + W_L)|_{Z,n_N,V_N,n_B} - \frac{\partial \epsilon_n}{\partial n_n}\right] = 0$$

$$\frac{\partial}{\partial A}(W_n + W_L)|_{Z,n_N,V_N,n_B} = \frac{\partial \epsilon_n}{\partial n_n}. \tag{2.40}$$

Combining Eq. (2.36) and Eq. (2.40) with the assumption that W_L is is unaffected by n_n, we obtain

$$\mu_n^{(G)} \equiv \left(\frac{\partial \epsilon_n}{\partial n_n} - m_n\right) + \frac{n_N}{1 - V_N n_N}\frac{\partial W_N}{\partial n_n}\bigg|_{A,Z,V_N,n_N} = \mu_n^{(N)}. \tag{2.41}$$

The neutron chemical potential in gas is defined by Eq. (2.41). The first term is the chemical potential of neutrons in bulk, and the second term is the change in nuclear surface energy once a neutron is delivered to the gas. The energy density of nuclei occupied by the neutron gas outside the nuclei is described as $n_N W_N / (1 - V_N n_N)$.

Finally, by minimising ϵ_{tot} concerning V_N at fixed A, Z, n_N and $n_n(1 - V_N n_N)$, the equilibrium condition between the pressure of the free neutron gas and that of the nuclei may be obtained. As a result, we realize

$$P^{(G)} = P^{(N)} \tag{2.42}$$

where the pressure acting on a nucleus is

$$P^{(N)} = -\frac{\partial}{\partial V_N}(W_N + W_L)|_{A,Z,n_n,n_N} \tag{2.43}$$

and the pressure acting on neutron gas outside the nucleus is

$$P^{(G)} = n_n \mu_n^{(G)} - (\epsilon_n - n_n m_n). \tag{2.44}$$

We can verify the relation between the total pressure given by

$$P = n_B^2 \frac{\partial}{\partial n_B}\left(\frac{\epsilon_{\text{tot}}}{n_B}\right) \tag{2.45}$$

and that given by

$$P = P^{(G)} + P_c. \tag{2.46}$$

The pressure contributed by charged particles is

$$P_c = P_e + P_L, \tag{2.47}$$

where the electron pressure is given by

$$P_e = n_e^2 \frac{\partial}{\partial n_e}\left(\frac{\epsilon_e}{n_e}\right), \tag{2.48}$$

and the (negative) lattice pressure is

$$P_L = n_N^2 \left(\frac{\partial W_L}{\partial n_N}\right)\bigg|_{A,Z,V_N,n_n}. \tag{2.49}$$

In sum, the equilibrium condition are given by Eqs. (2.32), (2.34), (2.41), and (2.42). To apply these criteria, we must clearly define W_N, W_L, ϵ_n and ϵ_e in the following sections.

2.2.2 Nuclear Matter Energy at Low Densities

Consider a system made up of compressed nuclear matter droplets. A nucleus' total energy W_N could be expressed as the sum of volume energy, surface energy, and Coulomb energy. The energy W_N could then be calculated using the semi-empirical mass formula:

$$W_N(A, Z, V_N, n_n) = [(1-x)m_n + xm_p + b(k,x)]A + W_{\text{Coul}}(A, Z, V_N, n_n) + W_{\text{Surf}}(A, Z, V_N, n_n) \tag{2.50}$$

where $b(k,x)$ represents the binding energy per nucleon of bulk nuclear matter at a limited number density.

$$n = \frac{k^3}{1.5\pi^2} \tag{2.51}$$

and k is the wavenumber and $x \equiv Z/A$ is the proton fraction of the nucleus.

Similarly, we apply the same function $b(k,x)$ with $x = 0$ to characterize the neutron outside the nucleus. neutron gas.

$$\frac{\epsilon_n(n_n)}{n_n} = b(k_n, 0) + m_n, \tag{2.52}$$

with

$$n_n = \frac{k_n^3}{1.5\pi^2} \tag{2.53}$$

where the free neutron Fermi wave number equals $2^{1/3}k_n$ and $\epsilon_n(n_n)$ is an energy density for neutrons at the number density n_n. Additionally, the uniformly mixing neutron-proton fluid at higher densities beyond the point that nuclei start dissolving could be characterised by $b(k,x)$.

In the low densities regime, the standard techniques associated with the nuclear-mater theory are still valid to describe the behaviours of nuclei. We consider the effective interaction between nucleons described by the Reid soft-core potential [50], which is one of the best-fitting two-body potentials to the scattering data below 300 MeV. It should be noted that the other fittings are also good, but differences between them are not significant [51].

Before evaluating the binding energy at finite density $b(k,x)$, the correlation function of two interacting nucleons must be determined. For systematic nuclear matter ($x = 1/2$) around the given range of densities, the binding energy from the pair approximation [50] is 11 MeV per nucleon, while the empirical value is about ~ 16 MeV. The 5 MeV difference could be obtained from various corrections e.g. correlations among the three interacting nucleons [52], that among four interacting nucleons [53], and three-nucleon forces arising from exchanging mesons between nuclei [54].

The binding energy of symmetric nuclear matter can be expressed in the following form:

$$b(k, 1/2) = -w_0 + \frac{1}{2}K\left(1 - \frac{k}{k_0}\right)^2 \tag{2.54}$$

where $b_0 \approx 16$ MeV, while $n_0 = k_0^3/1.5\pi^2$ is the saturation number density ≈ 0.16 nucleons per fm^3, or $k_0 \approx 1.4$ fm^{-1}. The pair approximation yields a compressibility parameter K of $sim135$ MeV.

For a near-symmetric ($x \approx 1/2$) nuclear matter, the binding energy per nucleon could be approximated as

$$b(k, x) \approx b(k, 1/2) + S(k)(1 - 2x)^2, \tag{2.55}$$

where the symmetric-energy coefficient could be approximately written as the following form [55]

$$S(k) \approx 31 \left(\frac{k}{k_0} \right)^2 \quad \text{MeV.} \tag{2.56}$$

The reason that the symmetric energy scales as k^2 because the variation of kinetic energy near $x = 1/2$ behaves as $(k^2/6m_n)(1 - 2x)^2 \approx 14(k/k_0)^2(1 - 2x)^2$ MeV.

The most detailed calculation could be obtained from Ref. [56], where the binding energy per nucleon was approximated by a monotonically rising function.

$$b(k, 0) \approx 19.74k^2 - k^3 \left(\frac{40.4 - 1.088k^3}{1 + 2.545k} \right) \quad \text{MeV,} \tag{2.57}$$

where k is in a unit of fm^{-1} for $k \lesssim 1.5$ fm^{-1}. The first term refers to the free neutron gas's kinetic energy, which becomes dominating at low densities.

It was found [56] that ,for $k \lesssim 1.5$ fm^{-1}, the proton chemical potential $\mu_p^{(0)}$ is well approximated by

$$\mu_p^{(0)} = -k^3 \frac{218 + 277k}{1 + 8.57k^2} \quad \text{MeV} \tag{2.58}$$

and k is also in fm^{-1} at the number density of neutron gas $n = k^3/1.5\pi^2$.

For small x, $b(k, x)$ approximately takes the following form

$$b(k, x) = b(k, 0) + x(\mu_p^{(0)} - \mu_n^{(0)}), \tag{2.59}$$

where the chemical potential of pure neutron matter $\mu_n^{(0)}$ is given by

$$\mu_n^{(0)} = \frac{\partial \epsilon_n(n_n)}{\partial n} = b(k, 0) + \frac{1}{3}k \frac{\partial b(k, 0)}{\partial k}. \tag{2.60}$$

Another correction term in the powers of x from the proton kinetic energy is

$$\frac{3[(2x)^{1/3}k]^2}{10m_p^\star}x = 19.74k^2 x^{5/3} \frac{m_n}{m_p^\star} \quad \text{MeV.} \tag{2.61}$$

Note that $m_p^\star$ is the effective mass of a proton for pure neutron state of matter where the empirical value of $m_p^\star/m_n \approx 0.65$.

Without complete functions of $b(k, x)$ for the value of x between the pure neutron gas ($x = 0$) and nearly symmetric nuclear matter ($x = 1/2$), we need to interpolate $b(k, x)$ smoothly within our knowledge. To construct the interpolation, we need the following information:

1. For ($x = 1/2$) around the saturation density, $b(k, x)$ has the form of Eq. (2.54):

$$b(k, 1/2) = -w_0 + \frac{1}{2}K \left(1 - \frac{k}{k_0} \right)^2. \tag{2.62}$$

2. For small x, from Eq. (2.57) to Eq. (2.61), the binding energy per nucleon has a form:

$$b(k, x) = b(k, 0) + x(\mu_p^{(0)} - \mu_n^{(0)}) + \frac{3(2^{1/3}k)^2}{10m_n}x^{5/3}. \tag{2.63}$$

3. For low k, there is only a contribution from kinetic energy of the free particle, so the binding energy per nucleon is

$$b_{\text{kin}}(k,x) = \frac{3(2^{1/3}k)^2}{10m_n}\left(x^{5/3} + (1-x)^{5/3}\right). \tag{2.64}$$

4. For small deviation $\alpha \equiv 1 - 2x$ from $x = 1/2$, there is a correction for $b(k,x)$ interpreted as the symmetric energy per nucleon given by

$$b_{\text{sym}} = b(k,x) - b(k,1/2) \approx \frac{sk^2}{k_0^2}\alpha^2. \tag{2.65}$$

First, we need to interpolate $b(k,x)$ between $b(k \approx k_0, 1/2)$ in Eq. (2.62) and $b(k \to 0, 1/2)$ in Eq. (2.64), written as

$$b(k,1/2) = \frac{3k^2}{10m_n}\left(1-\frac{k}{k_0}\right)^3 - w_0\left(\frac{k}{k_0}\right)^3\left[1+\left(1-\frac{k}{k_0}\right)\left(9-6\frac{k}{k_0}\right)\right] + \frac{1}{2}K\left(1-\frac{k}{k_0}\right)^2\left(\frac{k}{k_0}\right)^3. \tag{2.66}$$

Next, the interpolation between $x = 0$ and $x = 1/2$ can be obtained by subtract the kinetic energy term from Eqs. (2.63), (2.66), and the symmetric energy term from Eq. (2.65) then, as a polynomial in even powers of α up to order α^6, create a fitting to the interaction energy. The appropriate interpolation for $b(k,x)$ could be written as

$$\begin{aligned}
b(k,x) &= \left[b(k,1/2) - \frac{3k^2}{10m_n}\right](1-3\alpha^4+2\alpha^6) + \left[s\left(\frac{k}{k_0}\right)^2 - \frac{k^2}{6m_n}\right]\alpha^2(1-\alpha^2)^2 \\
&+ \left[b(k,0) - \frac{3\cdot 2^{2/3}}{10}\frac{k^2}{m_n}\right](3\alpha^4-2\alpha^6) + \left(\mu_p^{(0)} - \mu_n^{(0)} + 2^{2/3}\frac{k^2}{2m_n}\right)\frac{1}{4}(\alpha^4-\alpha^6) \\
&+ b_{\text{kin}}(k,x).
\end{aligned} \tag{2.67}$$

In the limit of $x \to 1/2$, Eq. (2.67) agree with Eq. (2.65) and Eq. (2.66), while that of $x \to 0$ agree with Eq. (2.63). As $k \to 0$, Eq. (2.67) becomes

$$b_{\text{kin}}(k \to 0, x) + \left[2\left(\frac{k}{k_0}\right)^2 - \frac{k^2}{6m_n}\right]\alpha^2(1-\alpha^2)^2. \tag{2.68}$$

The second term fails to disappear in this limit since the term k^2 is not correct as $k \to 0$. Fortunately, in worst case, this only causes $\sim 15\%$ error in $b(k,x)$ in this limit.

The complete interpolation of $b(k,x)$ in Figure 2.1 is plotted by using the parameters b_0, k_0, K, s of nearly symmetric nuclear matter given by

$$w_0 = 16.5 \text{ MeV}, \quad k_0 = 1.43 \text{ fm}^{-1}, \quad K = 143 \text{ MeV}, \quad s = 33.0 \text{ MeV}. \tag{2.69}$$

2.2.3 Nuclear Surface Energy

In this section, we attempt to formulate the nuclear surface energy within the framework of Thomas-Fermi theory, according to Ref. [57] concerning the fluctuation of the bulky energy over
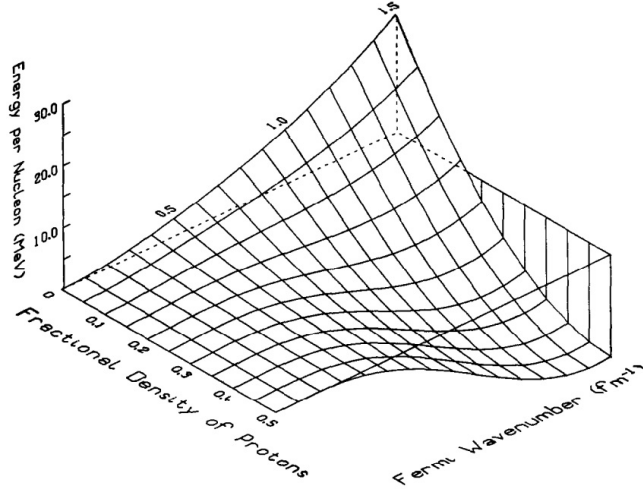
Figure 2.1: The complete interpolation of binding energy per nucleon $b(k, x)$ at finite density n as a function of the mean Fermi wave number k and proton fraction x: image from Ref. [44]

the surface. We postulate that the width of the surface is narrow enough in comparison to the average radius and consider the first layer of the surface at normal to the z-axis dividing the 2 regions. Additionally, we presume that the nucleons' density at radius r: $n(r) \to n_i$ as $z \to -\infty$ and $n(r) \to n_o$ as $z \to +\infty$, given that n_i and n_o is the number density inside and outside the nuclei. The energy of the system can be approximately expressed by

$$\int d^3r b(n(r))n(r) \tag{2.70}$$

where the argument of $b(k, x)$ could be reduced and represented by $b(n)$ for simplicity. Consider a narrow surface at $z = a$ with steps of reduction in number density from n_i to n_o. Given that the system has the identical nucleons' number as the original, we could determine the value of a from

$$\int_{z=-\infty}^{a} d^3r[n(r) - n_i] + \int_{a}^{z=+\infty} d^3r[n(r) - n_o] = 0. \tag{2.71}$$

Consequently, the surface part of Eq. (2.70) or E_σ could be obtained by subtracting from Eq. (2.70) the energy

$$\int_{z<a} d^3r b_i n_i + \int_{z>a} d^3r b_o n_o, \tag{2.72}$$

where $b_i \equiv b(n_i)$ and $b_o \equiv b(n_o)$. The energy per unit area associated with the narrow surface of the nucleus is given by

$$E_\sigma = \int_{-\infty}^{a} dz[b(n(z))n(z) - b_i n_i] + \int_{a}^{+\infty} dz[b(n(z))n(z) - b_o n_o]. \tag{2.73}$$

One could determine $n(z)$ and $x(z)$ directly, using $b(n(z))$ as given from the previous section. Assume that $b(n(z))n(z)$ evolves linearly with $n(z)$ over the surface then

$$b(n(z))n(z) = b_o n_o + \frac{n(z) - n_o}{n_i - n_o}(b_i n_i - b_o n_o), \tag{2.74}$$

then Eq. (2.73) disappears identically.

Additionally, we assume $n(z)$ and $b(n(z))$ could be written in the form of the Fermi-function surface profile $f(z/l_b)$ and $g(z/l_b)$

$$n(z) = n_o + (n_o - n_i)f(z/l_b), \qquad (2.75)$$

$$b(z) = b_o + (b_o - b_i)g(z/l_b). \qquad (2.76)$$

where $f(z/l_b)$ and $g(z/l_b)$ are dimensionless function complying that

$$f(-\infty) = g(-\infty) = 1, \qquad f(+\infty) = g(+\infty) = 0. \qquad (2.77)$$

The length l_b is proportional to the surface thickness t_s. From, Eq. (2.73), we find that

$$E_\sigma = l_b(b_o - b_i)\left[(n_i - n_o)\int d\zeta f(\zeta)(1 - g(\zeta)) + n_o \int d\zeta(f(\zeta) - g(\zeta))\right]. \qquad (2.78)$$

Given that $f = g$, E_σ could be written as a linear function of the number density, then

$$E_\sigma = c_\sigma l_b(b_o - b_i)(n_i - n_o), \qquad (2.79)$$

$$c_\sigma = \int d\zeta f(\zeta)(1 - g(\zeta)). \qquad (2.80)$$

For example, given that a Fermi-function surface profile takes the following form

$$f(z/l_b) = \frac{1}{e^{z/l_b} + 1} \qquad (2.81)$$

then $c_\sigma = 1$ and $l_b \sim 1/4$ to $1/6$ of the surface thickness; but for $f(z/l_b)$ falls from 1 to 0, and linearly between 0 and l_b then $l_b = t_s$ and $c_\sigma = 1/6$.

The correction to the density approximation in Eq. (2.73) also contributes to surface energy. According to the differential Thomas-Fermi theory [57], the symmetric nuclear matter-energy for ordinary nuclei is

$$\int b(n)n d^3r + \frac{B}{n_{NM}}\int (\nabla n)^2 d^3r, \qquad (2.82)$$

where $B \approx 24$ MeV fm^2, and n_{NM} is the saturation number density. The second term in Eq. (2.82) might be generalised to the asymmetric nuclear matter as

$$\frac{1}{n_{NM}}\int d^3r(B_{nn}(\nabla n_n)^2 + B_{pp}(\nabla n_p)^2 + 2B_{np}(\nabla n_n)\cdot(\nabla n_p)), \qquad (2.83)$$

where n_n and n_p denote the neutron and proton number densities respectively. Since the components of nuclear force are long-range and unaffected by many-body correlations, B_{nn} and B_{np} almost the same. However, the coefficient $B_{np} \sim 2B_{nn}$. Therefore, Eq. (2.83) becomes

$$\frac{1}{n_{NM}}\int [B(\nabla n)^2 - B'(\nabla n_n - \nabla n_p)^2] \qquad (2.84)$$

given that $B' \sim 1/3B$. Although, it is unlikely that the term B' in Eq. (2.84) favours spatial fluctuations of the difference in number density $n_n - n_p$, the fluctuations could become significant. Assume that the gradient of n_n and n_p are uniform everywhere i.e.

$$nx = \frac{n_i x_i}{n_i - n_o}(n - n_o), \tag{2.85}$$

then Eq. (2.83) becomes

$$\frac{B_1}{n_{NM}} \int (\nabla n)^2 d^3r, \tag{2.86}$$

where $B \sim B_1$. Given that the system is described by the plane surface density Eq. (2.75), the energy in Eq. (2.86) becomes

$$v \frac{B_1}{n_{MN}} \frac{(n_i - n_o)^2}{l_b}, \tag{2.87}$$

where

$$v = \int_{-\infty}^{\infty} d\zeta \left(\frac{\partial f}{\partial \zeta} \right)^2 . \tag{2.88}$$

For the Fermi-function surface in Eq. (2.81), $v = 1/6$. According to the Thomas-Fermi theory, the length l_b is picked for minimising the total surface energy in Eq. (2.79) and Eq. (2.87), then

$$l_b = \left(\frac{B_1 v}{c_\sigma n_{NM}} \frac{n_i - n_o}{b_o - b_i} \right)^{1/2} \tag{2.89}$$

while the energy per unit area for over all surface is given by

$$E_{\text{surf,TF}} = 2 \left(\frac{v c_\sigma B_1}{n_{NM}} \right)^{1/2} (b_o - b_i)^{1/2} (n_o - n_i)^{3/2} \tag{2.90}$$

where the subscript TF stands for Thomas-Fermi theory. The relation between the number of nucleons A and the surface energy could be determined from a product between $E_{\text{surf, TF}}$ and $4\pi r_N^2$ given that r_N represents the mean radius of the nuclei. Since

$$A = n_i V_N = \frac{k^3}{1.5\pi^2} \frac{4\pi r_N^2}{3} \tag{2.91}$$

then

$$r_N = \left(\frac{9\pi}{8} \right)^{1/3} \frac{A^{1/3}}{k}. \tag{2.92}$$

The total surface energy could be written as

$$b_{\text{surf, TF}} = \frac{\sigma (b_o - b_i)^{1/2}}{w_0^{1/2}} \frac{(n_i - n_o)^{3/2}}{n_{NM}^{3/2}} \left(\frac{k_0}{k} \right)^2 A^{2/3} \tag{2.93}$$

where

$$\sigma = 4 \left(\frac{3}{\pi} \right)^{1/3} k_0 (v c_\sigma B_1 w_0)^{1/2} \tag{2.94}$$

is a coefficient in the order of 20 MeV.

To evaluate the thickness of the surface, first, assume there is no free neutron outside so that the nucleus is made up of free particles in a square well-potential. Inside the well, the

surface thickness scales with the Fermi wavelength. As it is overflowing, the neutrons start dripping out. The inverse of the nucleus's momentum k_c at the top of the well could be used to evaluate the thickness of the surface.

$$\frac{k_c^3}{1.5\pi^2} = n_i - n_o. \tag{2.95}$$

Note that k_c turns into the Fermi momentum in the well when $n_o = 0$. In general, the thickness of the nuclear surface l_b must have a value smaller than $\sim \pi k_c^{-1}$. The surface thickness is inversely proportional to k_c up to the first approximation written as

$$l_b = \frac{\eta\pi}{k_c} \tag{2.96}$$

where $\eta \approx 1$.

Substituting Eq. (2.96) into Eq. (2.79), we obtain the approximation to the surface energy per unit area given by

$$E_{\text{surf}} = \left(\frac{2}{3}\pi\right)^{1/3} \eta c_\sigma (b_o - b_i)(n_i - n_o)^{2/3}. \tag{2.97}$$

Multiplying Eq. (2.97) by the area of nucleus, the total surface energy becomes

$$b_{\text{surf}} = \frac{\sigma(b_o - b_i)}{w_0}\left(1 - \frac{n_o}{n_i}\right)^{2/3} A^{2/3} \equiv w_{\text{surf}} A^{2/3}, \tag{2.98}$$

where

$$\sigma = 2(3\pi^2)^{1/3} c_\sigma \eta w_0. \tag{2.99}$$

Note that the adjustable parameter σ could be evaluated by fitting the nuclear masses and radii of the model to that of the experiment. Interestingly, for ordinary nuclei, where $n_o = 0$, Eq. (2.98) reduces to

$$b_{\text{surf}} = -b_i \frac{\sigma}{w_0} A^{2/3}. \tag{2.100}$$

2.2.4 Coulomb Energy

The nuclear Coulomb energy could be expressed in terms of a uniformly charged sphere of a radius r_N and a total charge Ze by

$$w_{c,0} Z^2 A^{-1/3} = \frac{3}{5}\frac{Z^2 e^2}{r_N}. \tag{2.101}$$

Assume we include the effect of the surface thickness l_b, the nuclear Coulomb energy is lessened by $\sim l_b^2/r_N^2$. Specifically, consider the case that the Fermi-function charge distribution takes the following form:

$$n_p(r) = \frac{Z}{4/3\pi r_N^3}\frac{1}{e^{(r-r_N')/d} + 1} \tag{2.102}$$

where the surface thickness $l_b \approx 2d \ln 9$ and nuclear radius after including effect of the surface thickness $r'_N = r_N(1 - \pi^2 d^2/3r_N^2 + \mathcal{O}(d^4/r_N^4))$. The thickness correction for the Coulomb energy was found to be

$$b_{\text{thick}}(k, x) = -\frac{\pi^2}{2} \frac{d^2 Z^2 e^2}{r_N^3 A} = -\frac{4}{9} \frac{\pi Z e^2 d^2 k^3 x}{A}. \tag{2.103}$$

Another correction to Eq. (2.101) is the photon exchange energy [58],

$$b_{\text{exch}} \approx -\frac{3}{4\pi} \frac{Z e^2 (2x)^{1/3} k}{A}. \tag{2.104}$$

The photon exchange energy per nucleon $b_{\text{exch}}(k, x)$ has a minor contribution to the total correction in the bulk energy W, then it could be neglected. However, it is still important since it depends on the geometry of the surface. Therefore, it must be included in the calculations.

The other electrostatic energy associated with the interaction between a positively charged lattice and a uniformly distributed electron background. The simplest method to calculate the lattice Coulomb energy is a procedure that splits the lattice into unit cells, each having one nucleus at the centre, and each cell is electrically neutral, called the Wigner-Seitz method. The minor correction term of the lattice Coulomb energy from the interaction among the cells could be neglected in a first approximation. For simplicity one can replace the cell with a sphere of an identical size. Accordingly, the condition for the identical spheres is

$$\frac{4}{3} \pi r_c^3 n_N = 1. \tag{2.105}$$

Assume that Z electrons are uniformly distributed over the sphere, the overall electrostatic energy of the cell, or equivalently of the nuclei is given by the sum of Eqs. (2.101), (2.103), (2.104), and the lattice energy below

$$W_L = -\frac{9}{10} \frac{Z^2 e^2}{r_c} \left(1 - \frac{5}{9} \frac{< r^2 >}{r_c^2}\right), \tag{2.106}$$

where $< r^2 >$ is the average squared radius of the charge distribution inside the nucleus. When treating nuclei as point particles, $W_L = -\frac{9}{10} Z^2 e^2/r_c$ provides an excellent estimation to the body centered cubic (bcc) and face centered cubic (fcc) lattices. The exact value of W_L for bcc, fcc, and sc (simple cubic point) lattices are given by

$$W_L = -\frac{Z^2 e^2}{r_c} \times \begin{cases} 0.89593 & \text{(bcc)} \\ 0.89588 & \text{(fcc)} \\ 0.88006 & \text{(sc).} \end{cases} \tag{2.107}$$

For a uniformly distributed proton in the nucleus, the mean squared radius is

$$< r^2 >= \frac{3}{5} r_N^2. \tag{2.108}$$

The total Coulomb energy per nucleus, excluding exchange term b_{exch} and the surface thickness term b_{thick} reduces to

$$w_c \frac{Z^2}{A^{1/3}} = \frac{3}{5} \frac{Z^2 e^2}{r_N} \left(1 - \frac{3}{2} \frac{r_N}{r_c} + \frac{1}{2} \frac{r_N^3}{r_c^3}\right) = \frac{3}{5} \frac{Z^2 e^2}{r_N} \left(1 - \frac{r_N}{r_c}\right)^2 \left(1 + \frac{r_N}{2r_c}\right). \tag{2.109}$$

The first correction term to the lattice energy is the electron screening energy which has been calculated exactly by [59], for a bcc lattice;

$$W_{\text{screening}} = 0.12k_{\text{FT}}^2 r_c^2 W_L < 0, \qquad (2.110)$$

where W_L is the lattice energy per point lattice and k_{FT}^{-1} is the electron screening length, related by

$$k_{\text{FT}} = \left(\frac{4e^2}{\pi}\right)^{1/2} k_e. \qquad (2.111)$$

Notice that k_e is the electron Fermi wave number. Hence

$$W_{\text{screening}} = 0.004 Z^{2/3} W_L. \qquad (2.112)$$

Apparently, this correction is small and may be neglected.

2.2.5 Evaluation of Equilibrium Conditions at Low Densities

According to various types of energy mentioned in many previous sections within this chapter, the total energy associated with a single nucleus, determined by A, Z, and mean wave number k, is given by

$$W_N(A, Z, k, k_n) = [(1-x)m_n + xm_p]A + [b + b_{\text{thick}} + b_{\text{exch}}]A + b_{\text{surf}}A^{2/3} + w_{c,0}Z^2 A^{-1/3} \qquad (2.113)$$

where $k_n = (1.5\pi^3 n_n)^{1/3}$. Note that for fixed x, a whole W_N explicitly depends on A. The volume energy per nucleon b is given by Eq. (2.67), the surface energy by Eq. (2.98), the Coulomb energy contributions by Eq. (2.101) and Eq. (2.103), and lastly the exchange energy by Eq. (2.104). We can include W_L, the lattice energy simply by replacing $w_{c,0}$ by w_c. The value for d in b_{thick} is chosen to be $0.74/k_c$, so it would be in agreement with the value of surface thickness determined from electron scattering experiment. The Eq. (2.113) is considered to be semi-empirical mass formula for nuclear energies consisting of 5 parameters: w_0, k_0, K, and s in the volume energy, and σ in the surface energy.

The parameters could be evaluated by fitting the Eq. (2.113) to ordinary nuclei where the surface energy is given by Eq. (2.100), and the equilibrium value of k is determined by

$$\frac{\partial W_N(A, Z, k)}{\partial k} = 0, \qquad (2.114)$$

where in this condition, we consider ordinary nuclei under zero pressure. The values in the Eq. (2.69) together with $\sigma = 21.0$ MeV provides a good fitting to nuclear mass and radii over wide range of $A-$ and $Z-$values ($A \geq 40$).

Using Eqs. (2.113), (2.106), and (2.108), the generalized equilibrium conditions from Eq. (2.32) becomes

$$b_{\text{surf}}A^{2/3} = 2(w_{c,0}x^2 A^{5/3} + W_L) = 2w_c Z^2 A^{-1/3}. \qquad (2.115)$$

Note that at fixed $x, n_n, n_N A$, and $n_N V_N$, the neutron density n_n, the wave number k, and r_N/r_c remain fixed, while r_c scales as $A^{1/3}$. The Eq. (2.115) could be interpreted as "given the correct Z and A for the system in equilibrium, the surface energy per nucleus is exactly twice of the total Coulomb energy in Eq. (2.109)". Solving the Eq. (2.115) for the correct A as a function of x and r_N/r_c, we get

$$A = \frac{w_{\text{surf}}}{2w_c x^2} = \frac{w_{\text{surf}}}{x^2 \left(\frac{4}{5}\left(\frac{3}{\pi}\right)^{1/3} e^2 k\right)\left(1 - \frac{3}{2}\frac{r_N}{r_c} + \frac{1}{2}\left(\frac{r_N}{r_c}\right)^3\right)}. \tag{2.116}$$

The Eq. (2.116) relates A to k, k_n, x and the electron Fermi wave number k_e, since

$$u \equiv \left(\frac{r_N}{r_c}\right)^3 = V_N n_N = \frac{A}{n}\frac{n_e}{Z} = \frac{1}{2x}\left(\frac{k_e}{k}\right)^3. \tag{2.117}$$

Here and afterwards, by dropping the subscript N out, n refers to the number density of the inside nuclei. Then, using the β−equilibrium condition in Eq. (2.34), the relation for k_e in terms of A, k, k_n and x could be expressed by

$$\mu_e = k_e = (m_n - m_p) - \left(\frac{\partial b'}{\partial x} + 2w_c x A^{2/3} + \frac{\partial w_{\text{surf}}}{\partial x} A^{-1/3}\right), \tag{2.118}$$

where the effective volume energy per nucleon is

$$b' = b + b_{\text{exch}} + b_{\text{thick}}. \tag{2.119}$$

Additionally, using the Eq. (2.34), we can express the Eq. (2.118) as

$$k_e = (m_n - m_p) - \frac{\partial b'}{\partial x} - \frac{1}{x}\frac{\partial}{\partial x}(x w_{\text{surf}}) A^{-1/3}. \tag{2.120}$$

The last term on the right is explicitly A−dependent. Therefore, we can combine Eqs. (2.120), (2.117), and (2.116) into a simple cubic equation for $A^{2/3}$ in terms of x, k and k_n written as

$$(2 - 3\alpha + \alpha^2)A + 3v(1 - \alpha^2)A^{2/3} + 3v^2\alpha A^{1/3} - v^3 - \xi = 0 \tag{2.121}$$

where

$$\alpha = \frac{(m_n - m_p) - \partial b'/\partial x}{k(2x)^{1/3}} \tag{2.122}$$

$$v = \frac{\partial(x b_{\text{surf}})/\partial x}{k 2^{1/3} x^{4/3}} \tag{2.123}$$

$$\xi = \frac{5}{2}\left(\frac{\pi}{3}\right)^{1/3}\frac{w_{\text{surf}}}{x^2 e^2 k}. \tag{2.124}$$

The Eq. (2.121) could be solved directly by using the standard formula for cubic equations.

Next, to determine k and k_n as function of x, we need to reconsider the neutron chemical potential from Eq. (2.41) and pressure from Eq. (2.42) for both inside and outside nuclei. For densities below neutron drip, it is known that $k_n = 0$ and the only essential condition is $P^{(N)} = 0$.

Beyond the neutron drip where $\mu_n^{(N)}$ passes through zero, both Eqs. (2.41) and (2.42) could have a common solution. Therefore, in the free neutron gas

$$\mu_N^{(G)} = \frac{\partial}{\partial n_n}\left(n_n b(k_n, 0)\right) + \frac{nu}{1-u}\left(\frac{\partial b_{\text{thick}}}{\partial n_n} + A^{-1/3}\frac{\partial w_{\text{surf}}}{\partial n_n}\right) \tag{2.125}$$

and

$$P^{(G)} = n_n\left(\mu_N^{(G)} - b(k_n, 0)\right). \tag{2.126}$$

The neutron chemical potential in nuclei could be calculated by replacing $(\partial/\partial A)_Z$ with $(\partial/\partial A)_x + (dA/dx)(\partial/\partial x)_A = (\partial/\partial A)_x - (x/A)(\partial/\partial x)_A$ and applying on the Eq. (2.34). We obtain

$$\mu_n^{(N)} = \left.\frac{\partial}{\partial A}(W_N + W_L)\right|_{x, n_n, V_N, n_N} - m_n + x\mu_e. \tag{2.127}$$

After that, we use Eqs. (2.113), (2.109) and (2.101) for $W_N + W_L$. By substituting $(\partial/\partial A)_{V_N}$ with $(\partial/\partial A)_n + (n/A)(\partial/\partial n)_A$, we can calculate the bulk and surface contributions to $\mu_n^{(N)}$. This results in

$$\mu_n^{(N)} = \frac{\partial}{\partial n}(nb') + \left(\frac{5}{3}w_{\text{surf}} + n\frac{\partial w_{\text{surf}}}{\partial n}\right)A^{-1/3} + x(\mu_e - m_n + m_p). \tag{2.128}$$

The pressure on a nucleus given by the Eq. (2.43) could be rewritten as

$$P^{(N)} = n^2\frac{\partial}{\partial n}\left(\frac{W_N + W_L}{A}\right)\bigg|_{Z, A, n_n, n_N}. \tag{2.129}$$

From the Coulomb contribution to the Eq. (2.129) written as $-\frac{1}{3}r_N(\partial/\partial r_N)(w_c Z^2 A^{-1/3})$, the pressure could be expressed as

$$P^{(N)} = n^2\frac{\partial}{\partial n}b' + n^2\left(\frac{\partial}{\partial n}w_{\text{surf}}\right)A^{-1/3} + \frac{1}{3}nw_{c,0}x^2 A^{2/3}(1-u). \tag{2.130}$$

Note that the values of k and k_n could be completely determined by the equilibrium conditions $\mu_n^{(N)} = \mu_n^{(G)}$ and $P^{(N)} = P^{(G)}$.

Eventually, the EoS of nuclear matter in the free neutron regime could be determined from the Eq. (2.128) and (2.130) together. It is indeed a good assumption since the processes involving the free neutron and free-electron gases could change both A and Z. Then the deformed lattice structure would be suppressed at zero temperature. On the other hand, the lattice plays a significant role in determining thermal fluctuations. It is likely that the thermal fluctuation occurs in a neutron star at non-zero temperature, makes Z vary and deforms the lattice.

According to Ref. [49], the calculation of EoS of the free neutron nuclear matter based on [44] is accurate and agrees with results of density distributions from electron scattering; however, its calculation is time-consuming when applying the configuration up to 5,000 nucleons for each unit cell to determine EoS of the free neutron nuclear matter. Instead, the density matrix expansion method was used in Ref. [49] to estimate the EoS from 1.68×10^{12} g cm^{-3} up to around 5×10^{14} g cm^{-3} with very small differences, when compared to the original method.

Apart from free neutron and free electron gas at low densities, we could consider a possibility of free proton gas by considering the proton chemical potential from the data. However, according to the data from the Ref. [43], there is no proton drip since the proton chemical potentials inside nuclei are always less than that in the neutron gas.

2.3   Nuclear Matter at Intermediate Densities

In this section, we consider the extension of microscopic calculations for the EoS described by CET from 87.05 MeV fm^{-3} to higher densities the number density is around the nuclear saturation number density. Most of the descriptions of nuclear matter in this density range follows Ref. [45].

In the past, many EoSs of nuclear matter in the density range beyond $\rho \geq 1.55 \times 10^{14}$ g cm^{-3} (87.05 MeV fm^{-3}), commonly used in astrophysical modeling, could be obtained phenomenologically based on two-nucleon interaction. However, the two-nucleon interaction itself can not reproduce properties of nuclear matter around this density range due to strongly repulsive force at small relative distance.

Recently, there is the effective theory resulting from the 1$^{\text{st}}$ principle from quantum chromodynamics or QCD called the chiral-effective field theory (CET) that could be able to describe the nuclear matter in this range. Assuming that light quarks are approximately massless and therefore chirally symmetric, the CET could provide the framework for the nuclear matter at low energy that nucleons interact via exchanging pions. The outcome of approximation comes with great accuracy since the nucleons weakly interact from low to intermediate density. However, the higher-order correction terms from many nucleons e.g. 3N interaction contribution to the nuclear matter EoS become more and more important and necessary to compare the predicted values with the observed values e.g. nuclear symmetry energy as density increases to around the nuclear saturation number density.

According to Ref. [60], there is a theoretical uncertainty associated the neutron matter EoS described mainly by 2N interaction with 3N-interaction as higher order correction terms. Correspondingly, the dominant sources of the uncertainty lie within the c_i couplings where $i = 1, 3$, which could be determined from exchanging two-pion via three-nucleons interactions among neutrons without concerning interaction among the many-particle system. From πN, NN and the leading 3N interactions, $c_1 = -(0.7 - 1.4)$ GeV^{-1} and $c_3 = -(2.2 - 4.8)$ GeV^{-1} [60] generating the error band in energy per nucleon in Figure 2.2.

Generally, nuclear interactions depend on the energy scale Λ_E. Therefore, the Hamilto-
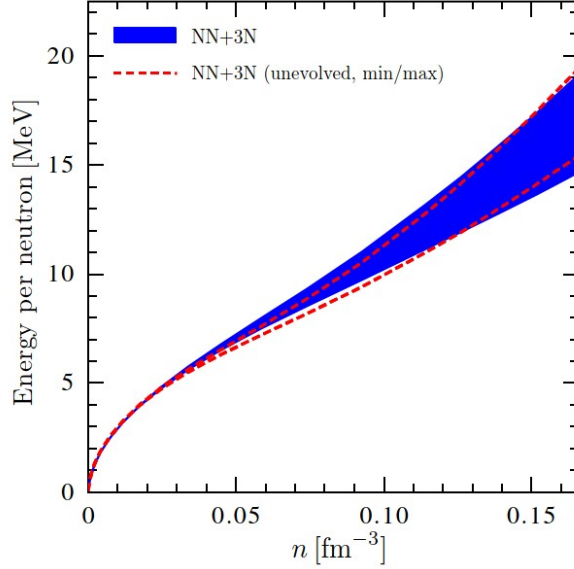
Figure 2.2: Energy per nucleon as a function of number density n, that the energy per nucleon based on two- and three-nucleon interactions with (without) a renormalization-group evolution to enhance the many-body convergence could be represented in blue strip (dashed red) where uncertainties in the low-energy coupling parameters c_1 and c_3 in 3N interactions the bounded area of the band, [60]: image from Ref. [45]

nian for nuclear interactions could be expressed as

$$H(\Lambda_E) = T + V_{\mathrm{NN}}(\Lambda_E) + V_{\mathrm{3N}}(\Lambda_E) + \dots \qquad (2.131)$$

where T, V_{NN} and V_{3N} are the kinetic energy, the potential energy with contribution from NN interactions, and that from 3N interactions, respectively. According to Ref. [45], with the renormalization group evolution of the NN interaction, we obtain a range of the energy scale as low-momentum cutoffs $\Lambda_E = 1.8 - 2.8$ fm^{-1}. This result is common to other long-range interactions from different potentials for pion physics. Consequently, the leading chiral 3N interactions are long-range and dominate the contribution to the 3N interactions. Therefore, we determine c_1 and c_3 by considering only the leading chiral term in 3N interactions with the low-momentum cutoffs.
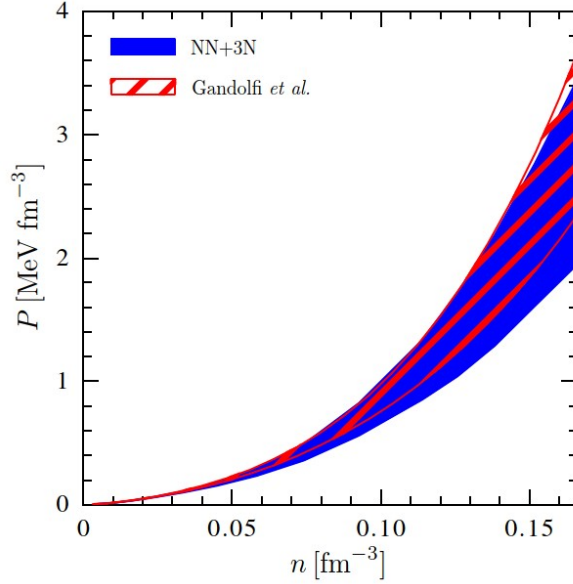
Figure 2.3: Pressure P of nuclear matter versus number density n, where the pressure could be represented by the the blue strip determined by two- and three-nucleon interactions with an evolution of renormalization group; the band shaded in red represents the pressure with the unevolved renormalization group from Gandolfi [61]: image from Ref. [45]

2.3.1 Asymmetric Nuclear Matter and Beta Equilibrium

According to Ref. [45], the total energy per nucleon ϵ, defined as a combination of the interaction energy and the kinetic energy, could be written in terms of $1 - 2x$ as:

$$
\begin{aligned}
\frac{\epsilon(\bar{n}, x)}{T_0} &= \frac{3}{5}\left[x^{5/3} + (1-x)^{5/3}\right](2\bar{n})^{2/3} - \left[(2\alpha - 4\alpha_L)x(1-x) + \alpha_L\right]\bar{n} \\
&\quad + \left[(2\eta - 4\eta_L)x(1-x) + \eta_L\right]\bar{n}^\gamma ,
\end{aligned}
\tag{2.132}
$$

where $x = Z/A = n_p/n$ and $\bar{n} = n/n_0$ stand for a proton fraction and a relative number density concerning the saturation density, respectively. At the saturation density, the Fermi energy for the symmetric nuclear matter is $T_0 = (3\pi^2 n_0/2)^{2/3}/(2m) = 36.84\,\mathrm{MeV}$. Note that the energy density defined in the Eq. (2.134) does not contain any contribution from rest masses.

Using thermodynamics relations, the corresponding pressure $P = n^2 \partial \epsilon/\partial n$ is given by

$$
\begin{aligned}
\frac{P(\bar{n}, x)}{n_0 T_0} &= \frac{2}{5}\left[x^{5/3} + (1-x)^{5/3}\right](2\bar{n})^{5/3} - \left[(2\alpha - 4\alpha_L)x(1-x) + \alpha_L\right]\bar{n}^2 \\
&\quad + \gamma\left[(2\eta - 4\eta_L)x(1-x) + \eta_L\right]\bar{n}^{\gamma+1} .
\end{aligned}
\tag{2.133}
$$

Note that we could evaluate the parameters α, α_L, η and η_L when the symmetric nuclear matter becomes saturated:

$$
\epsilon(\bar{n} = 1, x = 1/2) = -B = -16\,\mathrm{MeV} \quad \text{and} \quad P(\bar{n} = 1, x = 1/2) = 0
\tag{2.134}
$$

where $\gamma = 4/3$, $\alpha = 5.87$, $\eta = 3.81$, and a sensible incompressibility parameter

$$K = 9 \left. \frac{\partial^2 \epsilon(\bar{n}, x)}{\partial \bar{n}^2} \right|_{\bar{n}=1, x=1/2} = 236 \, \text{MeV} \, . \tag{2.135}$$

For the parametrizations on energy per nucleon in the Eq. (2.134) and pressure in the Eq. (2.133), we can evaluate the symmetry energy S_v and its derivative L as

$$S_v = \frac{1}{8} \left. \frac{\partial^2 \epsilon(\bar{n}, x)}{\partial x^2} \right|_{\bar{n}=1, x=1/2} \quad \text{and} \quad L = \frac{3}{8} \left. \frac{\partial^3 \epsilon(\bar{n}, x)}{\partial \bar{n} \partial x^2} \right|_{\bar{n}=1, x=1/2} . \tag{2.136}$$

We can adjust K by adjusting γ in the Eqs. (2.133) and (2.134). The symmetric energy and the derivative lightly count on γ and K since the leading term in the density derivative L. The

γ	K [MeV]	S_v [MeV]	L [MeV]
1.2	210	$29.7 - 32.8$	$32.4 - 53.4$
4/3	236	$29.7 - 33.2$	$32.5 - 57.0$
1.45	260	$30.1 - 33.5$	$33.6 - 56.7$

Table 2.2: Possible range for the symmetry energy S_v and the density derivative L predicted from different given γ values: table from Ref. [45]

parameter α_L and η_L could be evaluated by sampling given that ϵ and P fall inside the blue strips of the Figure 2.2 and Figure 2.3 for the number densities from $0.45 n_0$ to $1.1 n_0$. Consequently, the possible range for α_L and η_L represented in the Figure 2.4 are $\alpha_L = 1.18 - 1.59$ and $\eta_L = 0.64 - 1.11$.
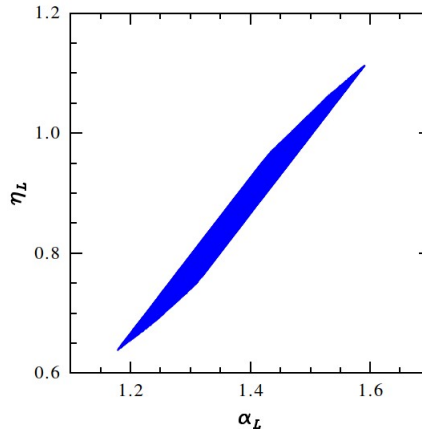
Figure 2.4: Possible range for α_L and η_L at the saturation density where the energy per nucleon and the pressure in the Eqs. (2.134) and (2.133) hold true: image from Ref. [45]

In $\beta-$equilibrium, we have a condition:

$$\mu'_n + m_n = \mu'_p + m_p + \mu'_e, \tag{2.137}$$

where μ_p', μ_n' and μ_e' are chemical potentials excluding rest mass contribution for proton, neutron and electron, respectively. We could determine the proton fraction x in beta equilibrium by minimizing a combination of the total energy per nucleon ϵ, the contribution of energy from electrons and the rest mass of the nucleons, with respect to the number density or in other words

$$\frac{\partial \epsilon(\bar{n}, x)}{\partial x} + \mu_e'(\bar{n}, x) - (m_n - m_p)c^2 = 0 \,. \tag{2.138}$$

For ultrarelativistic degenerate electron gas, $\mu_e'(\bar{n}, x) = (3\pi^2 x n_0 \bar{n})$. The allowed ranges for α_L

$n = n_0$	x	μ_n' [MeV]	μ_p' [MeV]
min	0.040	54.2	-58.0
max	0.053	51.9	-71.5
$n = n_0/2$	x	μ_n' [MeV]	μ_p' [MeV]
min	0.030	34.6	-46.1
max	0.033	34.3	-48.7

Table 2.3: Proton fraction x and chemical potentials μ_n' and μ_p' excluding contribution from rest mass in beta equilibrium for the saturation density n_0 and for $n_0/2$: table adapted from Ref. [45]

and η_L provide possible ranges for proton fraction, the rest-mass-subtracted chemical potentials of the neutron and proton in beta equilibrium at the saturation number density n_0 and for $n_0/2$ given in the Table 2.3, where the difference in neutron and the proton masses (1.3 MeV) is small and neglectable comparing with $\mu_e' \sim 100$ MeV. Obviously, c_1 and c_3 uncertainties result in possible ranges of α_L and η_L, and consequently imply the ranges of S_V and L.

2.3.2   Phase Transition from Nuclei to CET Nuclear Matter

In this section, we determine the criteria for the transition between dense neutrons described by CET and nuclei. Not only the neutron chemical potential but also the pressure must be continuous, while the mass density might have a discontinuous change. From the 1$^{\text{st}}$ law of thermodynamics, we have

$$\mu = \frac{\rho + P}{n_B} \tag{2.139}$$

where n_B refers to the total number density of baryons and ρ is density of the system. Actually, the chemical potential of baryon must be equal to that of the neutron at the transition. We can verify this claim by considering

$$\mu n_B = \sum_i \mu_i n_i \tag{2.140}$$

where the sum over the index i stands for the sum over all types of the particles present here. Consider that particle type i with charge Q_i, and baryon number B_i, thus

$$\mu_i = B_i \mu_n - Q_i \mu_e. \tag{2.141}$$

The condition above assures stability of particle i against $\beta-$decay. Substituting the Eq. (2.141) into the Eq. (2.140), we have

$$\mu n_B = \mu_n \sum_i B_i n_i - \mu_e \sum_i Q_i n_i \tag{2.142}$$

from charge neutrality $\sum_i Q_i n_i = 0$, while $\sum_i B_i n_i = n_b$; therefore, $\mu = \mu_n$. Accordingly, if we plot P vs μ, the more preferred state is the one with lower μ_n. Unfortunately, according to P and μ calculated in the Refs. [43] and [45], there is no obvious point that two curves cross.

The crucial part of the phase transition is that as the density of the CET nuclear phase decreases, instability against proton clustering increases. The presence of the instability could be observed by considering the variation of the total energy density concerning infinitesimal in densities; $\delta n_n(r), \delta n_p(r)$, and $\delta n_e(r)$. Due to relatively large spatial variation compared with the effective range of interaction, we consider only leading terms of the interacting energy up to 2nd order in δn by Thomas-Fermi expressions as a sum of Eq. (2.70) for the local bulk energy, Eq. (2.83) for the curvature terms, the electron energy and Coulomb energies. Thus from Ref. [44], concerning the Fourier transformation of variation in the number densities, the total Coulomb energy is

$$E_{\text{Coul}} = \frac{1}{2} \int \frac{d^3 q}{(2\pi)^3} \frac{4\pi e^2}{q^2} |\delta n_p(q) - \delta n_e(q)|^2, \tag{2.143}$$

and the curvature energy is given by

$$E_{\text{curv}} = \frac{1}{n_{NM}} \int \frac{d^3 q}{(2\pi)^3} q^2 [B_{nn}|\delta n_n|^2 + B_{pp}|\delta n_p|^2 + B_{np}(\delta n_p^* \delta n_n + \delta n_p \delta n_n^*)]. \tag{2.144}$$

The electron curvature energy could be neglected because of its small value. The local energy could be written up to second order as

$$
\begin{aligned}
E_{\text{loc}} &= E_0 + \int d^3 r [(\mu_n + m_n)\delta n_n(r) + (\mu_p + m_p)\delta n_p(r) + \mu_e \delta n_e(r)] \\
&+ \int d^3 r \left[\frac{\partial \mu_n}{\partial n_n}(\delta n_n(r))^2 + \frac{\partial \mu_p}{\partial n_p}(\delta n_p(r))^2 + 2\frac{\partial \mu_p}{\partial n_n}\delta n_p(r)\delta n_n(r) + \frac{\partial \mu_e}{\partial n_e}(\delta n_e(r))^2 \right],
\end{aligned}
\tag{2.145}
$$

where E_0 is the energy of the CET nuclear matter and $(\partial^2 nW/\partial n_n^2) = \partial\mu/\partial n_n$, and so forth. The derivatives with respect to n_n act at the fixed n_p and vice versa, unless indicated explicitly. With $\beta-$equilibrium condition and charge neutrality:

$$\int d^3 r (n_p(r) - n_e(r)) = 0, \tag{2.146}$$

the first-order term becomes $(\mu_n + m_n)\delta \int d^3 r (n_p(r) + n_e(r))$. Additionally, if the variations preserve the total baryon number $\int d^3 (n_n(r) + n_p(r))$, the first-order term disappears.

The instability could exist if the energy is lower than E_0, given that the density is inhomogeneous. Thus, minimizing the local energy with respect to $\delta n_n(r)$ and $\delta n_e(r)$, we obtain the following conditions

$$\left(\frac{\partial \mu_n}{\partial n_n} + \frac{2B_{nn}q^2}{n_{NM}}\right)\delta n_n(q) + \left(\frac{\partial \mu_p}{\partial n_n} + \frac{2B_{np}q^2}{n_{NM}}\right)\delta n_p(q) = 0 \qquad (2.147)$$

and

$$\frac{\partial \mu_e}{\partial n_e}\delta n_e(q) = \frac{4\pi e^2}{q^2}(\delta n_p(q) - \delta n_e(q)). \qquad (2.148)$$

After solving for δn_n and δn_e in terms of δn_p, the variation of the total energy is assumed to take the form

$$E - E_0 = \frac{1}{2}\int \frac{d^3q}{(2\pi)^3}v(q)|\delta n_p(q)|^2 \qquad (2.149)$$

where

$$v(q) = v_0 + \beta q^2 + \frac{4\pi e^2}{q^2 + k_{\mathrm{FT}}^2}. \qquad (2.150)$$

Note that k_{FT} is given by Eq. (2.111) with $k_e = (3\pi^2 nx)^{1/3}$, on the other hand,

$$v_0 = \frac{\partial \mu_p}{\partial n_p} - \frac{(\partial \mu_p/\partial n_n)^2}{(\partial \mu_n/\partial n_n)} \equiv \left(\frac{\partial \mu_p}{\partial n_p}\right)\Bigg|_{\mu_n, n_e}, \qquad (2.151)$$

$$\beta = \frac{2}{n_{NM}}(B_{pp} + 2B_{pn}\zeta + B_{nn}\zeta^2), \qquad (2.152)$$

$$\zeta = -\frac{\partial \mu_p/\partial n_n}{\partial \mu_n/\partial n_n}. \qquad (2.153)$$

For $\zeta \approx 2$, the system of CET nuclear matter becomes unstable as the fluctuation in density of proton is about twice that of the neutron with the same sign. Note that,

$$v(q) \to \left(\frac{\partial \mu_p}{\partial n_p}\right)\Bigg|_{\mu_n, \mu_e}, \qquad (2.154)$$

as $q \to 0$. The second order derivative of $v(q)$ at $q = 0$ becomes $2(\beta - 4\pi e^2/k_{\mathrm{FT}}^4)$ and is always negative in the CET neutron, because

$$\frac{4\pi e^2}{k_{\mathrm{FT}}^4} = \frac{\pi}{12}\left(\frac{1}{e^2\mu_e nx}\right) \gg \beta \sim \frac{10^2 \mathrm{MeV}\cdot\mathrm{fm}^2}{n_{NM}}. \qquad (2.155)$$

Consequently, $v(q)$ is minimum at $q = Q$, which is given by

$$Q^2 = \left(\frac{4\pi e^2}{\beta}\right)^{1/2} - k_{\mathrm{FT}}^2. \qquad (2.156)$$

It was found in the table 8 of Ref. [43] that the corrections from Coulomb energy and curvature energy contribute to suppress the instability until $v_{\min}(> v_0)$ becomes negative. The critical density could be determined by the following condition:

$$v(Q) \equiv v_{\min} = v_0 + 2(4\pi e^2\beta)^{1/2} - \beta k_{\mathrm{FT}}^2, \qquad (2.157)$$

From the given data, v_0 becomes negative for density $\rho \leqslant 3.2 \times 10^{14}$ g/cm^3 since the correction terms of Coulomb energy and that of curvature energy that tend to suppress the instability, vanishes. The critical density, where $v(q) = 0$, denoted by ρ_i, could be determined from

$$v_0 + 2(4\pi e^2 \beta)^{1/2} - \beta k_{\mathrm{FT}}^2 = 0. \tag{2.158}$$

The value of v_0 is necessary set by the derivative

$$\left(\frac{\partial \mu_n}{\partial n_n} \right)_{\mathrm{free}} = \frac{\pi^2}{2^{1/3} m_n k}, \tag{2.159}$$

for a free neutron gas. At $k = 1.35$ fm^{-1}, $(\partial \mu_n / \partial n_n)|_{\mathrm{free}} = 240$ MeV·fm^3.

Due to inhomogeneity in the density distribution, the coefficient β could be described quantitatively by

$$\beta = 2(Q_{pp} + 2Q_{np}\zeta + Q_{nn}\zeta^2), \tag{2.160}$$

where $Q_{ij} \equiv B_{ij}/n_0$. Consequently, we could numerically predict that the baryon number density, where the instability occurs, is around $\bar{n} = 0.55 - 0.625$ without Coulomb and density gradient contribution ($Q = 0$) and $\bar{n} = 0.475 - 0.55$ when including Coulomb and density gradient contribution ($Q = 75$ MeV·fm^5), according to Ref. [45]. Correspondingly, around $\rho < \rho_s/2$, the CET neutron becomes unstable. Note that from Ref. [45], $\rho_s \equiv \rho(n_0) = 150.3$ MeV fm^{-3}(2.67×10^{14}g cm^{-3}) is the density defined at nuclear saturation number density $n_0 \equiv 0.16$ fm^{-3} where nucleons begin to touch each other. Hence, there will be a 1$^{\mathrm{st}}$-order phase transition from CET neutron to the more stable nuclei, as density decreases below $\rho_s/2$.

2.4 General Extension for CET EoS

According to Ref. [45], as the densities of nuclear matter exceed the regime that could be described by the leading chiral terms of 3N interactions or $\rho > \rho_1 = 1.1\rho_s = 165.3$ MeV·fm^{-3}(2.94×10^{14} g cm^{-3}), the EoS defined in Section 2.3 is no longer reliable. Therefore, we need to broaden the EoS beyond this density. In this section, we follow the suggestions from Ref. [45] that the extension beyond the transition density ρ_1 could be expressed in a series of general polytropic extension that the pressure P is written as a connected piecewise polytrope $P(\rho) = \kappa \rho^\Gamma$ where the adiabatic index $\Gamma \equiv \frac{\rho}{P} \frac{\partial P}{\partial \rho}$. The extension of EoS could be divided into 3 different regions, see Figure 2.5. The density region 1: $\rho_1 \leq \rho \leq \rho_{12}$; region 2: $\rho_{12} \leq \rho \leq \rho_{23}$; region 3: $\rho \geq \rho_{23}$, respectively. The range polytropic exponents are set as $1.0 \leqslant \Gamma_1 \leqslant 4.5$ for the first region; $0.0 \leqslant \Gamma_2 \leqslant 8.0$ for the second region; and $0.5 \leqslant \Gamma_3 \leqslant 8.0$ for the third region, respectively. For density limits between polytropes, ρ_{12}, and ρ_{23}, it is sensible to set $1.5\rho_s \leqslant \rho_{12} < \rho_{12} < \rho_{\max}$ with a step size of $0.5\rho_s$. Lastly, the values of Γ_i and ρ_{ij} are constrained by results from nuclear physics and observations.
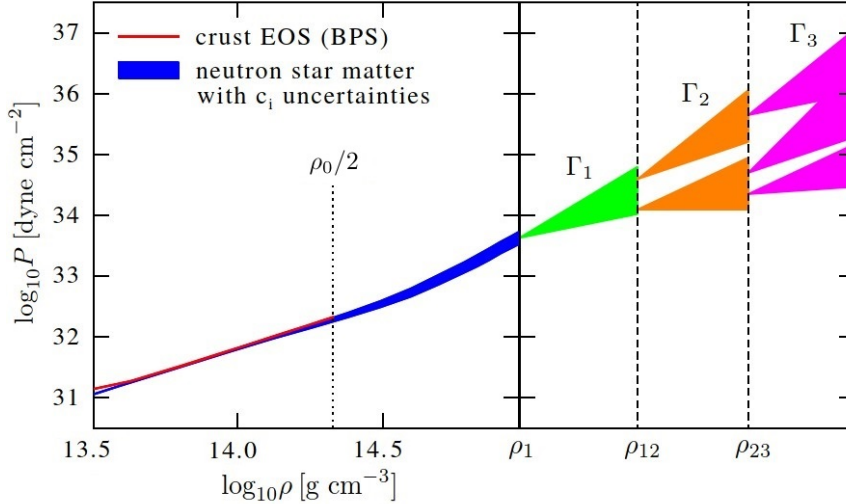
Figure 2.5: Pressure P of the nuclear matter as a function of mass density ρ: A part on the left in red is from BPS EoS of nuclear matter [43] for density $\rho < \rho_0/2$. The middle part is the blue band with c_i uncertainties for the CET nuclear matter for $\rho_s/2 \geq \rho \geq \rho_1 \equiv 1.1\rho_s$. On the right, the general extension are represented into 3 different regions: image adapted from Ref. [45]

2.4.1 Constraints on The EoSs of Extended CET Nuclear Matter

The connected piecewise polytropic extension, defined in the given range in the previous section, would be employed to generate lots of EoSs at higher density. Then we implement the extended polytropic EoSs into the Tolman-Oppenheimer-Volkov equations and keep only those that satisfy the following 2 constraints:

- The speed of sound inside the nuclear matter must be less than the speed of light for all densities: $v_s(\rho) = \sqrt{dP/d\rho} < 1$ (in natural units).

- The neutron star mass M from the extended EoSs equals the heaviest mass $\hat{M}$ observed from neutron stars.

Note that there are 2 choices for the heaviest known neutron star: $\hat{M} = 1.97 M_\odot$ [2] and $\hat{M} = 2.40 M_\odot$ [62]. The latter are from black widow pulsar $B1957 + 20$ containing large uncertainties. The Figure 2.6 represents the individual EoS that satisfy both constraints for the 2 cases. The higher pressure generated by the EoSs, the stronger EoS is excluded because of the causality and the mass measurement results. Additionally, the EOSs with large polytropic exponents are strongly constrained by causality, therefore the maximal densities are limited while the softer EoSs, the larger central densities. For $M = 1.97 M_\odot$, the maximal central density is $\approx 8.3\rho_s$ while for $M = 2.40 M_\odot$, the maximal density reaches only $\approx 5.8\rho_s$.
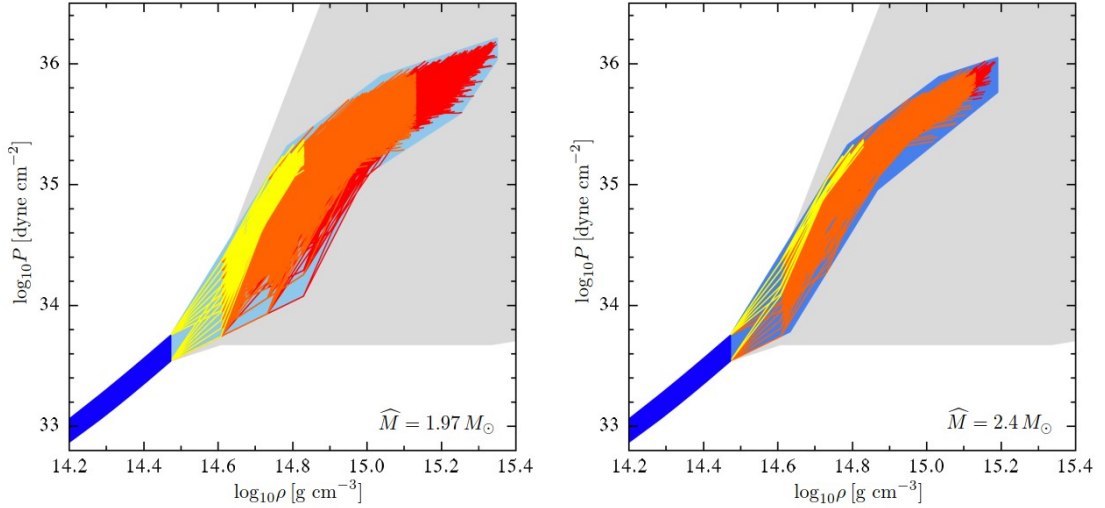
Figure 2.6: Pressure P of the nuclear matter as a function of mass density ρ: The blue band at low density is for CET nuclear matter with c_i uncertainties. The gray area shows all possible polytropic extensions, while that in aqua shows all EoSs that satisfy the causality condition and support a neutron of mass $\hat{M} = 1.97 M_\odot$ (left panel) and $\hat{M} = 2.40 M_\odot$ (right panel). Additionally, lines represent EoSs are labeled with colours to indicate the central density: yellow for $\rho_c \leqslant 2.5\rho_s$, orange for $2.5\rho_s \leqslant \rho_c \leqslant 5\rho_s$ and red for $\rho_c \geqslant 5\rho_s$: image from Ref. [45]
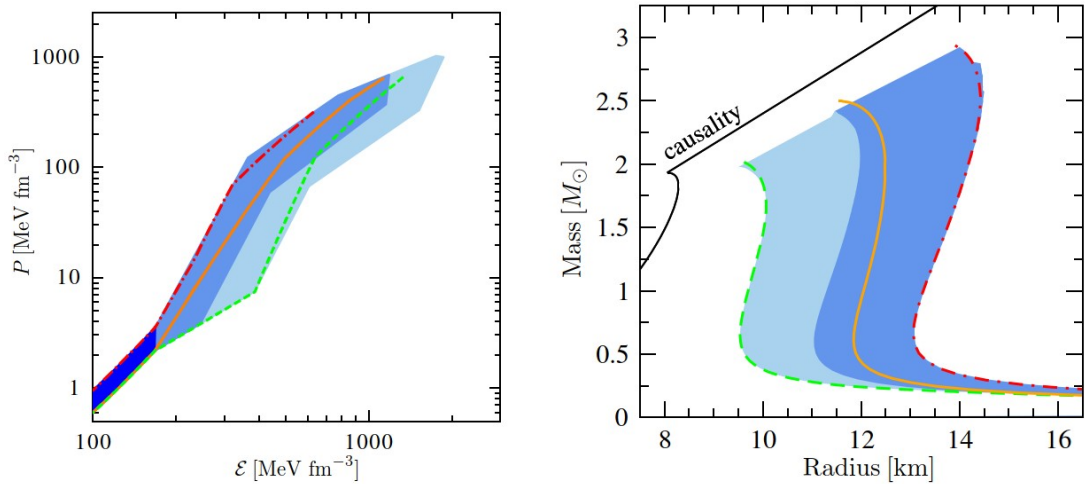
Figure 2.7: Three possible representative EoSs for Extended CET nuclear matter displayed in a plot between pressure P and energy density ϵ with the uncertainty bands. The corresponding mass-radius relation for the three Extended CET nuclear matter EoSs: image from Ref. [45]

As mentioned earlier, the uncertainty bands in the P vs ρ plots indicate that there are many possible individual EoSs. Therefore, these possibilities could be represented by three representative EoSs: stiff (red), intermediate (orange) and soft (green) extended CET EoS, as

shown in the Figure 2.7. We will define the general extension for CET EoSs in Chapter 4 numerically in great detail.

CHAPTER III

Holographic QCD and

Holographic Multiquark

In this chapter, we consider a brief review of the fundamental properties of QCD, including asymptotic freedom, chiral symmetry breaking, confinement-deconfinement transition. Then, we review a gauge-gravity duality and consider how the duality emerges from the study of superstrings theories and branes. Next, there would be a review of holographic QCD followed by the Sakai-Sugimoto model, a specific holographic QCD model, as the most similar holographic model compared to the real QCD. After that, we focus on the holographic descriptions for baryons and mesons. Lastly, in this chapter, we consider the holographic multiquark and the thermodynamics of the multiquark state.

3.1   A Brief Review of QCD

According to the quark model of hadrons, there are 6 flavours (types) of quarks in the model namely: up, down, charm, strange, top, and bottom. Nevertheless, their interactions are independent of their flavour. Instead, they are dependent on another quantum number called "colour". These are not actual colours. However, they have some analogies with a combination of 3 colours of light, so that a combination of red, green and blue quarks results in a colourless state. Generally, the interactions between quarks could be described by Quantum Chromodynamics or QCD. It is a quantum non-abelian gauge field theory based on the quark model where quarks interact with each other by exchanging colour charges via gluons. Additionally, the interaction range between quarks is very short. Peculiarly, their interacting strength could be described by a QCD coupling parameter, α_s, which decreases as the energy scale increases. It is known as asymptotic freedom in QCD. This implies that at low energy the coupling strength becomes very large. Then quarks are confined within hadrons with the colourless bound state condition for the stable hadrons. This is also known as colour confinement.

At a very high energy scale, results from perturbative calculations in QCD becomes

accurate and precise, especially when the energy scale reaches beyond around 200 GeV since the QCD coupling becomes weak, $\alpha_s \leq 0.1$[63]. Therefore, in this range of energy, QCD becomes perturbative, which is called "perturbative QCD" or in short "pQCD". Only leading terms or tree levels in the perturbative expansion are enough to determine various properties of interactions among quarks. To be specific, based on observational data, the temperature for the quark deconfinement is around 150 MeV or 1.7×10^{12} K [64]. This is also known as " Hagedorn temperature". Above the Hagedorn temperature, quarks and gluons become free from the bound state and turn into quark-gluon plasma (QGP).

There are many important symmetries associated with the QCD Lagrangian both continuous symmetries e.g. Lorentz symmetry, and discrete symmetries e.g. $SU(3)_{\text{colour}}$ gauge symmetry describing the interaction between quarks by exchanging colour charge via the gluons. In the language of the field theory, symmetries associated with Lagrangian determine conserved quantities or conservation laws. Any spontaneous symmetry breaking leads to the existence of massive Goldstone bosons. Therefore, for the exact $SU(3)_{\text{colour}}$ symmetry gluons are all massless. Another important discrete symmetry is an approximate $SU(3)_R \times SU(3)_L$ chiral flavour symmetry of light quarks (u, d, s). Since the masses of the light quarks are small, light quarks are all approximated to be massless called chiral quarks. However, at a low energy regime, especially when the energy scale falls below 0.1 GeV, QCD becomes strongly coupled and therefore breaks the chiral flavour symmetry. The broken $SU(3)_R \times SU(3)_L$ chiral flavour symmetry of light quarks (u, d, s) leads to the mass generation of nucleons from the elementary light quarks. According to mass parameters in QCD, masses of free light quarks are very small $(2.2, 4.7, 93$ MeV for u, d, s, respectively) compared to nucleons mass ($m_p \approx 938$ MeV). Combining 2 up and 1 down valence quarks only give 9.1 MeV which is less than 1% of m_p. The broken chiral symmetry accounts for approximately 99% of nucleons masses. Additionally, pseudo-Goldstone bosons are associated with chiral symmetry breaking. The explicit symmetry breaking occurring at a low energy scale generates pseudo-Goldstone bosons e.g. π mesons as effective interacting particles between nucleons.

At low energy, QCD becomes non-perturbative. Fortunately, the chiral effective field theory (CET), as the effective theory for QCD, is still perturbative. Normally, the characteristics of pseudo-Goldstone bosons might be determined by expanding CET around the perfectly symmetric theory in terms of explicitly broken symmetry parameters. Other theoretical tools for the strongly coupled gauge theory are lattice QCD approaches. They are well-established with nonperturbative QCD but their numerical processes require very high computing performance. For the review of CET and Lattice QCD, see Refs. [65] and [66], respectively.

3.2   Gauge/String Duality

During the development of 2nd evolution of the superstring theories, the discovery of the AdS/ CFT correspondence [20] resulted in a significant tool for strongly coupled gauge theories. Remarkably, two theories specified in different dimensions are conjectured to be equivalent to each other with a strong-weak duality is one of the most fascinating characteristics of the gauge/string duality. As a result, this duality is commonly referred to as a "holographic duality," and the description from string theory that is similar to that in QCD is referred to as "holographic QCD." Hadrons in holographic QCD are defined by higher-dimensional structures using open strings and D-branes wrapped around a non-trivial cycle in the particular background. Using this duality, we could study the properties of hadrons at low energy.

Before delving into the fundamental concept of duality, we must first introduce an object in perturbative superstring theories, namely strings and non-perturbative objects known as D-branes. String theory uses a 10-dimensional string instead of a point particle to represent the fundamental state of matter. A Dp-brane is a $(p+1)$ dimensional object that connects the ends of open strings. The open strings attached to the flat Dp-brane contain massless modes that characterise $U(1)$ gauge particles living on it. As a result, a $U(1)$ gauge theory becomes fully aware of in $(p+1)$ dimensions. The gauge group is also upgraded to $U(Nc)$ when Nc Dp-branes are introduced in the same place.

At low energy, the coupling strengths of string theories become weak in the system consisting of open strings connected to the D-branes decouples from gravity. The effective theory of the system becomes $U(N_c)$ supersymmetric theory. However, since D-branes typically couple with gravity, spacetime is indeed curved. It is shown that the D-branes could be accurately characterised as the equivalent curved background using a specific parameter. As a result, we have two descriptions of the D-branes. In flat spacetime, one of these comes from gauge theory, while in curved spacetime, the other from string theory. It is anticipated that these two definitions are equivalent because they both describe the same D-brane system.

The most studied gauge/string duality is the AdS/CFT duality [20]. It is a duality between two theories: type IIB superstring theory in Anti-de Sitter(AdS) background and 4-dimensional or 4-Dim supersymmetric Yang-Mills theory, both attempting to describe the same D3-branes system. Rigorously, AdS/CFT duality could be described as follows: "the weakly coupled type IIB superstring theory on the $AdS_5 \times S^5$ background at near horizon limit is identical to the strongly coupled $SU(N_c)$ supersymmetric Yang-Mills theory in 4-Dim at low energy limit.".

3.3 Holographic QCD

In this part, we take a quick look into holographic QCD, which incorporates the notion of gauge/gravity duality. Most of the review of holographic QCD here follows [67]. The following descriptions will show how a low energy effective theory of hadrons could be obtained, and especially how mesons and baryons could be realized from string theory.

Applying AdS/CFT duality to QCD can be done in D3/D7 branes system. There are N_c D3 colour branes, representing interactions between quarks while N_f D7 flavour branes, representing the existence of flavours in QCD, are added into the system as probe branes in which its backreaction can be neglected. Correspondingly, mesons and baryons are replaced by open strings connected on N_c D3-branes and open strings connected from N_c D3-branes to N_f D7-branes [22].
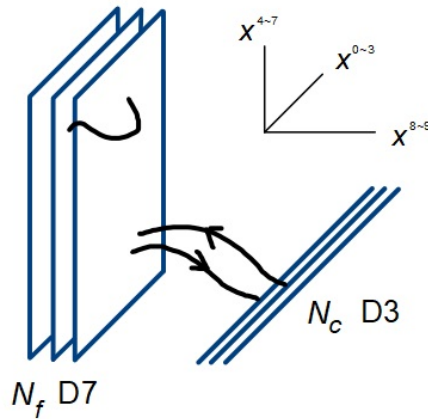
Figure 3.1: Mesons and Baryons in AdS/QCD

The AdS/QCD is modified further by adding black D3 branes as a cut off to the system (hard-wall model) to mimic confinement/deconfinement phase transition. However, chiral symmetry breaking, one of the key aspects of QCD, is still not well captured by this system.

3.3.1 Witten-Sakai-Sugimoto Model

In 1998, E. Witten proposed using N_c D4-branes extended along $x^{0\sim4}$ directions (world volume directions), with an S^1 compactification with an anti-periodic boundary condition in the x^4 direction as a holographic description of pure Yang-Mills[21]. Therefore, the shape of N_c D4-branes becomes like a hollow cylinder where the tube extends along $x^{5\sim9}$ axial directions (transverse directions).

The supersymmetry is completely broken by the anti-periodic boundary condition, and $U(N_c)$ Yang-Mills theory is realised as the effective theory of the open strings attached to the

D4-branes at low energy. To make quarks appear in the system, Sakai and Sugimoto [26] insert
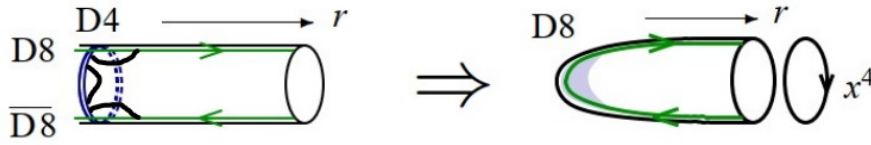
Figure 3.2: Replacement of D4-brane with the matching curved background: image modified from Ref. [68]

N_f D8-$\overline{\text{D8}}$ pairs stretched in $x^{0\sim3}$ and $x^{5\sim9}$ directions. In the compactified direction x^4, the D8-branes and $\overline{\text{D8}}$-branes are inserted at antipodal points or opposite points in the circle S^1. (See on the LHS of Figure 3.2. A modification of the antipodal positions of the D8- and $\overline{\text{D8}}$-branes could be found later in Refs. [4, 29])

When the D4- and D8 (or $\overline{\text{D8}}$)-branes are connected through open strings, the N_f massless modes of the $U(N_c)$ group turn into N_f massless quarks in $U(N_c)$ QCD with at a low energy limit. Accordingly, the corresponding chiral symmetry in QCD is realised in the D8-$\overline{\text{D8}}$ system with a $U(N_f)_L \times U(N_f)_R$ group. By replacing the D4-branes with the corresponding curved background, the D8-$\overline{\text{D8}}$ become connected. This is a basic setup for holographic QCD in Sakai-Sugimoto(SS) model.

In the system, there are two key parameters. . The first is the radius of the S^1, indicated as M_{KK}^{-1}, and the second is the 't Hooft coupling $\lambda = g_{\text{YM}}^2 N_c$. Note that we cannot interpret particles in Kaluza-Klein (KK) modes with masses of order M_{KK} as real particles in QCD. As a result, M_{KK}, must be regarded as a cutoff for the model. The theory may be considered as QCD below the cutoff.

Accordingly, the topology of the spacetime becomes $\mathbf{R}^{1,3} \times \mathbf{R}^2 \times S^4$, where $\mathbf{R}^{1,3}$ and $\mathbf{R}^2$ factors are parametrized by $x^{0\sim3}$ and (r, x^4), correspondingly, while S^4 represent the 4-sphere in the $x^{5\sim9}$ directions. Since the D8-branes are considered as a probe, the backreaction to the spacetime could be ignored. This is known as probe approximation and valid when $N_c >> N_f$. Hence, $U(N_f)_L \times U(N_f)_R$ turns into $U(N_f)$. This leads to a broken chiral symmetry in QCD. Attachment of open strings is required when the D4-brane is wrapped around the 4-sphere S^4 due to the RR current in the background.

Hadrons are beautifully realized in the Sakai-Sugimoto model. As seen in Figure 3.3, mesons and baryons in the model could be represented by open strings connected to the intersection between D4- and D8-branes or D4/D8 branes and D4-branes wrapped on S^4, correspondingly.When connected to the D4/D8-branes, each open string holds two flavour indices; therefore, the system of open strings and D4/48-branes could consistently represent mesons. Despite not stating the details here, it has been investigated that the D4-brane wrapped on the
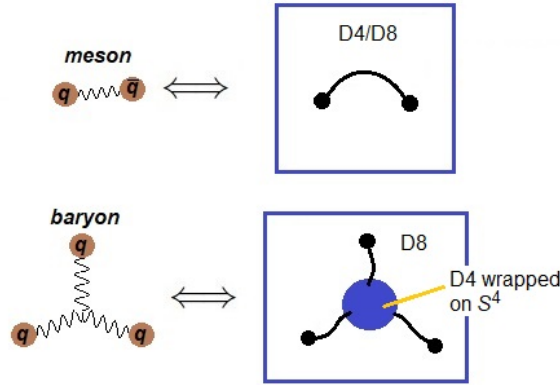
Figure 3.3: Hadrons in the model: image modified from Ref. [67]

S^4 has to have N_c open strings attached to it because of the RR flux in the background [21, 69]. Due to the RR current in the background [21, 69], there must be N_c open strings attached to the wrapped D4-brane on S^4. Hence, the higher dimensional object could be interpreted as quarks in large N_c QCD.

3.3.2 Mesons

The effective theory of open strings attached to the D4/D8-branes may be used to represent mesons. We could determine the 5-Dim $U(N_f)$ gauge theory by starting with the effective D8-brane action and then integrating it over the S^4 direction:

$$S_{\text{5-Dim}} \simeq S_{\text{YM}} + S_{\text{CS}}, \tag{3.1}$$

where

$$
\begin{aligned}
S_{\text{YM}} &= \kappa \int d^4x dz \text{Tr}(\frac{1}{2}h(z)F_{\mu\nu}^2 + k(z)F_{\mu\nu}^2), \\
S_{\text{CS}} &= \frac{N_c}{24\pi^2}\int_{\text{5-Dim}} \omega_5(A),
\end{aligned}
\tag{3.2}
$$

and $h(z) = (1 + z^2)^{-1/3}$ and $k(z) = 1 + z^2$ where $\mu, \nu = 0, \dots, 3$ refer to the four dimensional coordinates, and z is an extra-dimension in the worldvolume. The factor κ in S_{YM} scales as λN_c, while $\omega_5(A)$ in S_{CS} represents the Chern-Simon 5-form field. According to the holographic setup, the 5-Dim gauge could be expressed as

$$
\begin{aligned}
A_\mu(x^\mu, z) &= \sum_{n\geq 1} B_\mu^{(n)}(x^\mu)\psi_n(z), \\
A_z(x^\mu, z) &= \sum_{n\geq 0} \varphi^{(n)}(x^\mu)\phi_n(z),
\end{aligned}
\tag{3.3}
$$

where we use complete sets $\{\psi_n\}_{n\geq 1}$ and $\{\phi_n\}_{n\geq 0}$ as functions of z to expand the 5-Dim gauge field with $B_\mu^{(n)}$ and $\varphi^{(n)}$ representing 4-Dim vector and scalar fields, respectively. Note that by

absorbing $\varphi^{(n)}$, the vector field $B_\mu^{(n)}$ becomes massive, but mass of $\varphi^{(0)}$ remains zero. Correspondingly, the isovector particles such as $B_\mu^{(1)}$, $B_\mu^{(2)}$, $B_\mu^{(3)}$ could be interpreted as the ρ-meson, a_1-meson, ρ'-meson, respectively, while the scalar particle $\varphi^{(0)}$ could also be interpreted as the pion. Additionally, parity, spin, and charge conjugation also agree with the clarification. Additionally,since the pions are the Goldstone bosons with the spontaneous chiral symmetry breaking, then $\varphi^{(0)}$ could be interpreted as the pion field. Those pions should be massless given that they are composed of massless quarks.

Applying the expansions in Eq. (3.3) to the 5-Dim action in Eq. (3.2) then integrating over z, we could attain an effective action of the traditional mesons in 4-Dim as:

$$S_{\text{5-Dim}} \simeq S_{\text{4-Dim}}(\pi, \rho, a_1, \rho', a_1'). \tag{3.4}$$

Meson's masses and the couplings associated with interactions among the meson multiplets can be determined from the effective action in Eq. (3.4). The eigenequation for the mesons $B_\mu^{(n)}$ could be achieved when choosing the complete set $\{\psi_n\}_{n \geq 1}$ as a set of eigenfunctions that satisfy

$$-h(z)^{-1}\partial_z(k(z)\partial_z\psi_n(z)) = \lambda_n\psi_n(z), \tag{3.5}$$

where the eigenvalue for Eq. (3.5) is λ_n. Consequently, their mass are expressed as $\sqrt{\lambda_n}M_{\text{KK}}$. Accordingly, it can be shown that the eigenvalues $\lambda_n (n = 1, 2, 3, \dots)$.

Choosing $0 < \lambda_1 < \lambda_2 < \dots$, the coupling constants could be determined from Eq. (3.4). For instance, the coupling $g_{\rho\pi\pi}$ for $\rho - \pi - \pi$ interaction is

$$g_{\rho\pi\pi} = \frac{1}{\pi} \int dz k(z)^{-1}\psi_1(z). \tag{3.6}$$

Masses and couplings are evaluated numerically and some of the results have been reported in Table 3.1 and Table 3.2 below.

mass	SS model	experiment
ρ	[776 MeV]	776 MeV
a_1	1189 MeV	1230 MeV
ρ'	1607 MeV	1465 MeV

Table 3.1: Masses in the SS model: table from Ref. [67]

coupling	SS model	experiment
f_π	[92.4 MeV]	92.4 MeV
L_1	0.58×10^{-3}	$(0.1 \sim 0.7) \times 10^{-3}$
L_2	1.2×10^{-3}	$(1.1 \sim 1.7) \times 10^{-3}$
L_3	-3.5×10^{-3}	$-(2.4 \sim 4.6) \times 10^{-3}$
L_9	8.7×10^{-3}	$(6.2 \sim 7.6) \times 10^{-3}$
L_{10}	-8.7×10^{-3}	$-(4.8 \sim 6.3) \times 10^{-3}$
$g_{\rho\pi\pi}$	4.8	6.0
g_ρ	0.16 GeV^2	0.12 GeV^2
$g_{a_1\rho\pi}$	4.6 GeV	$2.8 \sim 4.2$ GeV

Table 3.2: Couplings in the SS model: table from Ref. [67]

Additionally, the 5-Dim action of meson obtained in Eq. (3.4) could reproduce a lot of former phenomenological models of hadrons. For more information see Ref. [67].

3.3.3 Baryons

As mentioned earlier, baryons can be represented by the wrapped D4-branes on S^4. In fact, a soliton in the gauge theory could be realised on the D4/D8-brane system [71]. In the Sakai-Sugimoto (SS) model, 5-Dim gauge theory, baryons can be described as a soliton with the instanton number is given by

$$\frac{1}{8\pi^2} \int_{R_4} \text{Tr}(F \wedge F) = N_B, \tag{3.7}$$

where R_4 is the 4-Dim space parameterized by $\{(x^{1\sim3}, z)\}$ and N_B could be interpreted as the baryon number. Equivalently, the existence of solitons as the Skyrme model's description of baryons or Skyrmions [72, 73] emerges from a specific configurations in the 5-Dim non abelian gauge theory. Various characteristics of baryons can be analysed using the techniques in the Skyrme model [74]. Eventually, the baryon's spectrum could be acquired as in Figure 3.4.

The numerical result of the baryon spectrum (LHS of Figure 3.4) resembles that of the parameters from the experimental data (RHS of Figure 3.4). For instance, the lightest and second lightest baryons are the states with $J^P = \frac{1}{2}^+$ and $J^P = \frac{3}{2}^+$, respectively, the second lightest baryon with $J^P = \frac{1}{2}^+$ ($J^P = \frac{3}{2}^+$) and the lightest one with $J^P = \frac{1}{2}^-$ ($J^P = \frac{3}{2}^-$) are almost degenerate, etc. It should be emphasized that the latter feature the latter property had been a puzzle in hadron physics since it denies the naive analysis based on the quark model.
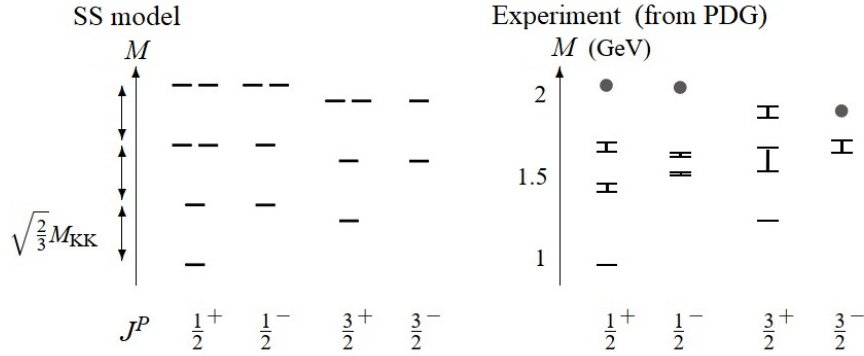
Figure 3.4: Baryons spectrum in the SS model: image from Ref. [67]

3.4 Holographic QCD for Deconfined Matter

We have already mentioned the holographic configuration that could represent mesons and baryons in the former sections. However, apart from mesons and baryons, the deconfined states of quarks could be described by the holographic model at temperatures above the deconfinement as well. In this section, we provide descriptions for a deconfined matter based on the holographic SS model from Ref. [4].

According to Ref. [4], the D4/D8/$\overline{\text{D8}}$-brane configurations that the positions of D8 and $\overline{\text{D8}}$ branes are generalized so that they are not necessary to be antipodal but separated by L_0. Accordingly, there are 3 stable configurations in the deconfined phases (see in Figure 3.5) based on the force balance condition:

(a) the parallel configuration of both D8- and $\overline{\text{D8}}$-branes representing the quark-gluon plasma χ_S-QGP,

(b) the connected D8/$\overline{\text{D8}}$ without sources in the bulk interpreted as the vacuum state,

(c) the connected D8-$\overline{\text{D8}}$ branes with the D4-brane as the baryon vertex embedded in the middle of the D8 and $\overline{\text{D8}}$ describing the multiquark state.

3.4.1 Holographic Multiquark Configuration

As indicated in Ref. [4], the D4 baryon vertex that represented baryon could be generalized further by many possible rearrangements of how strings join the vertex. It was found that holographic multiquark is a stable holographic configuration for deconfined QCD matter by considering the balancing force condition. The holographic multiquark could be described by the holographic structure that consists of the total number of strings N_c attached to the D4/
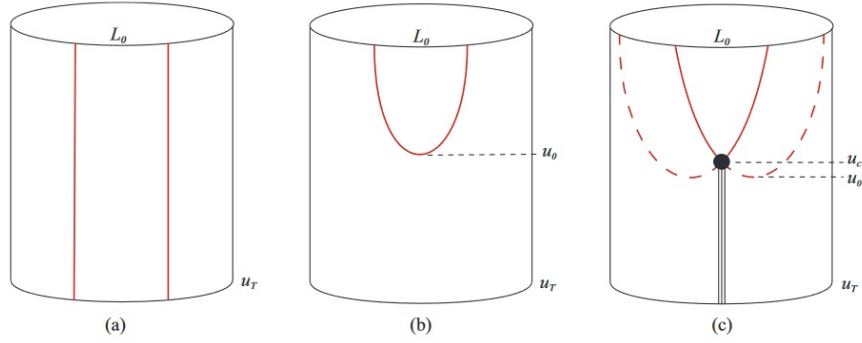
Figure 3.5: Deconfined matter the SS model: image from Ref. [4]

D8/$\overline{\text{D8}}$ brane system with a number of strings k_r extending in the radial direction of the AdS space from the vertex down to the horizon, called "radial strings", as well as, the remaining number string $k_h = N_{c^-} k_r$ connecting among the D4/D8/$\overline{\text{D8}}$ branes system and the vertex called "hanging strings".

According to holographic duality in the SS model, dynamics of strongly coupled multi-quark in 5 dimensional $SU(N_c)$ gauge theory could be described by the weakly coupled holographic configuration of the multiquark in the type IIA supergravity (superstring theory) defined in 10 dimensions. Therefore, to describe the deconfined matter at finite temperature using the SS model, let's first consider the metric of the 10-Dim spacetime written as

$$ds^2 = \left(\frac{u}{R_{\text{D4}}}\right)^{3/2}\left(f(u)dt^2 + \delta_{ij}dx^i dx^j + dx_4{}^2\right) + \left(\frac{R_{\text{D4}}}{u}\right)^{3/2}\left(u^2 d\Omega_4^2 + \frac{du^2}{f(u)}\right). \tag{3.8}$$

Given that the dilaton field, the 4-form field strength, and the radius of curvature of the spacetime configuration are

$$e^\phi = g_s\left(\frac{u}{R_{\text{D4}}}\right)^{3/4}, \qquad F_{(4)} = \frac{2\pi N}{V_4}\epsilon_4, \qquad R_{\text{D4}}^3 \equiv \pi g_s N l_s^3,$$

respectively, while

$$f(u) \equiv 1 - u_T^3/u^3, \qquad u_T = 16\pi^2 R_{\text{D4}}^3 T^2/9.$$

The configuration is compactified with a periodicity $2\pi R$ transversely to the D8/$\overline{\text{D8}}$ branes in x_4 direction. The volume of the unit 4-sphere Ω_4 is represented by V_4 while ϵ_4 is a volume of the 4-form. Additionally, l_s is the string length, $F_{(4)}$ is the 4-form field strength, and g_s is the string coupling.

Holographically, the dynamics of the configuration could be described by the Dirac-Born-Infeld or DBI action of D8/$\overline{\text{D8}}$ written as

$$S_{\text{D8}} = -\mu_8 \int d^9 X e^{-\phi} Tr\sqrt{-\det(g_{MN} + 2\pi\alpha' F_{MN})} \tag{3.9}$$

where F_{MN} is the component of field strength of the $U(N_f)$ flavour group on the brane system given by

$$F = d\mathcal{A} + i\mathcal{A} \wedge \mathcal{A}. \tag{3.10}$$

The gauge field $\mathcal{A}$ with $U(N_f)$ symmetry could be decomposed into $SU(N_f)$ represented by A and $U(1)$ part denoted by $\hat{A}$:

$$\mathcal{A} = A + \frac{1}{\sqrt{2N_f}}\hat{A}. \tag{3.11}$$

Note that only the diagonal part of $U(N_f)$ remain the same. Finally, the metric g_{MN} is induced on the D8-branes world volume.

The total action of the holographic multiquark phase is given by

$$S = S_{\text{D8}} + S_{\text{D4}} + \tilde{S}_{\text{F1}}, \tag{3.12}$$

where $S_{\text{D8}}, S_{\text{D4}}$ is the DBI action of the connected D8-branes, that of the D4-brane wrapped on S^4, respectively and the action of k_r radial strings stretching from the baryon vertex to the horizon is denoted by $\tilde{S}_{\text{F1}}$.

To describe the U(1) gauge field defined on the D8/$\overline{\text{D8}}$-brane, let's consider the action of the connected D8-branes

$$S_{\text{D8}} \quad = \quad \mathcal{N} \int_{u_c}^{\infty} du \; u^4 \sqrt{f(u)(x_4'(u))^2 + u^{-3}(1 - (\hat{a}_0'(u))^2)}, \tag{3.13}$$

where $\mathcal{N} = (\mu_8 \tau N_f \Omega_4 V_3 R^5)/g_s$, and $U(1)$ diagonal field is rescaled to $\hat{a} = 2\pi\alpha'\hat{A}/(R\sqrt{2N_f})$. Location of the vertex in the radial direction denoted by u_c is estimated from the balance condition of the D4/ D8-strings configuration (see Appendix A of Ref. [4]), where u_0 is the position that $x_4'(u_0) = 0$ (see on (c) of the Figure 3.5). The action of source term consisting of the D4-branes and strings, $S_{\text{D4}} + \tilde{S}_{\text{F1}}$, are given by

$$S_{\text{source}} \quad = \quad \mathcal{N}n \left[\frac{1}{3}u_c\sqrt{f(u_c)} + n_s(u_c - u_T) \right], \tag{3.14}$$

where n is a number density of multiquark, $n_s = k_r/N_c$ is the ratio of number of radial strings divided by the total number of strings joining the vertex. Holographically, the ratio n_s represents the relative colour charges per a multiquark state.

3.4.2 Thermodynamics of Holographic Multiquark

Consider the $U_B(1)$ symmetry corresponding to the diagonal part of the global flavour symmetry, $U(N_f)$, provided by the N_f flavour branes. Holographically, the baryon chemical potential μ is the conjugate of the $U_B(1)$ charge. Therefore, we could identify μ in the gauge theory side with the zeroth component A_0 of the gauge field at the boundary [75]. Hence,

$$\mu = \hat{a}_0(\infty). \tag{3.15}$$

According to the holographic duality, we could identified the grand canonical potential density with the classical solution of the D8-branes action [76]:

$$\Omega(\mu) = \frac{1}{\mathcal{N}} S_{\mathrm{D8}}[T, x_4'(u), \hat{a}_0(u)]_{\mathrm{classic}}. \tag{3.16}$$

To change the dependency on the variable $\hat{a}_0(u)$ in S_{D8} to the multiquark number density of $U_B(1)$ gauge field, $n(u)$ in $\tilde{S}_{\mathrm{D8}}$, the free energy could be expressed as a combination of the grand potential in Legendre-transformation form and the additional source term in Eq. (3.14). We could determine the baryon chemical potential by evaluating the partial derivative of the free energy density with respect to the number density:

$$\mu = \frac{\partial}{\partial n} \frac{1}{\mathcal{N}} \left(\tilde{S}_{\mathrm{D8}}[T, x_4'(u), n(u)]_{\mathrm{classic}} + S_{\mathrm{source}}(n, u_c) \right) \tag{3.17}$$

where the Legendre-transformed action $\tilde{S}_{\mathrm{D8}}$ is

$$\tilde{S}_{\mathrm{D8}}[T, x_4'(u), n(u)] = S_{\mathrm{D8}}[T, x_4'(u), \hat{a}_0(u)] + \mathcal{N} \int_{u_c}^{\infty} n(u)\hat{a}_0'(u)du \tag{3.18}$$

$$= \int_{u_c}^{\infty} du u^4 \sqrt{f(u)(x_4'(u))^2 + u^{-3}} \sqrt{1 + \frac{n^2(u)}{u^5}}. \tag{3.19}$$

By using the holographic dictionary, baryon number density could be written as

$$n(u) = -\frac{1}{\mathcal{N}} \frac{\delta S_{\mathrm{D8}}}{\delta \hat{a}_0'(u)} = \frac{u\hat{a}_0'(u)}{\sqrt{f(u)(x_4'(u))^2 + u^{-3}(1 - (\hat{a}_0'(u))^2)}} = \mathrm{const.} \tag{3.20}$$

The other constant of the configuration is

$$(x_4'(u))^2 = \frac{1}{u^3 f(u)} \left[\frac{f(u)(u^8 + u^3 d^2)}{F^2(u_c, d, T, n_s)} - 1 \right]^{-1} = \mathrm{const}, \tag{3.21}$$

where $F(u_c, d, T, n_s)$, given by

$$F^2(u_c, n, T, n_s) = u_c^3 f(u_c) \left(u_c^5 + n^2 - \frac{n^2 \eta_c^2}{9 f(u_c)} \right), \tag{3.22}$$

where

$$\eta_c \equiv 1 + \frac{1}{2} \left(\frac{u_T}{u_c} \right)^3 + 3n_s \sqrt{f(u_c)}. \tag{3.23}$$

We could determine the form of $F(u_c, n, T, n_s)$ by considering the force condition at the u_c. For more details see the Appendix of Ref. [4].

Using the description of x_4 in Eq. (3.21), and fixing the constraint for the separation L_0 between D8- and $\overline{\mathrm{D8}}$-branes to $L_0 = 2 \int_{u_c}^{\infty} x_4'(u)du = 1$, we get

$$\mu = \int_{u_c}^{\infty} \hat{a}_0'(u) + \frac{1}{\mathcal{N}} \frac{\partial S_{\mathrm{source}}}{\partial n} \bigg|_{T, L_0, u_c}, \tag{3.24}$$

where the later term represents the contribution from the sources, μ_{source}. For more information on the calculations see Refs. [4, 29]

We could determine the thermodynamic properties of the multiquark from the relations mentioned earlier. According to Ref. [4], we have already investigated that the multiquark state is more preferred over another deconfined nuclear matter in the conjectured phase diagram at any moderate temperature from that above the deconfinement to the chiral symmetry restoration temperature and at the finite quark chemical potential.

3.4.3 Equation of State of Holographic Multiquark

To determine the EoS, we need the chemical potential as well as the grand canonical potential density of the holographic multiquark written as

$$
\begin{aligned}
\mu &= \int_{u_c}^{\infty} du \left[1 - \frac{F^2(u_c, n, T, n_s)}{f(u)(u^8 + u^3 n^2)} \right]^{-\frac{1}{2}} \frac{n}{\sqrt{u^5 + n^2}} \\
&\quad + \frac{1}{3} u_c \sqrt{f(u_c)} + n_s(u_c - u_T).
\end{aligned}
\tag{3.25}
$$

$$
\Omega = \int_{u_c}^{\infty} du \left[1 - \frac{F^2(u_c, n, T, n_s)}{f(u)(u^8 + u^3 n^2)} \right]^{-\frac{1}{2}} \frac{u^5}{\sqrt{u^5 + n^2}},
\tag{3.26}
$$

With grand potential density Ω in Eq. (3.26) and chemical potential μ in Eq. (3.25) of the holographic multiquark, the EoS could be determined from following thermodynamic relations:

$$
dG_{\Omega} = -PdV - SdT - Nd\mu.
\tag{3.27}
$$

Note that we could reduce number of variables in the thermodynamics relation above by considering their volume-density form so that S, N and G_{Ω} are replaced by s, n and Ω, respectively; where

$$
P = -G_{\Omega}/V \equiv -\Omega(T, \mu).
\tag{3.28}
$$

Suppose that the multiquarks are uniformly distributed, the number density of multiquark could be obtained from

$$
n = \frac{\partial P}{\partial \mu}(T, \mu).
\tag{3.29}
$$

By rearranging the relation with the chain rule,

$$
\left. \frac{\partial P}{\partial n} \right|_T = \left. \frac{\partial \mu}{\partial n} \right|_T n,
\tag{3.30}
$$

then we could determine the pressure P from the given the number density n and chemical potential μ as

$$
P(n, T, n_s) = \mu(n, T, n_s)\, n - \int_0^n \mu(n', T, n_s) d(n').
\tag{3.31}
$$

Note that the pressure vanishes when $n = 0$ or no QCD matter presents.

EoS for Low Density Holographic Multiquark

At very low number density n, η_c converges to $\eta_0 + \mathcal{O}(n)$ as

$$\eta_0 \equiv 1 + \frac{1}{2}\left(\frac{u_T}{u_0}\right)^3 + 3n_s\sqrt{f(u_0)}, \tag{3.32}$$

as u_c turns into u_0. From Eq. (3.25), the baryon chemical potential at low n limit can then be approximated to be

$$\mu \simeq \mu_{\text{source}} + \alpha_0 n - \beta_0(n_s)n^3, \tag{3.33}$$

where

$$\mu_{\text{source}} \equiv \frac{1}{3}u_c\sqrt{f(u_c)} + n_s(u_c - u_T),$$

$$\alpha_0 \equiv \int_{u_0}^{\infty} \frac{u^{-5/2}}{1 - \frac{f_0 u_0^8}{f u^8}},$$

$$\beta_0(n_s) \equiv \int_{u_0}^{\infty} \frac{u^{-5/2}}{2\sqrt{1 - \frac{f_0 u_0^8}{f u^8}}} \times \left[\frac{f_0 u_0^3}{f u^8 - f_0 u_0^8}\left(1 - \frac{\eta_0^2}{9f_0} - \frac{u_0^5}{u^5}\right) + \frac{1}{u^5}\right]. \tag{3.34}$$

Replacing the chemical potential in Eq. (3.31) with Eq. (3.33), we could express the pressure at very small n as

$$P(n) \simeq \frac{\alpha_0}{2}n^2 - \frac{3\beta_0(n_s)}{4}n^4. \tag{3.35}$$

EoS for High Density Holographic Multiquark

At very large n and relatively low T, the baryon chemical potential could be expressed as

$$\mu \simeq \mu_{\text{source}} + \frac{n^{2/5}}{5}\frac{\Gamma\left(\frac{1}{5}\right)\Gamma\left(\frac{3}{10}\right)}{\Gamma\left(\frac{1}{2}\right)} + \frac{u_c^3 f_c}{10}\left(1 - \frac{\eta_c^2}{9f_c}\right)n^{-4/5}\frac{\Gamma\left(-\frac{2}{5}\right)\Gamma\left(\frac{19}{10}\right)}{\Gamma\left(\frac{3}{2}\right)} \tag{3.36}$$

where the value of integration u_c^5/n^2 is approximately zero as n becomes very large. Similarly, the pressure could be determined from Eq. (3.31) and Eq. (3.36) as

$$P \simeq \frac{2}{35}\left(\frac{\Gamma\left(\frac{1}{5}\right)\Gamma\left(\frac{3}{10}\right)}{\Gamma\left(\frac{1}{2}\right)}\right)n^{7/5}. \tag{3.37}$$

Note that the energy density ρ in both cases can be found through the relation $d\rho = \mu dn$.

CHAPTER IV

Equation of State (EoS) for Massive Neutron Stars with Holographic Multiquark Cores

In this chapter, we consider the overall picture of EoS for massive neutron stars with the multiquark core. For densities below 10^4 g cm^{-3}, the EoS for nuclear matter in this range could be obtained from Ref. [42]. For densities between 10^4 and 4.3×10^{11} g cm^{-3}, the point of neutron drip, the EoS of the nuclear matter could be determined from calculations based on the effect of Coulomb lattice and nuclear mass extrapolation data from [43]. From densities between 4.3×10^{11} and 1.34×10^{14} g cm^{-3}, the EoS could be determined from the calculations in Ref. [44, 49] based on standard nuclear physics or equivalently effective field theory based on two-nucleon interaction which include the effects of hyperons. For the density ranging from $\rho_s/2 = 75.2$ MeV fm^{-3}(1.34×10^{14}g cm^{-3}) up to $\rho_1 = 1.1\rho_s = 165.3$ MeV fm^{-3}(2.94×10^{14} g cm^{-3}), the EoS could be evaluated from the CET calculations based on chiral two-nucleon (2N) and three-nucleon (3N) interaction based on Ref. [77] where only the long-range two-pion-exchange parts of the 3N interactions contribute. For the densities beyond ρ_1, the further extensions of EoS for the nuclear matter could be determined, following Ref. [45]. However, at high densities, the existence of multiquark states is expected in the core of massive neutron stars. After that, we present the important results from Ref. [78] that the state of matter in the core of massive NS could be multiquark. The EoS for multiquark could be described alternatively by using a specific holographic QCD model called the "Sakai-Sugimoto" (SS) model, following Ref. [5]. Finally, we consider the phase transition between nuclear matter and multiquark matter with beta equilibrium.

4.1 Nuclear Matter EoS from Ultra-Low to Intermediate Density Regime

For simplicity, the EoS for nuclear matter from the ultra-low density to the intermediate density regime would be joined and fitted numerically into connected piecewise polytropes. It could be described as follows:

4.1.1 Nuclear Matter EoS at Ultra-Low Densities

EoS of the ultra-low-density crust could be obtained from Table 7 of Ref. [45] as a combination of EoSs from Refs. [43, 44, 49], it can be numerically fitted from polytropic EoSs below:

$$
\begin{aligned}
P(\rho) &= \kappa_a \rho^{\Gamma_a} + \alpha_a, \text{ for } 0 \le \rho \le \rho_a, \quad \text{(blue)} \\
P(\rho) &= \kappa_b \rho^{\Gamma_b}, \text{ for } \rho_a \le \rho \le \rho_b, \quad \text{(green)} \\
P(\rho) &= \kappa_c \rho^{\Gamma_c}, \text{ for } \rho_b \le \rho \le \rho_c, \quad \text{(orange)} \\
P(\rho) &= \kappa_d \rho^{\Gamma_d}, \text{ for } \rho_c \le \rho \le \rho_d, \quad \text{(red)}
\end{aligned}
$$

$$(4.1)$$

where $(\kappa_a, \Gamma_a, \alpha_a) = (280.00, 2.0000, -6.0000 \times 10^{-21})$ and $(\kappa_b, \Gamma_b) = (2.15247 \times 10^{-3}, 1.22213)$, $(\kappa_c, \Gamma_c) = (9.08176 \times 10^{-4}, 0.622687)$, $(\kappa_d, \Gamma_d) = (3.70286 \times 10^{-4}, 1.61786)$, while $(\rho_a, \rho_b, \rho_c, \rho_d)$ = $(2.66284 \times 10^{-7}, 0.237033, 2.46333, 75.1364)$ given that the density and the pressure are in MeV fm^{-3} unit. The numerically fitted EoS for ultra-low densities could be shown in the Figure 4.1. The colours inside the round brackets behind the Eq. (4.1) are used to indicate each EoSs in different sub-regime for this density range.

4.1.2 Nuclear Matter EoS at Low Densities

At densities between 75.1364 MeV/fm^3 < ρc^2 < 165.3 MeV/fm^3, the EoS could be determined from the Eqs. (2.134) and (2.133) and their values have been expressed in the Table 5 of Ref. [45]. Similarly, the pressure and energy density could also be numerically fitted and written as

$$P(\bar{n})/T_0 = \frac{2}{3} n_0 a_1 \bar{n}^{5/3} + n_0 b_1 \bar{n}^2 + \gamma n_0 c_1 \bar{n}^{\gamma+1}, \quad (4.2)$$

where $\bar{n} = n/n_0$ and

$$\rho(\bar{n}) c^2 / T_0 = a_0 \bar{n}^{5/3} + b_0 \bar{n}^2 + c_0 \bar{n}^{\gamma+1}, \quad (4.3)$$

for $T_0 = 36.84$ MeV and dimensionless parameters $a_0 = 176.209, b_0 = -250.992, c_0 = 100.253$. Due to c_i uncertainties in the low-energy coupling terms in the leading chiral 3N interactions,
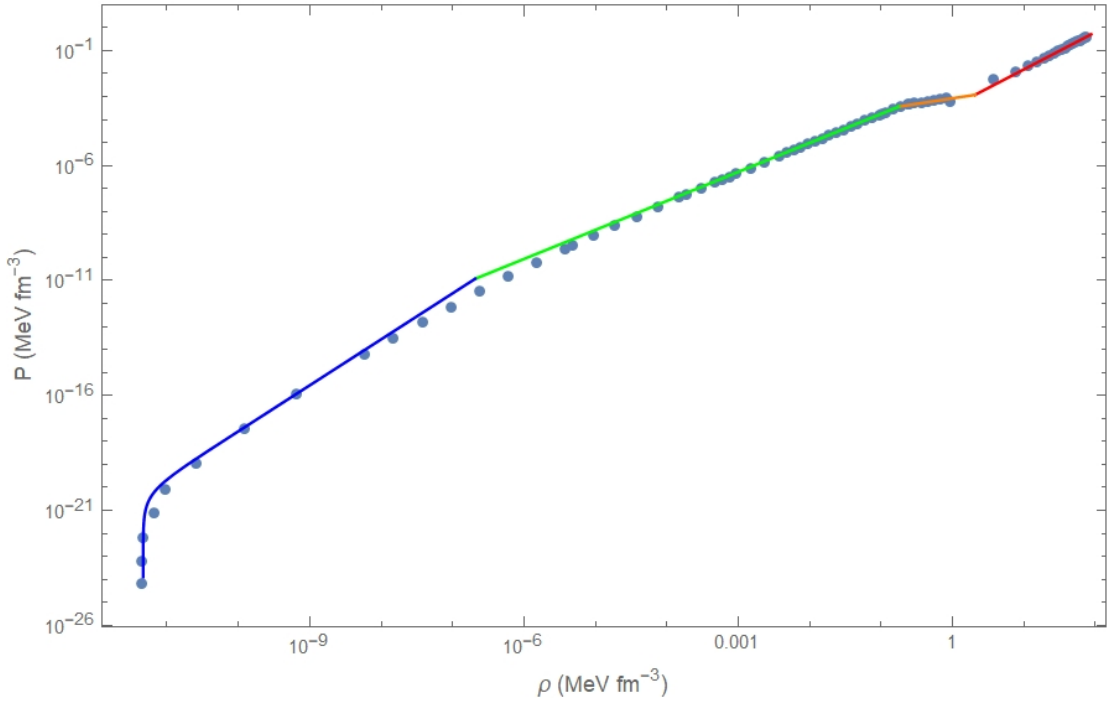
Figure 4.1: Numerical fitting EoS for ultra-low densities nuclear matter, corresponding to Table 7 of Ref. [45] where the pressure P is plotted against the mass density ρ

the EoS spans into a narrow band. Correspondingly, the upper limit and the lower limit of the EoS band could be represented by the dashed blue lines in Figure 4.2 and Figure 4.4) where $(a_1, b_1, c_1) = (1.55468, -2.50096, 1.44835)$ and $(1.33832, -2.0337, 1.07001)$, respectively.

4.1.3 Nuclear Matter EoS at Intermediate Densities

For intermediate density, the general extensions of EoS for CET nuclear matter from Section 2.3 could be expressed empirically as shown in the Figure 4.4. Stiff, intermediate and soft piecewise polytropes at higher densities from Ref. [45], individually with different corresponding powers Γ_1, Γ_2 and Γ_3, can be displayed in the Figure 4.2 and written as follows:

$$
\begin{aligned}
P(\rho) &= \kappa_1 \rho^{\Gamma_1}, \text{ for } \rho_1 \leq \rho \leq \rho_{12}, \\
P(\rho) &= \kappa_2 \rho^{\Gamma_2}, \text{ for } \rho_{12} \leq \rho \leq \rho_{23}, \\
P(\rho) &= \kappa_3 \rho^{\Gamma_3}, \text{ for } \rho_{23} \leq \rho \leq \rho_{max}.
\end{aligned}
$$

$$(4.4)$$

The general extensions of nuclear matter EoS could be expressed in terms of density $\rho \equiv mn$ as follows:

1. the stiff EoS (dashed-red line in Figure 4.2) has the exponents $(\Gamma_1, \Gamma_2, \Gamma_3) = (4.5, 5.5, 3.0)$

where $(\rho_{12}, \rho_{23}, \rho_{max}) = (1.5\rho_s, 2.0\rho_s, 3.3\rho_s)$ and $(\kappa_1, \kappa_2, \kappa_3) = (11.6687, 51.7666, 2.56345)$,

2. the intermediate EoS (dashed-orange line in Figure 4.2) has the exponents $(\Gamma_1, \Gamma_2, \Gamma_3) = (4.0, 3.0, 2.5)$ where $(\rho_{12}, \rho_{23}, \rho_{max}) = (3.0\rho_s, 4.5\rho_s, 5.4\rho_s)$ and $(\kappa_1, \kappa_2, \kappa_3) = (2.89711, 1.30607, 1.07402)$, and

3. the soft EoS (dashed-green line in Figure 4.2) has the exponents $(\Gamma_1, \Gamma_2, \Gamma_3) = (1.5, 6.0, 3.0)$ where $(\rho_{12}, \rho_{23}, \rho_{max}) = (2.5\rho_s, 4.0\rho_s, 7.0\rho_s)$ and $(\kappa_1, \kappa_2, \kappa_3) = (0.0321845, 2.63607, 0.572502)$,

where the density and pressure are also in GeV fm^{-3} unit, given that the saturation density is $\rho_s = 0.150273$ GeVfm^{-3}.
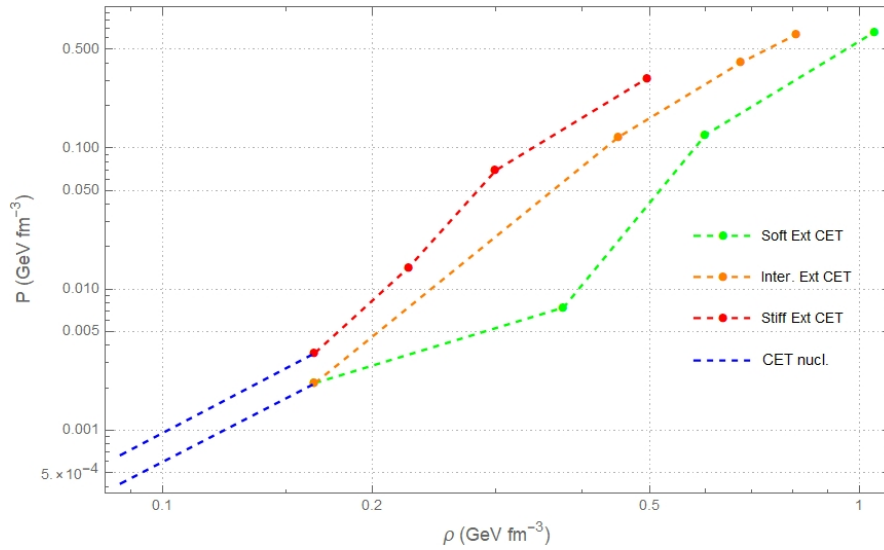

Figure 4.2: EoS for massive neutron stars consisting of EoS for Extended CET Nuclear and CET matter where the pressure P is plotted against the mass density ρ

4.2 EoS of Multiquark Matter at High Densities

Now let's consider multiquark matter using the holographic model. According to our former work on the thermodynamics of holographic multiquark [5], we obtained EoS of the multiquark state as shown in Figure 4.3. The log P v.s. log n graph could be used to evaluate the EoS of the multiquark where n is a number density of multiquark relating to density $\rho(n)$. The EoS of the multiquark matter could be described holographically and then approximated in two different limits. At high density, pressure is insensitive to relative colour charge per multiquark n_s; however, at low density, the pressure slightly decreases as n_s increases.
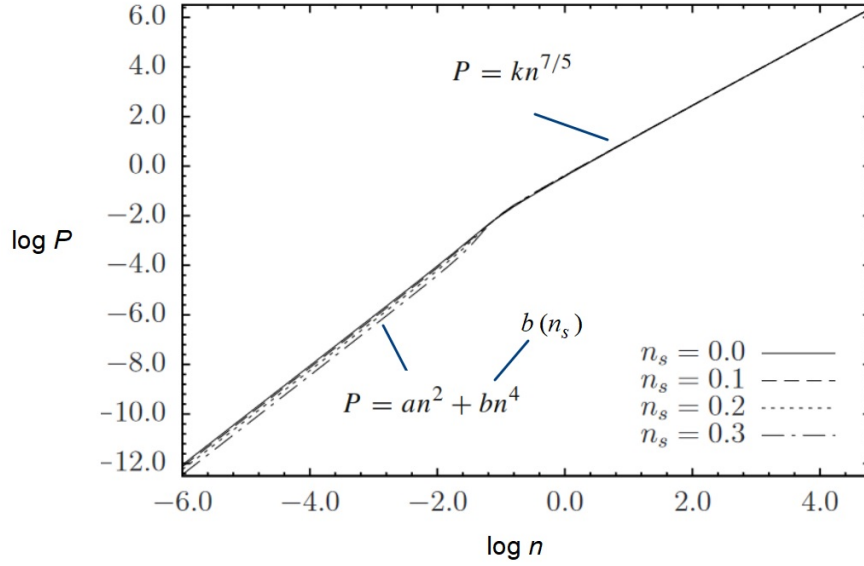
Figure 4.3: Pressure P of the multiquark matter vs. multiquark number density n: image adapted from Ref. [5].

4.2.1 EoS of Low Density Multiquark (mql) at High Densities

As reported by Ref. [5], the EoS of mql matter in dimensionless unit can be summarized as follows: at small number density of multiquark n,

$$P(n) = an^2 + bn^4, \tag{4.5}$$

$$\mu(n) = \mu_0 + an + \frac{4}{3}bn^3, \tag{4.6}$$

$$\rho(n) = \mu_0 n + an^2 + \frac{b}{3}n^4, \tag{4.7}$$

where $\mu_0 = \mu(n_{mq} = 0)$ is the initial value of the multiquark chemical potential defined as its number density approaches zero. For $n_s = 0$, $a = 1, b = 0, \mu_0 = 0.17495$ while for $n_s = 0.3$, $a = 0.375, b = 180.0, \mu_0 = 0.32767$. Note that to estimate $\mu(n)$ and $\rho(n)$, we use the thermodynamics relation,

$$\mu(n) = \int_0^\eta \frac{1}{\eta} \frac{\partial P(n)}{\partial \eta} d\eta + \mu_0, \tag{4.8}$$

$$\rho(n) = \int_0^\eta \mu(\eta) d\eta + \rho_0, \tag{4.9}$$

for the given pressure $P(n)$.

4.2.2 EoS of High Density Multiquark (mqh) at High Densities

At large n, the EoS for mqh matter takes the following form

$$P(n) = kn^{7/5}, \tag{4.10}$$

$$\mu(n) = \mu_c + \frac{7}{2}kn^{2/5}, \tag{4.11}$$

$$\rho(n) = \mu_c n + \frac{5}{2}n^{7/5}, \tag{4.12}$$

where the transition between high and low density multiquark could be indicated by the critical number density n_c together with their chemical potential $\mu(n_c) = \mu_c$ at the critical density. For $n_s = 0 : n_c = 0.215443, \mu_c = 0.564374$, while for $n_s = 0.3 : n_c = 0.086666, \mu_c = 0.490069$, where for both cases $k = 10^{-0.4}$.
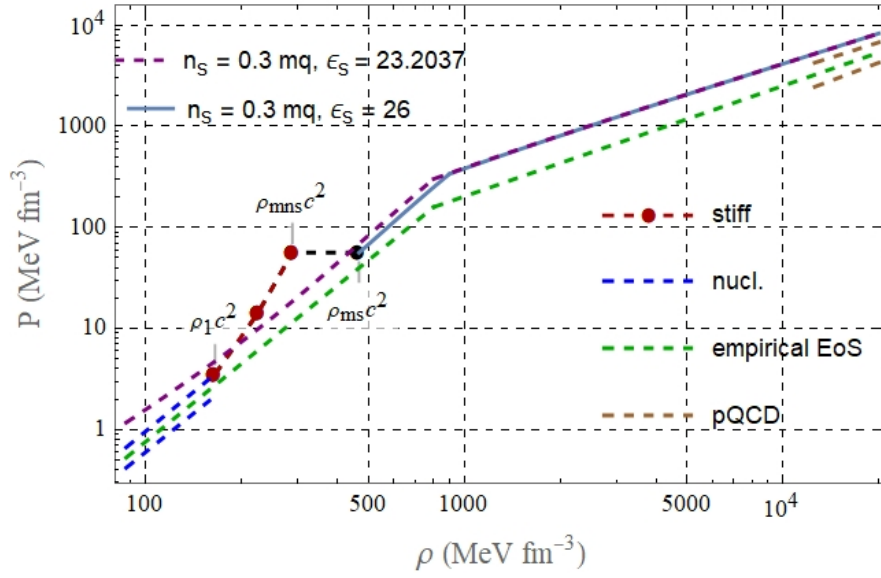

Figure 4.4: EoS for massive neutron stars consisting of EoS for mqh, mql, Stiff Extended CET nuclear matter, CET nuclear matter and standard nuclear matter as density decreases from high (multiquark cores) to low (nuclear matter crusts)

4.3 Phase Transitions between Deconfined Multiquark Matter and Confined Nuclear Matter

In this section, we consider phase transitions between the extended nuclear matter and the multiquark matter. For thermodynamic consistency, we consider the transitions through the relation between pressure and multiquark chemical potential per quark or $P - \mu_q$ diagram of the extended-CET-nuclear matter and that of the multiquark matter as shown in the Figure 4.5. Note that the empirical extension of EoSs leaves incomplete description on the field theory side, therefore we exclude ourselves from the explanation on the phase transition using complete knowledge of CET.

According to Ref. [4, 5], at extremely high pressure and density, baryons get compressed

against one another tightly at a low temperature ($T << 10^{12}$ K, below the confinement temperature), that quarks within hadron start dripping freely among the baryons. Strong interaction between quarks, described by exchanging colour charges between gluons, is still nonperturbative. Correspondingly, the baryonic matter may turn into multiquark nuclear matter, with the many quarks forming bound states through the remaining strong interaction in the deconfined vacuum. To consider the phase transition, we compare the free energy by assuming that the onset value of quark chemical potential for baryonic matter is the same as that of the multiquark phase, following Ref. [79];
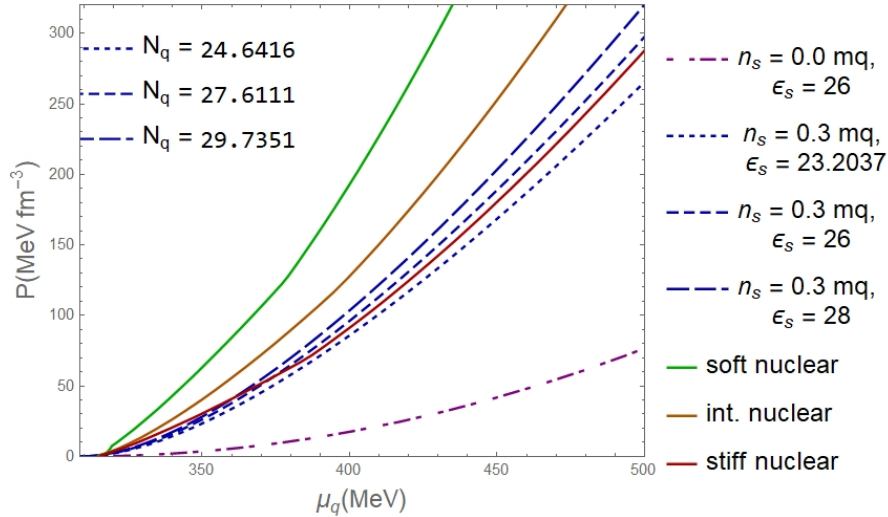

Figure 4.5: Comparison on the pressure P vs. the quark chemical potential μ_q between Extended CET nuclear matter and that of multiquark matter

$$\mu_{mq,0} = \frac{\mu_{b,0}}{3} N_q = \mu_{q,0} N_q, \qquad (4.13)$$

where the number of quarks per multiquark is N_q, and the initial value of the quark chemical potential is $\mu_{q,0}$. Following the Ref. [79], we set $\mu_{q,0} = 308.55$ MeV, concerning the nuclear EoS. Note that fixing $\mu_{mq,0}$ in the SS model also results in setting the energy density scale ϵ_s, allowing N_q to be determined later. Due to a jump in density at the transition between the multiquark and nuclear matter phase, it is assumed to be first order.

As illustrated in Figure 4.5, the $P - \mu_q$ diagram could be used to determine the transition point. Given that both states have the same pressure, the thermodynamically preferred phase will have lower quark chemical potentials. For $n_s = 0, 0.3$, there are possible three options for phase transitions between multiquark and the extended CET nuclear matter depending on the energy density scale $\epsilon_s = 23.2037, 26, 28$ GeV fm^{-3}. Thermodynamically, we found that the colourless multiquark represented by $n_s = 0$ is always less preferred than the nuclear matter. We choose ϵ_s within the minimal range of values that result in the NS masses restricted by recent

observations. Additionally, ϵ_s are set to achieve nice interpolations from the nuclear matter EoS from CET at low densities to free quark EoS from pQCD at high densities. This will be discussed in the next section.

The $P - \mu_q$ diagram for multiquark starts crossing the stiff CET EoS for nuclear matter when setting between $\epsilon_s \geq 26$ GeV fm^{-3}. Beyond $\mu_q = 374.0$ MeV, the multiquark state is more preferred over the stiff nuclear matter with $\epsilon_s = 26$ GeV fm^{-3}, $n_s = 0.3$. For $\epsilon_s = 26 - 28$ GeV fm^{-3}, the number of quark N per multiquark could reach $\simeq 25 - 30$ (around $8 - 10$ baryons) in the the core of massive NS.

As shown in Figure 4.5, the colourless multiquark phase ($n_s = 0$) is always less preferred thermodynamically than all of the extended nuclear EoS. However, the extended CET EoSs are just empirical. Therefore, we exclude the possibility of the colourless multiquark from our consideration. Interestingly, the $n_s = 0.3$ multiquark EoS is similar to the stiff nuclear matter EoS. This demonstrates that the stiff CET nuclear EoS at high densities is a good extension (the multiquark and stiff EoS overlap almost completely for $\epsilon_s \simeq 25$ GeV fm^{-3}). Given that thermodynamically, the multiquark state is less preferred than moderate and soft nuclear EoS, we shall restrict our analyses at most for the NS with multiquark core and the extremely strong nuclear crust from now on.

For any ancient NS, the temperature inside becomes very low compared to the confinement temperature as the NS has been cooled down by the direct Urca processes and eventually reaches thermal equilibrium with a beta stability condition. Correspondingly, the baryon chemical potential and neutrino emission would be suppressed as the beta stability and charge neutrality keep going on. Consider the beta equilibrium

$$
\begin{aligned}
n &\rightarrow p + e + \bar{\nu}_e, \\
p + e &\rightarrow n + \nu_e,
\end{aligned}
\tag{4.14}
$$

which results in

$$
\mu_n = \mu_p + \mu_e.
\tag{4.15}
$$

The electrons and protons are restricted inside the star due to strong gravitational attraction, which can be described as degenerate Fermi gases. As the number of protons and electrons grows, the Fermi energies also increase and vice versa. Eventually, the number of n, p and e become constants when

$$
E_{F,n} = E_{F,p} + E_{F,e},
\tag{4.16}
$$

where the Fermi energy of fermion $i = n, p, e$ is denoted by $E_{F,i} \simeq \mu_i$. Since low to moderate temperatures, $E_{F,i} \simeq n_i^{2/3}/m_i$, then the contribution from Eq. (4.16) dominates. Therefore, the

numbers of protons and electrons, $n_p = n_e$, are much less than that of the neutrons. As nuclear matter turns into the multiquark state with the beta equilibrium condition, it requires that

$$E_{F,mq} = E_{F,mq'} + E_{F,e}, \tag{4.17}$$

where $E_{F,mq}, E_{F,mq'}$ represent the Fermi energy of the multiquark before and after beta decay, respectively. As written in Eq. (4.16), the charge neutrality requires $n_{mq'} = n_e$. Since multiquarks are around 8-10 times more massive than baryons, meanwhile the number density is reduced by the same factor, i.e., $m_{mq} = f m_b, n_{mq} = n_b/f$, for $f \simeq 8 - 10$, then $E_{F,mq} = f^{-5/3} E_{F,b}$, which is about 2-3% of $E_{F,b}$. To satisfy Eq. (4.17), the Fermi energy of the electron must be reduced even further at beta equilibrium. As a result, the number of electrons and electrically charged multiquarks becomes much lower after stiff nuclear matter turn into multiquark. Nevertheless, when considering the beta equilibrium, the existence of the multiquark is relatively common due to the electron suppression.

4.4 Matching between the EoS for the Holographic Multi-quark and that for the Extended Nuclear Matter

The crucial results in Figure 1 and Figure 2 of the Ref. [1] imply that the interpolation between two different EoSs, the free quark EoS at high density described by pQCD and nuclear matter EoS at low density provided by CET could be achieved by connected EoS roughly with two different power laws. According to our previous work on the multiquark states based on the holographic SS model [5], it was found that the multiquark phase dominates at high density and low temperature. As illustrated in Figure 4.4, a reasonable interpolating EoS of $n_s = 0.3$ multiquark matter can be obtained by tuning $\epsilon_s = 23.2037$ GeV fm^{-3}. This results in a transition density $\rho_c = 0.8028$ GeV fm^{-3} as suggested by a joint between the average empirical EoS represented by the green dashed line connecting the extension of pQCD EoS and that of CET nuclear matter EoS together. Although the interpolation caused by the EoS looks nicely, it is not thermodynamically preferable over the extended CET nuclear states. Setting $\epsilon_s = 26$ GeV fm^{-3}, not only the multiquark state is thermodynamically preferable to the stiff nuclear matter but also provides a decent interpolation between high and low density, as seen in Figure 4.4.

CHAPTER V

Modeling Neutron Stars

This chapter demonstrates how to model the structure of massive NS by implementing the hybrid EoS of the NS with holographic multiquark (MQ) core defined in Chapter 4 into Tolman–Oppenheimer–Volkoff (TOV) equation. The NS was assumed to be spherically symmetric, static and in gravitational balance. Solving TOV equation, we could study the structure inside NS by determining how pressure $P(r)$ changes with radius r, how the pressure's gradient relates to density $\rho(r)$ and how much mass was accumulated from the centre $m(r)$. Then, we present the results from Ref. [78] that consider *MR* diagram of massive NSs with holographic MQ cores associated with $n_s = 0.3, \epsilon_s = 26(28)$ GeV fm^{-3} compared to pure MQ stars with $n_s = 0.3, \epsilon_s = 23.2037(26)$ GeV fm^{-3}. Lastly, we consider how the proton-baryon ratio and temperature affect the *MR* diagram.

5.1 Tolman–Oppenheimer–Volkoff (TOV) Equation

This section consider how could we model any static, spherically symmetric star containing a perfect fluid. Generally, metric components for the star are given by:

$$ds^2 = g_{\mu\nu}dx^\mu dx^\nu = e^{\nu(r)}dt^2 - e^{\lambda(r)}dr^2 - r^2 d\theta^2 - r^2\sin^2\theta d\phi^2 \tag{5.1}$$

where the metric above is written in geometrical unit that $G = c = 1$. In a comoving frame, components of stress-energy tensor of the fluid are

$$T_t^t = \rho(r) \text{ and } T_r^r = T_\theta^\theta = T_\phi^\phi = -P(r) \tag{5.2}$$

where $\rho(r)$ and $P(r)$ are density and pressure of the fluid meanwhile the four velocity of the perfect fluid could be normalized by $u_\mu u^\mu = 1$. Consider Einstein's field equation,

$$8\pi T_{\mu\nu} = G_{\mu\nu}. \tag{5.3}$$

The G_{tt} component of Einstein's field equation is

$$8\pi\rho(r)e^{\nu(r)} = \frac{e^{\nu(r)}}{r^2}\left(1 - \frac{d}{dr}\left(re^{-\lambda(r)}\right)\right). \tag{5.4}$$

Integrating (5.4) from 0 to r, we have

$$e^{-\lambda(r)} = 1 - \frac{2m(r)}{r} \tag{5.5}$$

given that $m(r)$ is an accumulated mass from its center to the radius r, where it satisfies $m(0) = 0$ corresponding to $\lambda(0) = 0$ and

$$\frac{dm(r)}{dr} = 4\pi r^2 \rho(r). \tag{5.6}$$

Also, the G_{rr} component of Einstein's field equation could be expressed as

$$8\pi P(r)e^{\lambda(r)} = \frac{1 - e^{\lambda(r)} + r\nu'(r)}{r^2} \tag{5.7}$$

which can be simplified further by using (5.5)

$$\begin{aligned}
\frac{d\nu(r)}{dr} &= \frac{1}{r}\left(1 - \frac{2m(r)}{r}\right)^{-1}\left(\frac{2m(r)}{r} + 8\pi r^2 P(r)\right), \\
\frac{d\nu(r)}{dr} &= 2\frac{m(r) + 4\pi r^3 P(r)}{r(r - 2m(r))}.
\end{aligned} \tag{5.8}$$

We could obtain TOV equation from the conservation in radial direction $\nabla_\mu T_r^\mu = 0$, written as

$$\begin{aligned}
0 &= -\frac{dP(r)}{dr} - \frac{1}{2}(P(r) + \rho(r))\frac{d\nu(r)}{dr}, \\
\frac{dP(r)}{dr} &= -\left(\frac{4\pi r^3 P(r) + m(r)}{r(r - 2)}\right)(P(r) + \rho(r)) \tag{5.9}
\end{aligned}$$

where we have used Eq. (5.8) to rearrange the TOV equation into an expression in Eq. (5.9). After replacing $\lambda(r)$ by using Eq. (5.5), the TOV equation becomes $m(r)$ dependent. Therefore, to solve Eq. (5.9), we need to consider the initial value $m(0) = 0$, instead of $\lambda(0) = 0$.

The total mass M and the stellar radius R are defined where the density and pressure vanish. Note that the initial value $\nu(0) \equiv \nu_0$ has not been specified by Eq. (5.8) since it is written in term of $\nu'(r)$. Therefore the initial value ν_0 could not be arbitrarily set to 0. However, it must be chosen in such a way that the associated boundary requirements at the surface $r = R$ are satisfied. Therefore,

$$e^{\nu(R)} = 1 - \frac{2M}{R}. \tag{5.10}$$

Originally, Tolman (1934, [6]) and Oppenheimer-Volkoff (1939, [7]) used the EoS of degenerate Fermi gas for a state of matter inside NS. It turns out that their upper limit of NS is $\sim 0.7\ M_\odot$ which is not realistic for NS. Therefore, this limit is not correct.

5.2 MR Diagram of NS with Holographic Multiquark Core

In this section, we apply the multiquark EoS given in Eqs. (4.7) and (4.9) for high density region. The further from the centre, the less pressure and density of the multiquark matter.

Below the multiquark-CET nuclear transition point, the stiff CET nuclear matter must be taken into account. After that, we use the recently developed piecewise-polytrope EoS (4.4) from the numerical fitting. Next, for lower densities, we use EoS from (4.2), (4.3), and (4.1) for nuclear matter by the corresponding order of density. From Figure 4.4, there are 3 possibilities for the overall EoSs:

(i) $n_s = 0.3, \epsilon_s = 26$ (28) GeV fm^{-3} multiquark then turning into stiff-nuclear matter at $\rho_{ms(2)}c^2 = 0.4678$ (0.4389) GeV fm^{-3} and $\rho_{mns(2)}c^2 = 0.2891$ (0.2734) GeV fm^{-3};

(ii) pure $n_s = 0.3$ at $\epsilon_s = 23.2037$ GeV fm^{-3} multiquark state for a whole star;

(iii) pure$n_s = 0.3$ at $\epsilon_s = 26$ GeV fm^{-3} multiquark state for a whole star.

The results of the three scenarios on mass-radius relations are shown in Figure 5.1. The The final two cases are the hypothesized multiquark star without any nuclear matter shell. Their existence is feasible given that the temperature at the core is high enough so that the temperature at the surface is also greater than the phase transition temperature between nuclear matter and the multiquark. Solving the TOV equation numerically, any NS consisting of multiquark core and nuclear matter crust described by stiff CET EoS has the mass range around $1.7 - 2.2 M \odot$ and radii of $14.5 - 11.1$ km for $\epsilon_s = 26 - 28$ GeV fm^{-3}, represented by the plains red-black curve in the MR diagram in Figure 5.1.In contrast, the possible observational masses of NSs provided by one-sigma uncertainties [3, 12, 80, 81] are also depicted in Figure 5.1. In Figure 5.2, the *core* of massive NS containing $n_s = 0.3$ multiquark has radius and mass of 8.3 (8.4) km and 1.49 (1.60)$M_\odot$ provided that $\epsilon_s = 26$ (28) GeV fm^{-3}, respectively. The mass and radius of the core in the pure multiquark star case correspond to the entire star where both high- and low-density layers of the multiquark matter could be determined by Eqs. (4.9) and (4.7).

The central temperature must be high enough for the state matter at the centre of NS or the whole star to be in the multiquark state. As the state of matter turns into quark-gluon plasma at the saturation density around n_0, the deconfinement temperature could be roughly estimated from the Hagedorn temperature which is around 150 MeV or 1.7×10^{12} K discovered in the Heavy-Ion collisions at BNL RHIC [82] and CERN ALICE [83]. Interestingly, many theoretical models along with the SS model predict that, at higher densities, the QCD deconfinement from nuclear matter to multiquark states with the broken chiral symmetry could occur at lower temperatures [4, 29]. Additionally, at high density and low temperature, the existence of colour-superconductive diquarks in the model [84] and other multiquark [85] might be possible. The conjecture phase diagram of Ref. [4] demonstrates that for intermediate temperature ($T <$

10^{12} K) and a considerable amount of μ, the deconfined vacuum in the holographic multiquark model is thermodynamically preferred over nuclear vacuum at the low-temperature beyond the deconfinement. Furthermore, the multiquark phase is thermodynamically favoured over the stiff nuclear matter when the quark chemical potential is large enough, according to Section 4.3.

The chemical potential may be used to determine the temperature profile inside the NS (see e.g. Ref. [86]).

$$\frac{T(r)}{T_0} = \frac{\mu(r)}{\mu_0}, \tag{5.11}$$

where $\mu_0 = (\rho_0 + P_0)/n_0, T_0$ are the chemical potential and temperature at the saturation density correspondingly. Additionally, the chemical potential is also useful to determine the confinement/deconfinement temperature associated with the transition between the nuclear matter and multiquark.From Ref. [45], the Fermi energy for CET nuclear EoS is 36.84 MeV. This implies that the nuclear EoS is unresponsive to temperature for the scale far lower than 1 MeV (roughly 5% rise in pressure for $T = 1$ MeV from the zero temperature scenario, estimated from Figure 25 of Ref. [87]). At low temperature, The CET may thus be employed to estimate the chemical potential at the transition with a smaller than 1% error for $T < 0.1$ MeV. The transition parameters for the NS at M_{max} with $n_s = 0.3, \epsilon_s = 26$ GeV fm^{-3} multiquark along with stiff nuclear matter shell are $T_{\text{dec}} = 0.6741$ T_0 and $\mu_{\text{dec}} = 374.0$ MeV , correspondingly, using (5.11). While the transition between the multiquark and FYSS nuclear matter (for more info. see Section 5.2.1) could exist around $\mu_{\text{dec}} = 341 - 342$ MeV and $T_{\text{dec}} \simeq 0.56$ T_0, as seen in Table 5.1.The surface temperature of the massive NS with multiquark core and the CET (FYSS) nuclear crust could be around $T_{\text{surf}} = 0.5643$ (0.546-0.549) T_0. Additionally, the core temperature of the NS with the CET (FYSS) nuclear matter crust that its surface temperature is around 10^9 K, would be roughly 1.77 $(1.82 - 1.83) \times 10^9$ K.

EoS for high- and low-density multiquark could be described roughly by two power laws. In Ref. [5], the multiquark matter is referred to as the multiquark core and crust; however, in our study, we refer to them as "mqh, mql," to prevent confusion. As demonstrated in Figure 5.5, each state of matter has distinct sound speed c_s and adiabatic indicesγ. Surprisingly, for the multiquark at high (low) density, $\gamma \approx 1$ (2.5), respectively, whereas at high density and most of the low density, the squared sound speed $c_s^2 > 1/3$ violates the conformal bound. Additionally, the squared sound speed of the $n_s = 0.3$ multiquark state at high density $c_s^2 \simeq 0.426$ is slightly over the conformal limit described by the state of free quarks with zero mass. At low densities, the adiabatic index γ of multiquark (mql) has $\gamma \approx 2.5$; where its character resembles the hadronic nuclear matter, that is colour-charged and deconfined. However, at high densities, the adiabatic index of multiquark (mqh) is very close to 1 (the conformal bound of free quarks). In comparison, at high densities, the colourless multiquark ($n_s = 0$) has $c_s^2 \lesssim 0.55$ and $\gamma \simeq 1.5$.

Table 5.1 summarise the maximum mass, stellar radius, central density, and transition

density corresponding to each variant of NSs with multiquark cores.

Matter content inside the star	M_{max} $(M_\odot)$	$R_{M_{max}}$ (km)	$\rho_0 c^2$ (GeV/fm^3)	$\rho_c c^2$ (GeV/fm^3)	$\rho_{\mathrm{mq\&b}} c^2$ (GeV/fm^3)
mq&stiff $\epsilon_s = 26$	2.226	11.76	1.216	0.8996	$(\rho_{\mathrm{ms}}c^2)$ 0.4678 $(\rho_{\mathrm{mns}}c^2)$ 0.2891 $\mu_{\mathrm{dec}}(\mathrm{GeV})$ 0.3740
mq&stiff $\epsilon_s = 28$	2.098	11.07	1.403	0.9688	$(\rho_{\mathrm{ms2}}c^2)$ 0.4389 $(\rho_{\mathrm{mns2}}c^2)$ 0.2734 $\mu_{\mathrm{dec}}(\mathrm{GeV})$ 0.3605
mq&FYSS, $i_Y = 1\%$ $\epsilon_s = 23.2037$	2.235	11.31	1.246	0.8028	$(\rho_{\mathrm{ms3}}c^2)$ 0.1246 $(\rho_{\mathrm{mns3}}c^2)$ 0.1111 $\mu_{\mathrm{dec}}(\mathrm{GeV})$ 0.3408
mq&FYSS, $i_Y = 10\%$ $\epsilon_s = 23.2037$	2.234	11.12	1.246	0.8028	$(\rho_{\mathrm{ms4}}c^2)$ 0.1380 $(\rho_{\mathrm{mns4}}c^2)$ 0.1434 $\mu_{\mathrm{dec}}(\mathrm{GeV})$ 0.3424
pure mq $\epsilon_s = 26$	2.111	10.66	1.396	0.8996	-
pure mq $\epsilon_s = 23.2067$	2.235	11.29	1.246	0.8028	-

Table 5.1: Important parameters, at maximum masses, of massive NSs with $n_s = 0.3$ and $\epsilon_s = 26, 28$ GeV fm^{-3} multiquark core and stiff nuclear matter crust; that of massive NSs with with $n_s = 0.3$ and $\epsilon_s = 23.2037$ GeV fm^{-3} multiquark cores and FYSS nuclear matter crust; as well as that of pure $n_s = 0.3$ multiquark stars: with $\epsilon_s = 26$ GeV fm^{-3} and with $\epsilon_s = 23.2037$ GeV fm^{-3}, respectively

5.2.1 Nuclear Matter at Finite Temperature and the Effect of the Proton Fraction Ratio

This section explores the impacts of temperature and proton fraction on the MR diagram. We made assumptions that the heat transfer by releasing neutrino is eventually over, and the change in entropy becomes insignificant (for general analysis of protoneutron stars with the change in entropy see e.g. Refs. [88, 89]). We consider the nuclear matter crust at a finite temperature described by FYSS EoS from Refs. [39, 40, 41], where the state of matter may consist of alpha particles, nuclei of deuterium and that of tritium. This EoS is suitable for describing the nuclear matter of the collapsing core during the supernova. It could be derived from the relativistic mean field theory with a typical set of parameters under statistical equilibrium and is available within the range $T = 0.1 - 398$ MeV. On the other hand, the multiquark EoS is temperature insensitive. Additionally, it is independent of proton to baryon fraction ratio $Y_q \equiv n_p/n_b$ since the distinction between light quarks of different flavours in the multiquark state is ignorable. The $P - \mu_q$ for $n_s = 0.3$ multiquark with $\epsilon_s = 23.2037$ GeV fm^{-3} at various temperature: $T = 0.10, 0.120226$ MeV and different proton to baryon ratio: $Y_q = 0.01, 0.10$ of are plotted in Figure 5.3. Thermodynamically, based on our analysis of the $P - \mu_q$ diagram, the $n_s = 0.3$ multiquark at $\epsilon_s = 26, 28$ GeV fm^{-3} are always favoured over the baryonic matter described by the FYSS EoS.

In Figure 5.4, the effects of temperature and the proton to baryon ratio are illustrated in the MR diagrams of NS with the multiquark core. Note that we only present the *epsilons* = 23.2037 GeV fm−3 with the baryonic matter described by the FYSS EoS as the other possible scenarios at the temperature range contain only *pure* multiquark star. The greater proton to baryon proportion, the smaller radius of NS with the multiquark core.
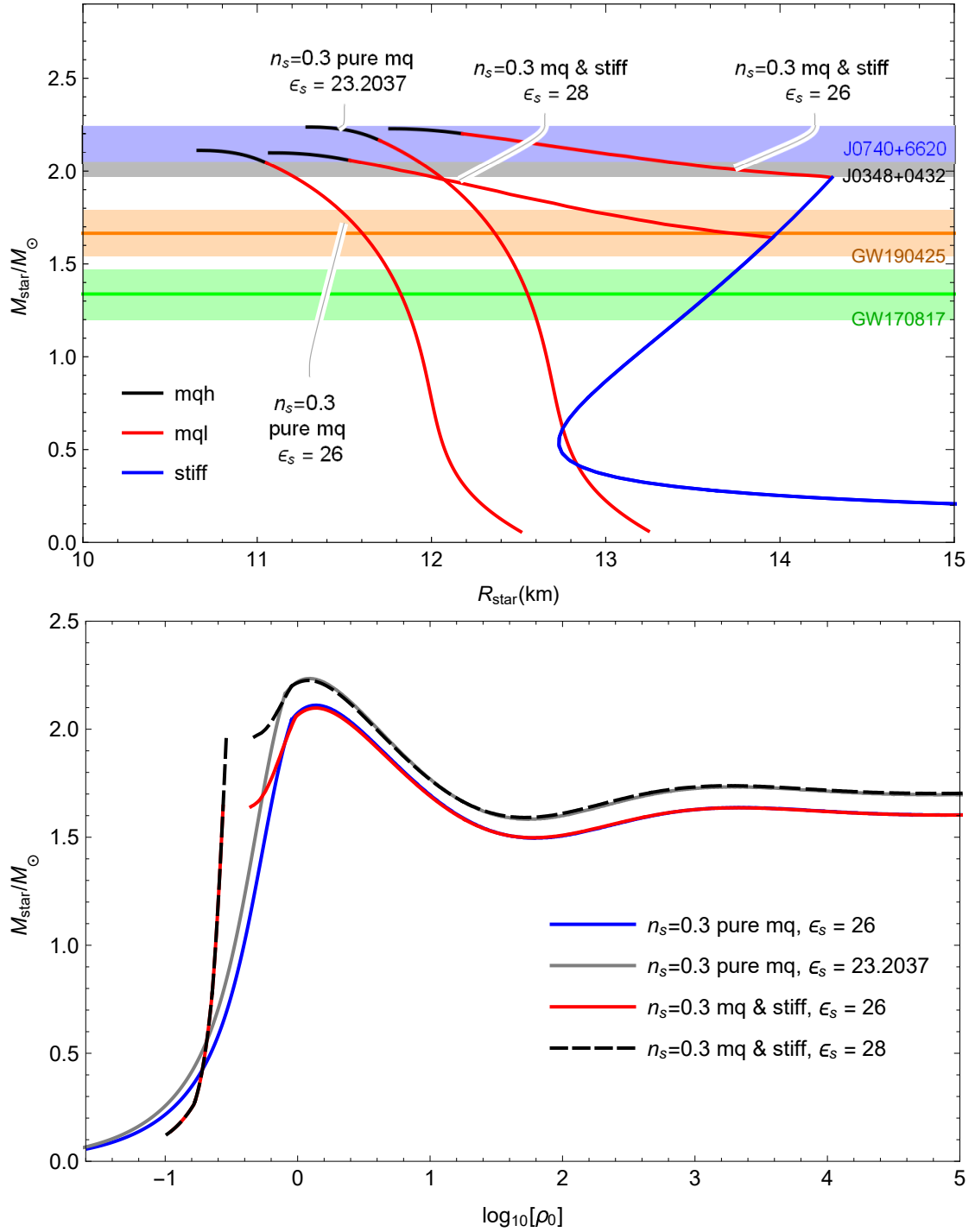
Figure 5.1: *MR* diagram and mass-central density of NS and pure multiquark stars: The different states of nuclear matter inside the star could be labeled by distinct colours. Any point on each curve represents a star with its structure consisting of the following layers ranging from high to low density: multiquark matter, stiff extended CET and the ordinary CET nuclear matter, while the pure multiquark stars consist only of the multiquark. Additionally, the constraints on NSs from observations are also displayed.
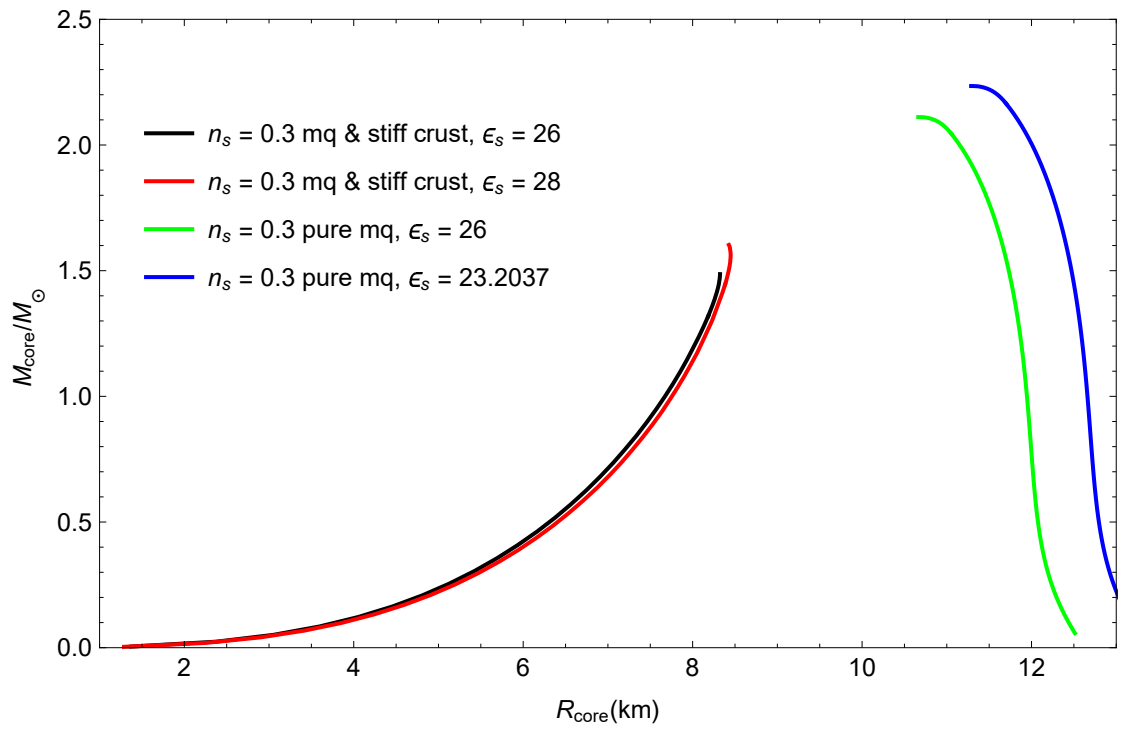
Figure 5.2: *MR* diagram of multiquark cores and that of pure multiquark stars corresponding to the *MR* diagram in Figure 5.1
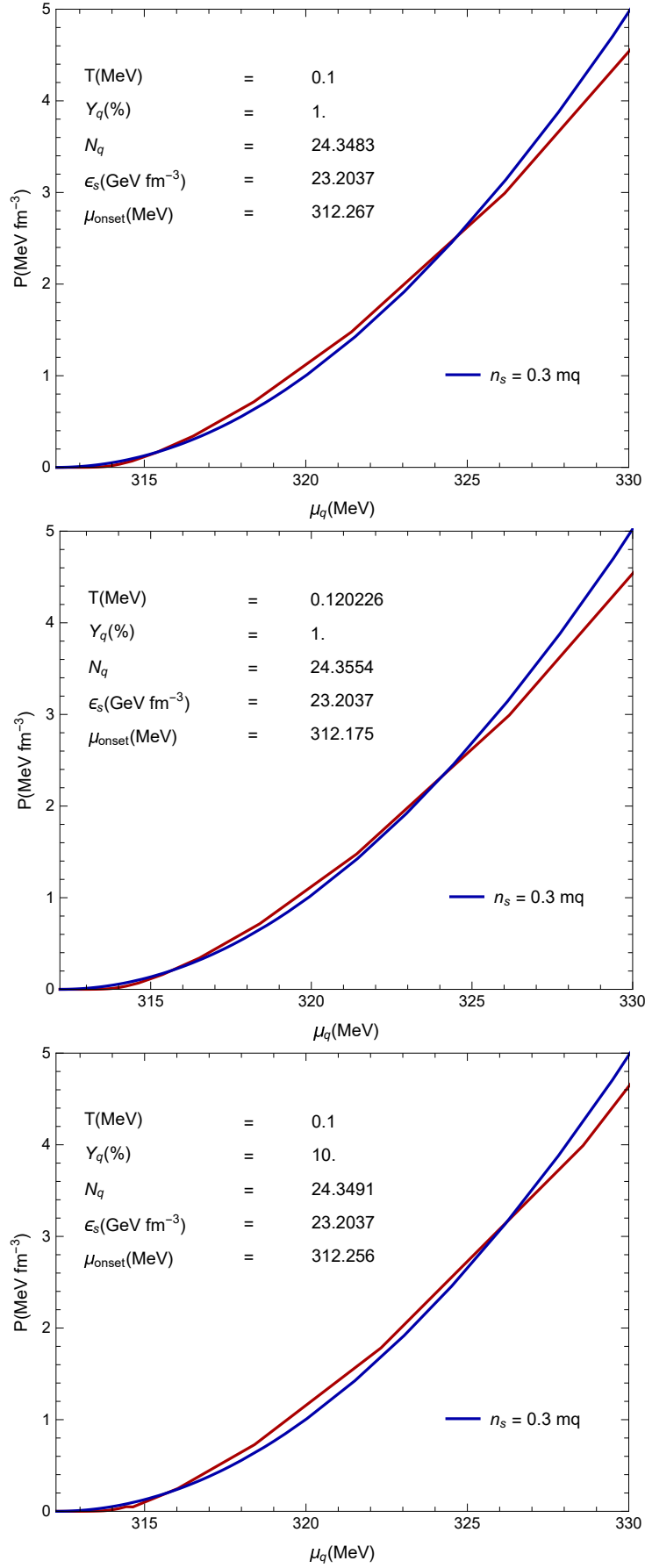
Figure 5.3: A comparison of $P - \mu_q$ plots between the multiquark and baryonic nuclear matter at intermediate temperatures and finite proton to baryon fractions
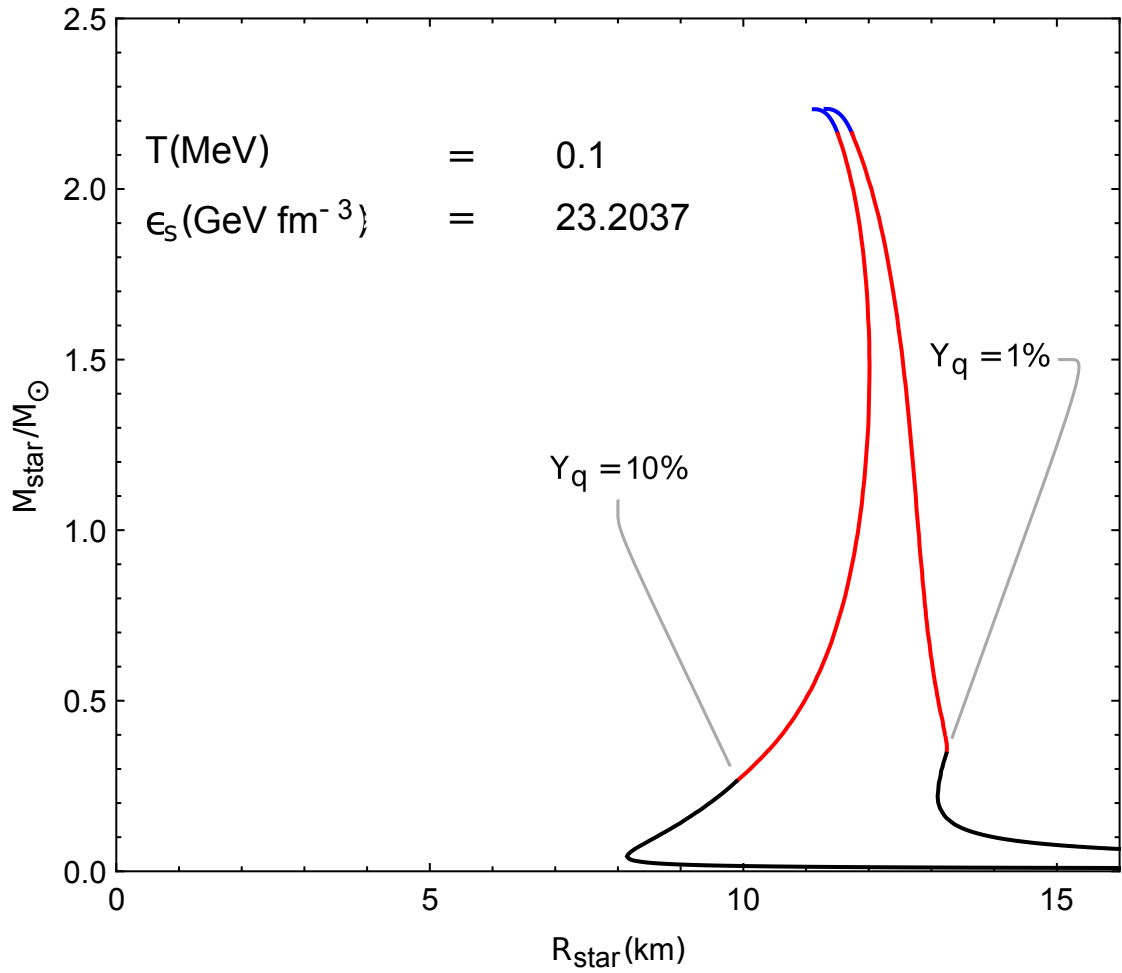
Figure 5.4: *MR* diagram of NSs with multiquark core along with FYSS nuclear shell at the temperature $T = 0.10$ MeV
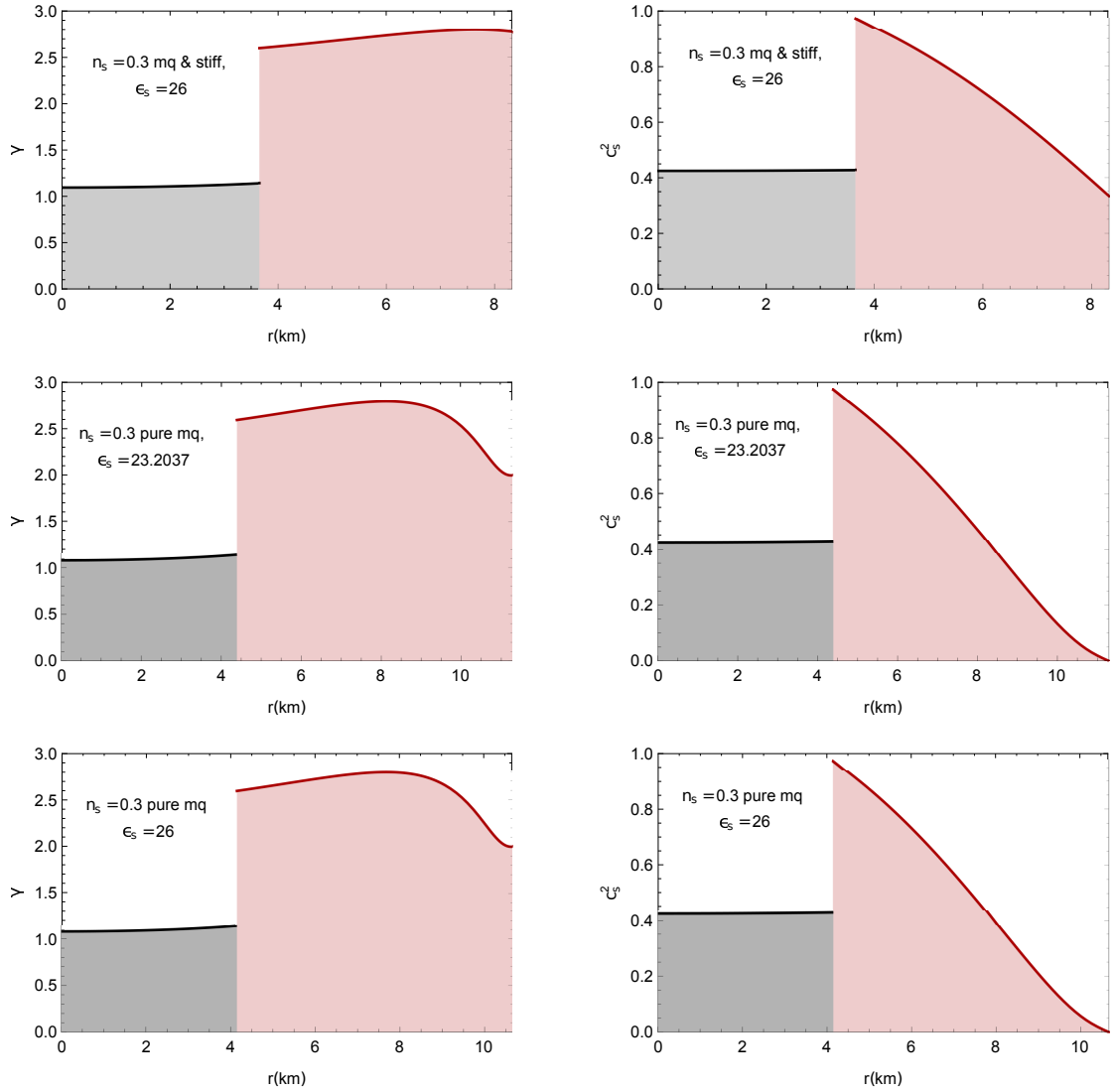
Figure 5.5: The adiabatic index $\gamma = \frac{d \ln P}{d \ln \rho}$ and c_s^2 associated with the multiquark *core* containing high and low multquark described by Eqs. (4.9) and (4.7) for each scenario

CHAPTER VI

Tidal Love Number and Tidal Deformability

This chapter investigates the possibility of the massive NS beyond $2M_\odot$ probably consisting of multiquark core and considers how the EoS for the holographic multiquark matches with the constraints from observations. Correspondingly, we focus on one of the most important parameters to constrain EoS of any compact stars called tidal deformability $\lambda_{(\text{tid})}$. First, we review background knowledge on tidal deformability $\lambda_{(\text{tid})}$ based on the Newtonian theory and focus on the relativistic theory for tidal deformation. Accordingly, $\lambda_{(\text{tid})}$ could be parameterized by Love number k_2 [30, 31, 32, 33] and the dimensionless tidal deformability parameter Λ. Then, as reported in Ref. [90], we show the calculations of the Love number k_2 and Λ of the NS with the multiquark core along with the nuclear crust described by Chiral Effective Field Theory (CET) EoS [15] and FYSS EoS [39, 40, 41] then represent them with the following parameters: the stellar mass M and compactness $C \equiv M/R$. Additionally, the tidal deformation of the multiquark star (MQS) is provided as a reference.

6.1   Newtonian Theory of Tidal Deformation

An influence of a tidal force on a stellar deformation, an orbital motion and a gravitational-wave signal could be estimated from the tidal Love number of the counterpart [91]. It is a proportional constant between the externally tidal field on the object and the corresponding multipole moment of mass distribution inside the star in the theory of gravity by Newton (see e.g. Ref. [92]). According to Ref. [93], the tidal field could be determined in term of quadrupolar oscillation by the tidal moment

$$\epsilon_{ij} \quad = \quad \frac{\partial^2 \Phi_{\text{ext}}}{\partial x^i \partial x^j}, \tag{6.1}$$

where i, j running from 1 to 3. In this section, we follow Ref. [94] to describe the Newtonian theory of tidal deformation. Consider a non-rotating spherical object A, located in an external-

gravitational field generated by a point-like source B, at a distance away from the centre of mass of A. According to the 2nd law of motion, a resultant force on a point mass m_P is given by

$$
\begin{aligned}
m_P \vec{a}_P &= -g_A m_A \cdot \hat{u}_P + \vec{F}_{AB}, \\
&= -g_A m_A \cdot \hat{u}_P + \vec{\nabla}\Phi(\vec{r}_P),
\end{aligned}
\tag{6.2}
$$

where $\vec{r}_P$ is the position from the centre of mass to the point P, the gravitational potential induced by B is $\Phi(\vec{r}_P)$ and the unit vector $\hat{u}_P \equiv \vec{r}_P/r_P$. By expanding the gradient of $\Phi(\vec{x})$ around the centre of mass up to the 1st order,

$$
\frac{\partial \Phi(\vec{x})}{\partial x_i} \approx \left.\frac{\partial \Phi(\vec{x})}{\partial x_i}\right|_{\vec{x}=0} + \left.\frac{\partial^2 \Phi(\vec{x})}{\partial x^i \partial x^j}\right|_{\vec{x}=0} \vec{x}_j = \left.\frac{\partial \Phi(\vec{x})}{\partial x_i}\right|_{\vec{x}=0} - \epsilon_{ij}\vec{x}_j.
\tag{6.3}
$$

The tidal moment ϵ_{ij} relates to the tidal force $F^{(\mathrm{tid})}$ and the external-tidal-gravitational potential $\Phi^{(\mathrm{tid})}$ by

$$
F_i^{(\mathrm{tid})} = m x_j \epsilon_{ij} = -m\frac{\partial \Phi^{(\mathrm{tid})}}{\partial x_i},
\tag{6.4}
$$

which implies that

$$
\Phi^{(\mathrm{tid})} = \frac{1}{2} x_i x_j \epsilon_{ij}.
\tag{6.5}
$$

The quadrupole moment could be written as

$$
Q_{ij} = \int d^3x \delta\rho(\vec{x}) \left(x_i x_j - \frac{1}{3} r^2 \delta_{ij} \right).
\tag{6.6}
$$

In a weak tidal field limit, up to the first order in ϵ_{ij}, the induced quadrupole field Q_{ij} could be written in terms of the tidal field as

$$
Q_{ij}^N = -\lambda_{(\mathrm{tid})}^N \epsilon_{ij}^N,
\tag{6.7}
$$

where the constant $\lambda_{(\mathrm{tid})}^N$ relates to the $\ell = 2$ Newtonian tidal Love number k_2^N by

$$
k_2^N = \frac{3}{2} G \lambda_{(\mathrm{tid})}^N R^{-5}.
\tag{6.8}
$$

The overall potential outside the body in the weak field limit could be expressed as a sum of the potential generated by the tidally deformed body and externally tidal potentials on the body

$$
\Phi_N^{\mathrm{total}} = -\frac{M}{r} - \frac{3}{r^5} Q_{ij} x_i x_j + \frac{1}{2} \epsilon_{ij} x_i x_j.
\tag{6.9}
$$

Combining Eqs. (6.7),(6.8) and (6.9), we finally have the total gravitational potential in the Newtonian limit written as

$$
\Phi_N^{\mathrm{total}} = -\frac{M}{r} + \left[\frac{2k_2^N}{G} \left(\frac{R}{r} \right)^5 + \frac{1}{2} \right] \epsilon_{ij} x_i x_j.
\tag{6.10}
$$

6.2 Relativistic Theory of Tidal Deformation

Consider a spherically symmetric and static dense star of mass M located in an externally static-quadrupolar-tidal field ϵ_{ij}. Correspondingly, the star would be deformed resulting in a change in the quadrupole moment Q_{ij}. In the stellar asymptotically rest frame, the gravitational potential could relativistically be expressed as

$$\Phi_{\text{GR}}^{\text{total}} = -\frac{(1 + g_{tt})}{2}. \tag{6.11}$$

while g_{tt} at the far away distance r from the source is given by [95]

$$-\frac{(1 + g_{tt})}{2} = -\frac{M}{r} - \frac{3Q_{ij}}{2r^3}\left(n^i n^j - \frac{1}{3}\delta^{ij}\right) + O\left(\frac{1}{r^3}\right) + \frac{1}{2}\epsilon_{ij}x^i x^j + O(r^3) \tag{6.12}$$

whereas $n^i \equiv x^i/r$. We only consider the case that the gravitational field is strong. Consider an individual body in a stationary gravitational field ϵ_{ij} with the response quadrupole moment Q_{ij}. Similar to that of Newtonian version, the quadrupole moment Q_{ij} relates to the relativistic tidal deformability ϵ_{ij} by

$$Q_{ij} = -\lambda_{\text{(tid)}}\epsilon_{ij}, \tag{6.13}$$

where the $\ell = 2$ relativistic tidal Love number k_2 relates to the parameter $\lambda_{\text{(tid)}}$ by

$$k_2 = \frac{3}{2}\lambda_{\text{(tid)}}R^{-5}. \tag{6.14}$$

Note that the relativistic k_2 is written in dimensionless unit. We can naturally decompose the multipole moments Q_{ij} and tidal field ϵ_{ij} into the following series using the spherical harmonic basis:

$$\epsilon_{ij} = \sum_{\text{m}=-2}^{2} \epsilon_{\text{m}}\mathcal{Y}_{ij}^{\text{2m}}, \tag{6.15}$$

$$Q_{ij} = \sum_{\text{m}=-2}^{2} Q_{\text{m}}\mathcal{Y}_{ij}^{\text{2m}} \tag{6.16}$$

where the tensorial spherical harmonic $\mathcal{Y}_{ij}^{\text{2m}}$ are symmetric and traceless. Note we have used the fact that the $\ell = 2$ spherical harmonics $Y_{2m}(\theta, \phi)$ could be decomposed in terms of $\mathcal{Y}_{ij}^{\text{2m}}$ as

$$Y_{2m}(\theta, \phi) = \mathcal{Y}_{ij}^{\text{2m}} n^i n^j, \tag{6.17}$$

where $n \equiv (\sin\theta\cos\phi, \sin\theta\sin\phi, \cos\theta)$. According to Eq. (6.13), the tidal deformation $\lambda_{\text{(tid)}}$ of a specific mode m ($\ell = 2$) could be represented as

$$\lambda_{\text{(tid)}} = -\frac{\epsilon_{\text{m}}}{Q_{\text{m}}}, \tag{6.18}$$

while the dimensionless tidal deformation [96] could be written as

$$\Lambda \equiv \frac{\lambda_{\text{(tid)}}}{M^5} \equiv \frac{2}{3}k_2\left(\frac{R}{M}\right)^5. \tag{6.19}$$

Again, throughout this analysis, we express k_2 and Λ in the geometric units where $G = c = 1$.

6.2.1 Estimations of the Relativistic Tidal Love Number

In the fairly strong field, e.g. a brief moment just before the binary merging, we assume the perturbation is negligible, compared with the leading term of the metric $g_{\alpha\beta}^{(0)}$,

$$ds_0^2 \quad = \quad g_{\alpha\beta}^{(0)}dx^\alpha dx^\beta = -e^{\nu(r)}dt^2 + e^{\lambda(r)}dr^2 + r^2(d\theta^2 + sin^2\theta d\phi^2). \qquad (6.20)$$

Correspondingly, the stress-energy tensor could be written as

$$T_{\alpha\beta} \quad = \quad (\rho + P)u_\alpha u_\beta + P g_{\alpha\beta}^{(0)}. \qquad (6.21)$$

Under the influence of the externally tidal gravitational field, the metric is deformed by

$$g_{\alpha\beta} \quad = \quad g_{\alpha\beta}^{(0)} + h_{\alpha\beta}, \qquad (6.22)$$

where the linearized metric perturbation is denoted by $h_{\alpha\beta}$. The $\ell = 2$, static, even-parity perturbations would only be considered in the Regge-Wheeler gauge [97, 98]. Subsequently, the first order metric perturbation on $h_{\alpha\beta}$ might be represented diagonally as in Ref. [98, 99]

$$h_{\alpha\beta} \quad = -\mathrm{diag}[e^{\nu(r)}H_0(r), e^{\lambda(r)}H_2(r), r^2K(r), r^2K(r)\mathrm{sin}^2\theta]Y_{2m}(\theta, \phi). \qquad (6.23)$$

Due to the metric perturbation, the stress-energy tensor is also perturbed by

$$\delta T_0^0 \quad = \quad -\delta\rho = -(dP/d\rho)\delta P, \qquad (6.24)$$

$$\delta T_i^i \quad = \quad \delta P,$$

where $i = 1, 2, 3$. Note that we attempt to write the perturbations in terms of δP. The linearized Einstein equation implementing the the metric and stress-energy perturbation from Eq. (6.25) and Eq. (6.23), respectively, could be written as

$$\delta G_\beta^\alpha \quad = \quad 8\pi\delta T_\beta^\alpha. \qquad (6.25)$$

Solving the linearized Einstein's field equation in $\theta - \theta$ component and $\phi - \phi$ component of the Einstein equation, we found that $\delta G_\theta^\theta - \delta G_\phi^\phi = 0$. As a result, we have $H_2 = H_0 \equiv H$. Solving the $r - \theta$ component, we obtain $\delta G_\theta^r = 0$ which relates K' to H. Subsequently, using $\delta G_\theta^\theta + \delta G_\phi^\phi = 16\pi\delta P$ to eliminate δP, the difference between the $r - r$ and the $t - t$ part of the Einstein equation results in the differential equation for $H_0 \equiv H$ (for $l = 2$) written as:

$$H''(r) + H'(r)\left[\frac{2}{r} + e^{\lambda(r)}\left(\frac{2m(r)}{r^2} + 4\pi r(P(r) - \rho(r))\right)\right]$$

$$+ \quad H(r)\left[-\frac{6e^{\lambda(r)}}{r^2} + 4\pi e^{\lambda(r)}\left(5\rho(r) + 9P(r) + \frac{\rho(r) + P(r)}{dP(r)/d\rho(r)}\right) - (\nu'(r))^2\right] = 0, \quad (6.26)$$

where $' \equiv d/dr$. The boundary conditions for Eq. (6.26) obtained by solving the Eq. (6.26) as $r \to 0$ yields

$$H(r) = a_0r^2, \qquad (6.27)$$

where a_0 is a arbitrary constant (later, for simplicity, we could be set $a_0 = 1$). To separate the unique solution from the collection of solutions specified by a_0, we need the continuity conditions of $H(r)$ and it's derivative across $r = R$. Before that, we need to know the solution of the exterior differential equation of $H(r)$. Outside the star, the Eq. (6.26) reduces to

$$H''(r) + H'(r)\left[\frac{2}{r} + e^{\lambda(r)}\left(\frac{2m(r)}{r^2}\right)\right] + H(r)\left[-\frac{6e^{\lambda(r)}}{r^2} - (\nu'(r))^2\right] = 0, \qquad (6.28)$$

$$H''(r) + \left(\frac{2}{r} - \lambda'(r)\right)H'(r) - \left(\frac{6e^{\lambda(r)}}{r^2} + (\lambda'(r))^2\right)H(r) = 0. \qquad (6.29)$$

By changing variable $x = r/M - 1$, $\frac{d}{dr} = \frac{1}{M}\frac{d}{dx}$ and $e^{-\lambda(x)} = \frac{x-1}{x+1}$, we can transform the differential equation of $H(r)$ into the associated Legendre differential equation of $H(r)$ with $l = m = 2$:

$$\frac{1}{M^2}H''(x) + \left(\frac{2}{M(x+1)} + \frac{1}{M}\left(\frac{2}{x^2-1}\right)\right)\frac{1}{M}H'(x) \qquad (6.30)$$
$$- \left(\frac{6}{M^2(x+1)^2}\left(\frac{x+1}{x-1}\right) + \frac{1}{M^2}\left(\frac{2}{x-1}\right)^2\right)H(x) = 0,$$

$$(x^2 - 1)H''(x) + 2xH'(x) - \left(6 + \frac{4}{x^2-1}\right)H(x) = 0. \qquad (6.31)$$

The standard solution to the associated Legendre differential equation of $H(x)$ could be written as

$$H(x) = c_1 Q_2^2(x) + c_2 P_2^2(x), \qquad (6.32)$$

where $P_2^2(x)$ and $Q_2^2(x)$ are associated Legendre functions of the first kind and of the second kind for $l = m = 2$, respectively. Correspondingly, the asymptotic forms of (6.32) for large x could be expressed into a form of

$$Q_2^2(x) = \frac{1}{2(x^2-1)}\left(10x - 6x^3 + 3(x^2-1)^2 \ln\left(\frac{x+1}{x-1}\right)\right), \qquad (6.33)$$

$$P_2^2(x) = 3(x^2 - 1). \qquad (6.34)$$

The exterior solution could be obtained by replacing the expressions for $Q_2^2(x)$ and $P_2^2(x)$ from Eq(6.34). This yields

$$H(r) = c_1\left(\frac{r}{M}\right)^2\left(1 - 2\frac{M}{r}\right)\left[-\frac{M(M-r)(2M^2 + 6Mr - 3r^2)}{r^2(2M-r)^2} + \frac{3}{2}\ln\left(\frac{r}{r-2M}\right)\right] \qquad (6.35)$$
$$+ 3c_2\left(\frac{r}{M}\right)^2\left(1 - 2\frac{M}{r}\right).$$

The large-r asymptotic behaviour of the solution (6.35) is given by

$$H(r) = \frac{8}{5}\left(\frac{M}{r}\right)^3 c_1 + \mathcal{O}\left(\left(\frac{M}{r}\right)^4\right) + 3\left(\frac{r}{M}\right)^2 + \mathcal{O}\left(\left(\frac{r}{M}\right)\right). \qquad (6.36)$$

After comparing the asymptotic behaviour of the exterior solution (6.36) with the expansion (6.12) and using Eq. (6.13), we could determine c_1 and c_2 by

$$c_1 = \frac{15}{8}\frac{1}{M^3}\lambda_{\text{(tid)}}\epsilon, \qquad c_2 = \frac{1}{3}M^2\lambda_{\text{(tid)}}\epsilon. \qquad (6.37)$$

Finally, we are ready to solve for $\lambda_{(tid)}$ in terms of H and its derivative at the stellar surface $r = R$ using Eqs. (6.37) and (6.35), then use the relation (6.14) to obtain the expression:

$$
\begin{aligned}
k_2 = {}& \frac{8C^5}{5}\left(1 - 2C\right)^2 \left[2 + 2C(y-1) - y\right] \times \{2C\left[6 - 3y + 3C(5y - 8)\right] \\
&+ 4C^3 \left[13 - 11y + C(3y - 2) + 2C^2(1 + y)\right] \\
&+ 3(1 - 2C)^2 \left[2 - y + 2C(y - 1)\right] \ln(1 - 2C)\}^{-1},
\end{aligned}
$$

where $C \equiv M/R$ is the compactness of the star, and $y \equiv RH'(R)/H(R)$ is a parameter determined from a numerical integration of of Eq. (6.26) in the interval $0 < r \leq R$.

The externally tidal-gravitational field from the stellar counterpart in the binary system would deform each other. As a result, a parameter for the combined tidal deformation of the binary system with masses M_1, M_2 could be specified by

$$
\tilde{\Lambda} \equiv \frac{16}{13} \frac{(M_1 + 12M_2)M_1^4 \Lambda_1 + (M_2 + 12M_1)M_2^4 \Lambda_2}{(M_1 + M_2)^5}. \tag{6.38}
$$
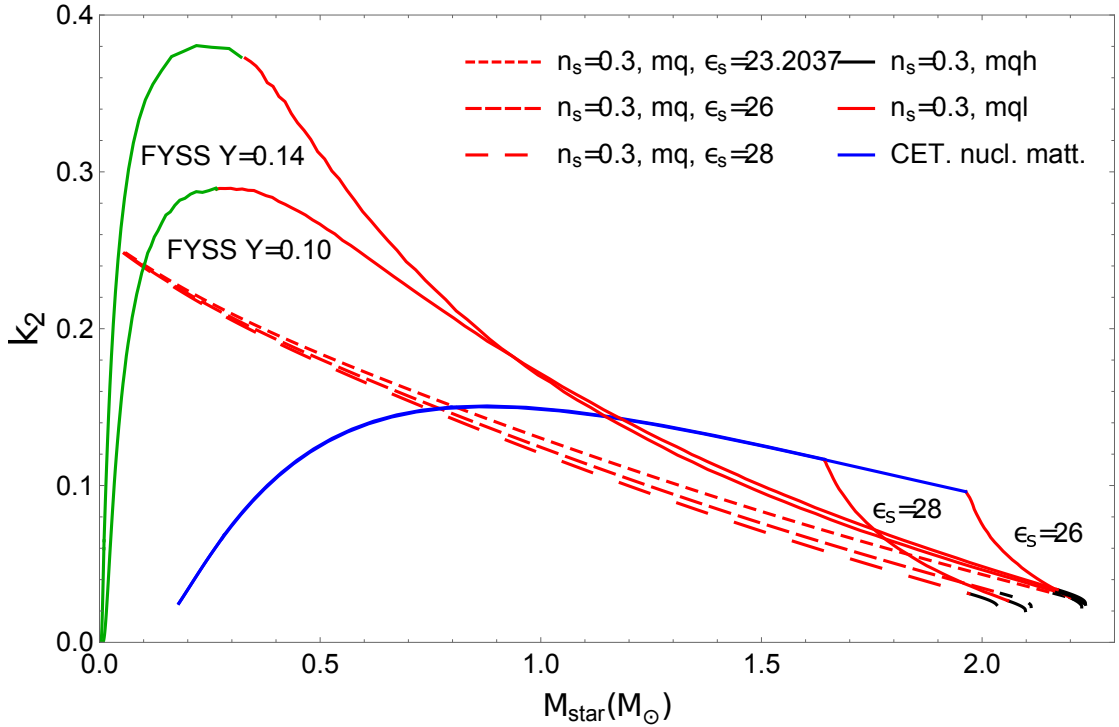
Figure 6.1: The Love number k_2 vs the stellar mass of NS with MQ core (and MQS)

6.3 Tidal Love Number and Tidal Deformability of the Massive NS with Holographic MQ core and MQS

We plotted the Love number k_2 for NS with the multiquark core and that of MQS against the stellar mass in Figure 6.1. Additionally, the dimensionless tidal parameter Λ was also plotted

EoS	$M(M_\odot)$	R(km)	k_2	Λ
mq+CET, $\epsilon_s = 26$	1.8	14.1	0.106	302
	1.9	14.2	0.100	255
	2.0	13.8	0.0752	113
	2.2	12.2	0.0285	14.0
mq+CET, $\epsilon_s = 28$	1.8	12.8	0.0619	108
	1.9	12.3	0.0453	50.0
	2.0	11.8	0.0328	22.7
mq+FYSS, $Y = 0.10$ $\epsilon_s = 23.2037$	1.5	12.0	0.100	313
	1.9	11.9	0.0577	51.8
mq+FYSS, $Y = 0.14$ $\epsilon_s = 23.2037$	1.5	11.9	0.0956	290
	1.9	11.8	0.0550	48.3

Table 6.1: Dimensionless tidal deformation Λ and tidal love number k_2 of NS with multiquark core and CET/FYSS baryonic crust

EoS	$M_1(M_\odot)$	$M_2(M_\odot)$	Λ_1	Λ_2	$\tilde{\Lambda}$
mq+CET, $\epsilon_s = 26$	1.7	1.7	418	418	418
	2.0	1.4	113	1130	391
	1.87	0.93	247	7980	1280
mq+CET, $\epsilon_s = 28$	1.7	1.7	260	260	260
	2.0	1.4	22.7	1120	313
	1.87	0.93	62.3	8080	1080
mq+FYSS, $Y = 0.10$, $\epsilon_s = 23.2037$	1.7	1.7	128	128	128
	2.0	1.4	32.2	498	158
	1.87	0.93	59.5	5670	776
mq+FYSS, $Y = 0.14$, $\epsilon_s = 23.2037$	1.7	1.7	118	118	118
	2.0	1.4	30.2	459	146
	1.87	0.93	55.4	5310	727

Table 6.2: Dimensionless tidal deformation Λ_1, Λ_2 and combined dimensionless tidal deformation $\tilde{\Lambda}$ of binary systems of NS with multiquark core and nuclear CET/FYSS crust
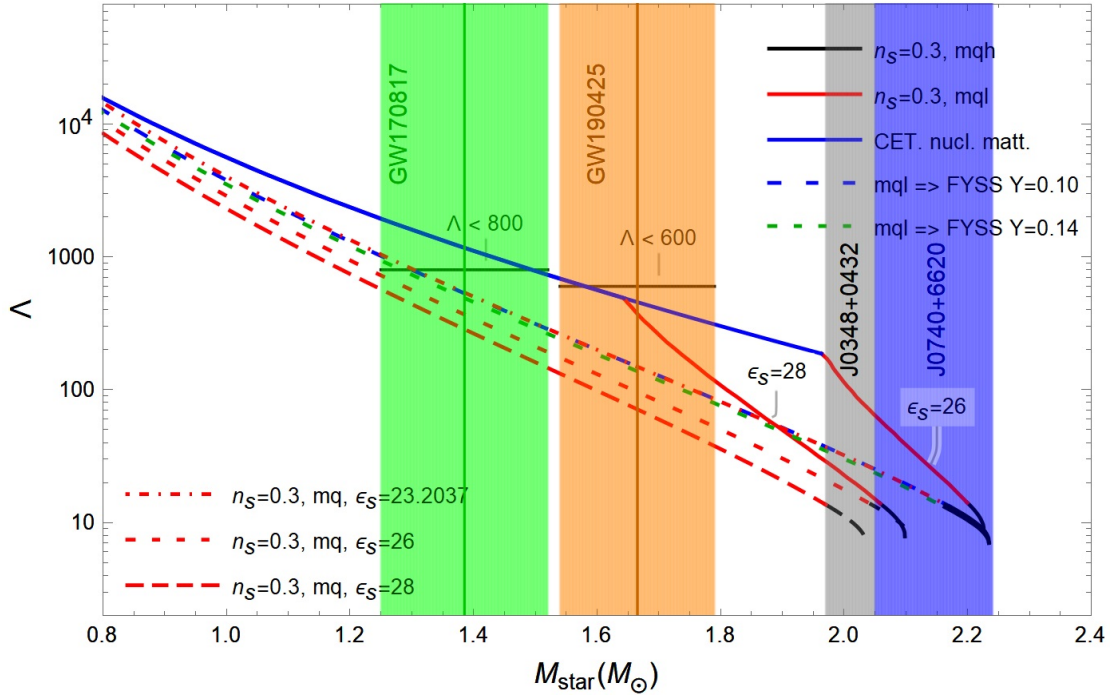
Figure 6.2: Dimensionless tidal deformation Λ vs mass of NS with MQ core (and MQS)

in Figure 6.2. We examine the NS with the $\epsilon_s = 26, 28$ (23.2037) GeV fm^{-3} multiquark core connecting to nuclear CET (FYSS) crust and the $\epsilon_s = 23.2037, 26, 28$ GeV fm^{-3} MQS. Observational constraints from the events, generating gravitational-wave signals, observed by GW170817, GW190425, and constraints discovered from LIGO/Virgo were expressed in Figure 6.2 as well. The lower and upper bound for masses in the binary systems are provided at a 90% confidence interval as $1.17 M_\odot$ and $1.60 M_\odot$. Correspondingly, in Figure 6.2, this interval could be translated to $(1.25 M_\odot, 1.52 M_\odot)$ at 68.27% confidence interval or 1σ. Likewise, for GW190425, the 90% confidence interval $(1.46 M_\odot, 1.87 M_\odot)$ turns into $(1.54 M_\odot, 1.79 M_\odot)$ at 68.27% confidence interval or 1σ. The upper bounds on Λ for individual gravitational event [13, 80] are shown in Figure 6.2 where $\Lambda < 600$ for GW190425 and $\Lambda < 800$ for GW170817. The values of k_2, Λ NS with the multiquark core with CET/FYSS baryonic crust for specific masses that are essential to compare with the result of the gravitational wave signals [13, 80, 100] are expressed in Table A.1. Table 6.2 investigates the combined tidal parameter $\tilde{\Lambda}$ of binary systems given that their masses are potentially within the mass range defined by LIGO/Virgo [13, 80]. For the binary system with masses $(1.5 - 1.7, 1.6 - 1.9) M_\odot$ (GW190425) and $(0.9 - 1.4, 1.4 - 2.3) M_\odot$ (GW170817), the unfasten constraints are $\tilde{\Lambda} < 600, 700 - 800$, respectively. We chose the mass range of each companion in the binary to be more than $1.7 M odot$ in order for it to have a multiquark core. Each binary counterpart is assumed to have its mass greater than $1.7 M_\odot$ so that its core could have the multiquark matter.
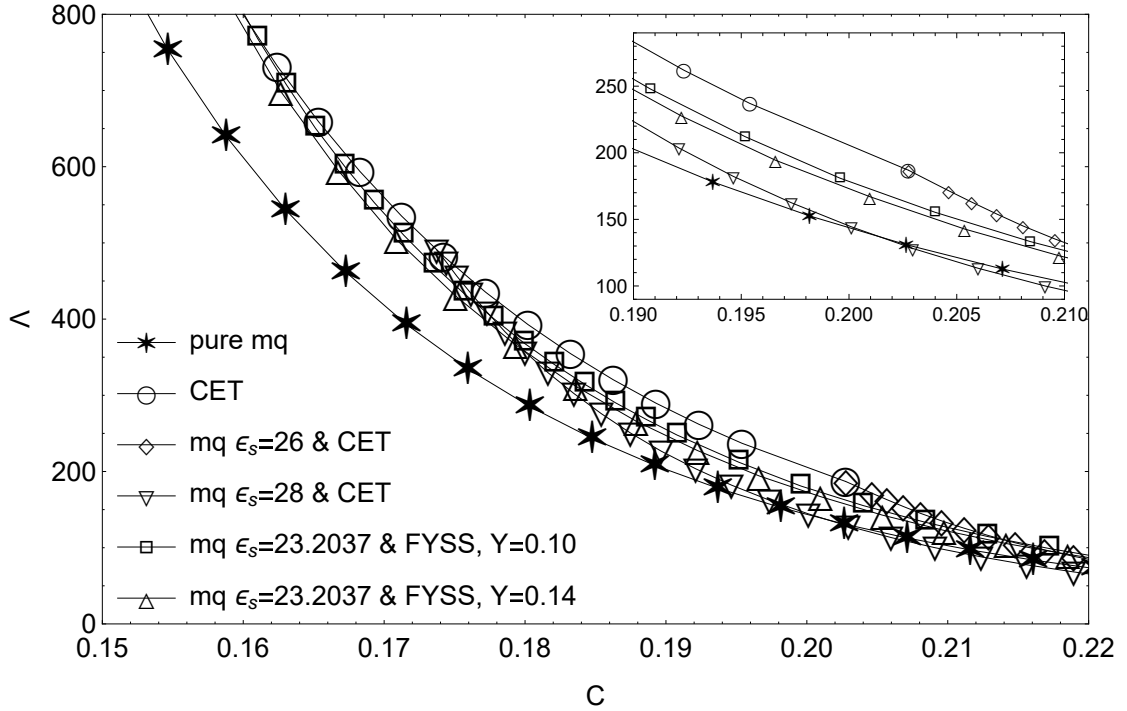
Figure 6.3: Dimensionless tidal deformation Λ versus compactness $C = M/R$ of MQS/NS with MQ core

Using the fundamental relationships between the(rotational) Love number, the moment of inertia, and the quadrupole moment, Yagi and Yunes could classify compact stars containing nuclear and quark matter into distinct universal classes [101]. It would be interesting to consider what class the MQS/NS with multiquark core belongs to. In Figure 6.3, we present the relation between the compactness $C \equiv M/R$ and the dimensionless tidal parameter Λ rather than the rotational deformability parameter.

Similarly, the tidal deformability could be divided into two distinctive classes: one for NS with pure baryonic matter and the other for pure MQS, as illustrated in Figure 6.3. At any given stellar compactness C, the NSs with the pure baryonic matter have a greater Λ than that of pure MQSs, while the hybrid stars interpolate between the two classes. As the compactness decreases, the dimensionless tidal parameter Λ for the NS with MQ core transits from the pure MQS curve to the CET curve, as seen by the inverted triangle and diamond plot in Figure 6.3. The curve representing the NS with multiquark core along with high-$Y(\equiv n_p/n_b = 0.10, 0.14)$ baryonic matter crust described by FYSS EoS tends to move toward that with baryonic matter crust described by CET EoS. As expected, all MQSs with any ϵ_s coincide on the same curve since the compactness C is independent of ϵ_s.

CHAPTER VII

Radial Pulsation of Holographic Multiquark Core/Star

In this chapter, we consider the infinitesimally radial pulsations of the multiquark cores of the massive NS (or MQS) as well as their stability under the framework of general relativity. Then, as reported by Ref. [90], we determine the radial pulsating frequencies from $0^{\text{th}} - 5^{\text{th}}$ modes as well as consider instability associated with the 0th mode of the radial pulsations of the $\epsilon_s = 23.2037$ GeV fm^{-3} holographic multiquark stars (MQS).

7.1 Linearized Adiabatic Radial Pulsation Equations

The first general relativistic approach to describe radial pulsations of spherical symmetric stars was established by Chandrasekhar [102]. Following the Refs. [103, 104], the radial pulsations could be rewritten into the form consisting of the two crucial quantities: the Lagrangian pressure perturbation denoted by ΔP and the relative radial displacement, $\xi = \Delta r / r$, where Δr refers to the radial displacement of the particle inside the star, as expressed below

$$
\xi'(r) = -\frac{1}{r}\left(3\xi(r) + \frac{\Delta P(r)}{\Gamma(r)P(r)}\right) - P'(r)\frac{\xi(r)}{(P(r) + \rho(r))}, \tag{7.1}
$$

$$
(\Delta P(r))' = \xi(r)\left[\omega^2 r e^{\lambda_0(r) - \nu_0(r)}(P_0(r) + \rho_0(r)) - 4P_0'(r)\right]
$$
$$
+ \xi(r)\left[(P_0'(r))^2\frac{r}{(P_0(r) + \rho_0(r))} - 8\pi r e^{\lambda_0(r)}(P_0(r) + \rho_0(r))P_0(r)\right]
$$
$$
+ \Delta P(r)\left[P_0'(r)\frac{1}{(P_0(r) + \rho_0(r))} - 4\pi r e^{\lambda_0(r)}(P_0(r) + \rho_0(r))\right], \tag{7.2}
$$

where $\Gamma(r)$ is an adiabatic index at a distance r away from the centre defined in the next section while each mode of the radial pulsations has the eigenfrequency ω associated with the time-dependence perturbation $\propto e^{\pm i\omega t}$.

7.2 Adiabatic Indices and Sound Speed

Generally, the EoS of the NS could be written as a series of polytrope specified by pressure as a function of the power-law of the density of the system. The power of the polytropes is nothing but an adiabatic index associated with the nuclear of matter. As the adiabatic index becomes large, the EoS becomes stiff and vice versa. The greater the adiabatic index is, the higher pressure the EoS could withstand and the more massive the star could become. Furthermore, it regulates the pulsation frequencies and the stellar dynamical equilibrium under disturbance through the compressibility of the matter inside the star (see Eq. (7.1)).

In particular, the adiabatic index might be expressed in terms of the number density n as

$$\Gamma \quad \equiv \quad \frac{n}{P}\left(\frac{dP}{dn}\right). \tag{7.3}$$

The adiabatic index written in Eq. (7.3) represents the property that the pulsating frequency alters with the number density n. Nevertheless, the relativistic adiabatic index in conventional form should be written as $\gamma = \frac{\rho}{P}(\frac{dP}{d\rho})$ when concerning the stiffness of the EoS. The pairs of values (Γ, γ, c_s^2) defined at the *maximum mass* of the massive NS with multiquark core are provided in Table 7.1. The softer multiquark EoS at high density, the smaller conventional adiabatic γ. Given that $\gamma > 5/3$, the "mql" EoS at low density becomes stiff; whereas for $\gamma \simeq 1.1$ inside the core, the "mqh" EoS becomes soft.

7.3 Determination of Radial Pulsating Frequencies of the Holographic Multiquark Star

The fact that the radial pulsation equations, governed by Eqs. (7.1) and (7.2), do not require any derivatives of $\Gamma(r)$, is a critical aspect in determining the pulsing frequencies. The computation of the 2nd order perturbation Eq. (7.2) using $\nu(r)$ from the 0th order stellar profile is subtle. As stated in Eq. (5.10), we must select $nu(r = 0)$ that, at the surface,

$$e^{\nu(R)} = 1 - \frac{2M}{R}. \tag{7.4}$$

Due to the invariance under a translation of $\nu \to \nu + \nu_0$ the associated with the zeroth-order Einstein's field equation for any arbitrary constant ν_0, the gauge fixing of ν is necessary for the computations in the 1st and 2nd order perturbations, according to Eq. (7.4). Crucially, the solution of the Schwarzschild metric matches the boundary conditions at the stellar surface. Using a replacement for $\lambda(r)$

$$e^{-\lambda(r)} = 1 - \frac{2m(r)}{r}, \tag{7.5}$$

ϵ_s (GeVfm^{-3})	(Γ, γ, c_s^2)	
	mqh	mql (small to large r)
23.2037 & FYSS, $Y = 0.10$	(1.4, 1.1, 0.43)	$(3.6 - 2.3, 2.6 - 2.2, 0.97 - 0.05)$
23.2037 & FYSS, $Y = 0.14$	(1.4, 1.1, 0.43)	$(3.6 - 2.3, 2.6 - 2.2, 0.97 - 0.06)$
26 & CET	(1.4, 1.1, 0.43)	$(3.6 - 3.1, 2.6 - 2.8, 0.97 - 0.33)$
28 & CET	(1.4, 1.1, 0.43)	$(3.6 - 3.0, 2.6 - 2.7, 0.97 - 0.26)$

Table 7.1: Values of (Γ, γ, c_s^2) for high density multiquark "mqh" in the inner core and low density "mql" in the outer core with CET/FYSS nuclear crust at the *maximum mass* of the massive NS with MQ core

we could ensure the matching of the solution of the Schwarzschild metric at the boundary in any order of perturbation.

The boundary conditions, at the core and the surface, are essential in determining the solutions of the pair of Eqs. (7.1) and (7.2). Naturally, the evanescence of the coefficient in $1/r$-term in Eq. (7.1) is a required condition, so that there would be no divergence problem as $r \to 0$. Therefore, mathematically

$$\Delta P(0) = -3(\xi(0)\Gamma(0)P(0)). \tag{7.6}$$

At the centre, $\xi(0) = 1$, the relative radial displacement must be normalised to unity. Additionally, $P(r = R) = 0$ defines a radius of the stellar surface R. Correspondingly,

$$\Delta P(R) = 0. \tag{7.7}$$

From the two radial pulsation equations associated with the given EoS, we could determine the stellar profile by shooting the eigenvalue ω^2 and substituting it into the pulsation equations. The correct value of the eigenfrequency must satisfy the boundary conditions in Eqs. (7.6) and (7.7). The collection of the verified eigenvalues must be aligned into an increasing order: $\omega_0^2 < \omega_1^2 < \cdots < \omega_n^2 < \cdots$ alongside with a set of eigenfunctions rearranged by increasing indices $\xi_0, \xi_1, \cdots, \xi_n, \cdots$,. Within the star, the eigenfunction of the typical stationary wave ξ_n contains

n nodes. We could instantaneously determine the eigenfunctions associated with the pressure perturbation $\Delta P_n(r)$.

Considering the infinitesimal radial adiabatic perturbations, the static compact stellar model becomes stable given that $\omega_n^2 > 0$ for all n. The configuration is on the borderline of stability-instability at the lowest eigenfrequency $\omega_0 = 0$ [105]. In particular, the stellar configuration is unstable for the pulsations in lower mode, while it becomes stable for a set of higher mode. Note that we only investigate the zeroth-mode instability in this research.

7.3.1 Eigenfrequencies and Instabilities

After we determine the eigenfrequencies numerically by applying the shooting process upon Eqs. (7.1), (7.2) and the TOV equations, we achieve the plot of the eigenfrequencies against the mass of the MQS shown in Figure 7.1, while that of the eigenfrequencies vs the compactness of the multiquark expressed in Figure 7.2. In the SI unit, the radial pulsating frequencies of the multiquark core oscillations are proportional to $\sqrt{\epsilon_s}$ in the SS model. For the MQS with $\epsilon_s = 23.2037$ GeV fm^{-3} and its mass about $2M_\odot$, the zeroth-mode frequency is roughly 2.5 kHz. As the central density keeps increasing and goes beyond the critical value associated with the maximum mass, instability arises for the zeroth mode. As expected, the system runs into the unstable branch of the MR diagram. Oscillations in the higher mode for the $\epsilon_s = 23.2037$ GeV fm^{-3} MQS with masses beyond $2.15M_\odot$ reveal peculiar wavy patterns of frequencies based on the interaction between the perturbative waves in the "mqh" and "mql" layers.
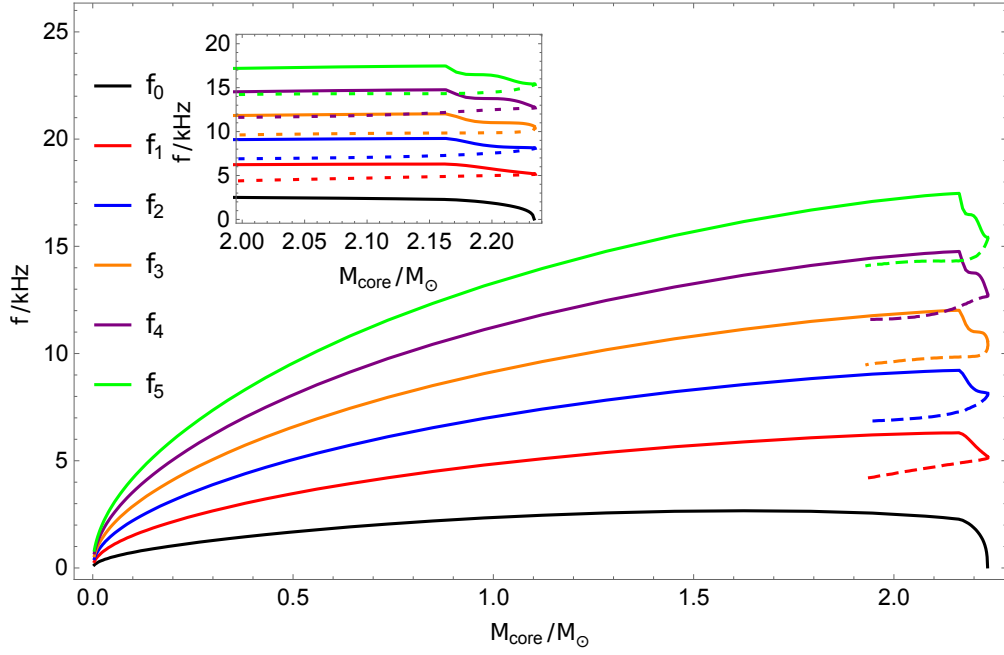
Figure 7.1: The eigenfrequencies $f_n = \omega_n/2\pi$ for $n = 0, 1, 2, 3, 4, 5$ vs mass of $\epsilon_s = 23.2037$ GeV fm^{-3} MQS/multiquark core: the solid (dashed) line represents the stable (unstable) frequencies
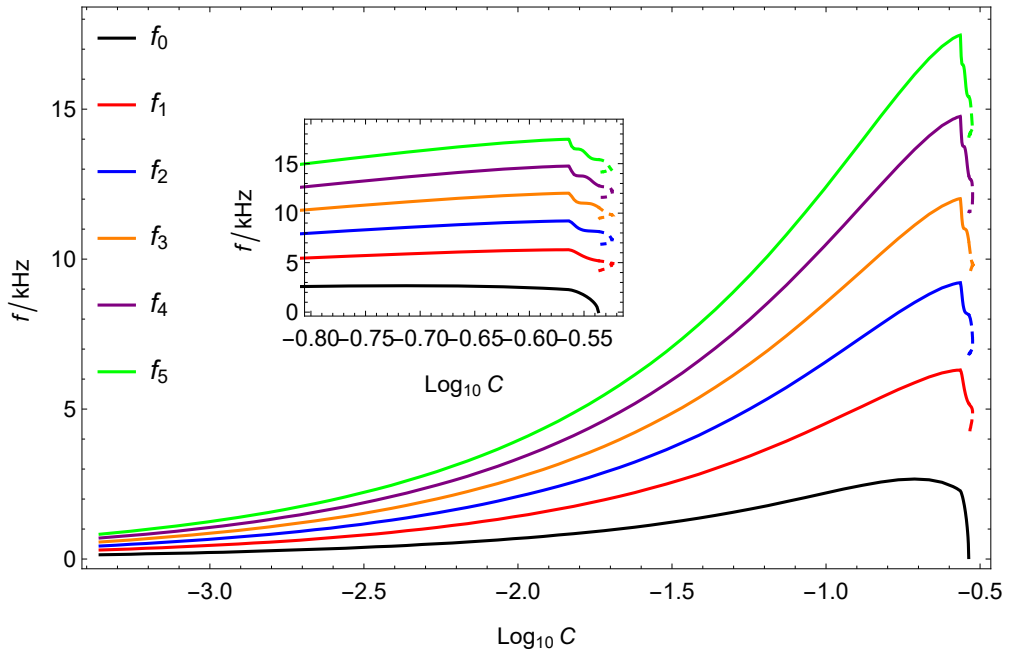
Figure 7.2: The eigenfrequencies $f_n = \omega_n/2\pi$ for $n = 0, 1, 2, 3, 4, 5$ vs compactness $C = M/R$ of $\epsilon_s = 23.2037$ GeV fm^{-3} MQS/multiquark core: the solid (dashed) line represents the stable (unstable) frequencies

CHAPTER VIII

Conclusion

Throughout this dissertation, we have implemented the EoS of the multiquark state for the inner core of NS from the low up to intermediate temperature $(T < 10^{12}K)$ based on the holographic SS model. We found that the interpolation fits nicely between the two known limits: the high-density pQCD or free quark limit and the low-density CET nuclear matter limit, using the EoS of the multiquark when setting $\epsilon_s = 23.2037 - 28$ GeV fm^{-3}, as being guided by the average-empirical-trend line between the two opposing limits of the known EoS. Once ϵ_s is chosen, the EoS of the multiquark matter is fixed. For $n_s = 0.3$, the energy density scale ϵ_s relates to a multiquark state containing $N_q \simeq 24 - 30$ (roughly $8 - 10$ baryons) per multiquark (see Figure 4.5). Additionally, during the study of the phase transitions between the general extended nuclear matter and the deconfined multiquark, it was discovered that beyond the transition point, the $n_s = 0.3$ multiquark state with $\epsilon_s > 25$ GeV fm^{-3} is favoured over the stiff nuclear matter.

At high density, the multiquark EoS has approximately the same gradient as that of pQCD, as illustrated in Figure 4.4 in Chapter 4. Although being a bound state, the characteristics of multiquark matter and that of free quarks might be almost identical. Likewise, the similar gradient between the baryonic nuclear EoS and that of low-density multiquark EoS indicates that they might share some characteristics together. Furthermore, as described in Chapter 4, the presence of the multiquark state at high and low density as anticipated by the SS model, (see Ref. [5]) offers an accurate interpolation between the baryonic nuclear matter described by CET and the free quark matter described by pQCD.

The *MR* diagram in Chapter 5, the radii and mass range for the possible massive NS with multiquark core, parameterized by $n_s = 0.3$ and several scenarios of $\epsilon_s = 26$ (28) GeV fm^{-3} connecting to CET nuclear matter crust, are $14.3 - 11.8$ $(14.0 - 11.1)$ km and $1.96 - 2.23$ $(1.64 - 2.10)M_\odot$, respectively. The more massive NS, the smaller its size. At a temperature (around a few trillion K), the population of multiquarks should become less, and the deconfined phase would consist mainly of weakly coupled quarks and gluons; however, the multiquark state, described by the SS model, is found to be more thermodynamically preferred over the QGP

phase [4] for low to intermediate temperatures at high densities. Additionally, the proportion of the multiquark in the deconfined matter becomes less at high temperatures. As a result, the weakly interacting quark and gluon dominate the deconfined state. On the other hand, at intermediate temperatures and high densities, the multiquark described by the SS model is more thermodynamically preferred over the quark-gluon plasma [4]. It might be possible that the weakly coupled quarks and gluons could form inside the core of a recently born quark star or NS, succeeded by layers of multiquark. Consequently, the mass of the NS would be greater than $2M_\odot$ given that the temperature at its core could reach over a few trillion Kelvin.

On the contrary, for billion-year-old NSs, their surface temperatures are very low comparing to the deconfinement temperature scale around trillion Kelvin.On the contrary, the surface temperatures of billion-year-old NSs are very low compared to the deconfinement temperature scale around trillion Kelvin. Therefore, we predict that the multiquark alone could form inside the cores. Subsequently, the multiquark turns into the confined-stiff-baryonic matter along, as the density decrease with the increasing distance from the centre. There might be a mixture of the multiquark state and the baryonic nuclear matter at the transition. We have studied all possibilities of the massive NS with the multiquark core parametrised by $n_s = 0.3, \epsilon_s = 26 - 28$ GeV fm^{-3} connecting to the CET nuclear matter crust and that parametrised by $n_s = 0.3, \epsilon_s = 23.2037$ GeV fm^{-3} following by the FYSS nuclear matter crust. We found that the multiquark core only exists when $M > 2.0M_\odot$ with the stellar radius around $11.1 - 14.3$ km and $11.1 - 12.1$ km for the CET and FYSS nuclear matter crust, respectively. A variation of temperature and the proton to baryon ratio results in different MR relations of NS as shown in Figure 5.3 and Figure 5.4. The effect of the temperature variation is mild; however, the outcome of the variation in the proton to baryon ratio is apparent. The greater the proton to baryon ratio is, the smaller the stellar radius of the NS becomes. According to several observation on massive NSs with masses beyond $2M_\odot$ [2, 12, 62, 106, 107, 108, 109, 110, 111, 112, 113], there are many possible massive NSs and from the perspective based on our model of massive NSs, it is possible that they contain the multiquark cores.

We have computed the tidal deformation of the MQS and massive NS with multiquark core (or hybrid star) based on the holographic SS model in Chapter 6. The stellar mass and radius [78], together with the deformation parameter k_2, Λ [90] determined from our massive NSs model, consisting of the multiquark cores inside followed by the nuclear matter crust described by CET and FYSS EoS, are compatible with observational constraints from the LIGO/Virgo. When plotted against the compactness C, the deformability of MQ-matter stars could be distinguished from that of baryonic-matter stars. The deformability vs compactness $(\Lambda - C)$ curves of the massive NSs with MQ cores or the hybrid stars provide interpolations between the pure MQSs and the pure baryonic NSs curves.

In addition, in Chapter [7], we determined the $n = 0 - 5$ modes eigenfrequencies of the radial pulsations of the multiquark core parametrised by $\epsilon_s = 23.2037$ GeV fm^{-3}, $n_s = 0.3$ throughout the whole mass range. As a result, we discovered the fundamental mode frequency to be about 2.5 kHz at the maximal masses of roughly $2M_\odot$. The fundamental frequency shows a unique characteristic that gradually rises as the mass increases until reaching the maximum mass and then suddenly descends to a small value, as shown in Figure [7.1]. The appearance of wavy shapes of the higher modes around the maximum mass might be due to the opposition between radial waves in the low ("mql") and high ("mqh") density layers inside the MQ core.

Significantly, all of the curves for higher mode eigenfrequencies in the tidal deformability Λ vs compactness C (and vs mass M) graphs have sharp bendings at the transition between the multiquark and nuclear matter crust. Practically, this characteristic may indicate the existence of a multiquark core inside the massive NS. The collection of the pulsating frequencies of the multiquark core could be matched and analysed with that from observations and then compared to other models. Hopefully, this procedure might uncover some properties of the exotic nuclear matter inside the compact stars.

Generally, the colour superfluid conductor (CSC) phase could exist at a very high density. Arguably, it is uncertain which one of multiquark or CSC exists or whether all of them could coexist in the core of massive NSs given the proper circumstances (for more information on the holographic model of CSC with the tidal deformability see e.g. Refs. [114], [115]). So maybe in the less dense and colder core of massive NS, the CSC might be more thermodynamically favoured over the multiquark, while the multiquark could be more preferred over the CSC in the denser and intermediately hotter layers inside the core where the confined nuclear is more preferred in the crust. However, the parameters from the CSC EoS and that from the multiquark EoS satisfy the observational constraints from the $2M_\odot$ NS while the results are quite similar. Further investigations on the observational parameters of a massive NS and future models with the mixed phases would be interesting.

APPENDIX

APPENDIX A

Conversion Table between Dimensionless and Physical Quantities

quantity	dimensionless variable	physical variable
pressure	P	$\epsilon_s P$
density	ρ	$\dfrac{\epsilon_s}{c^2}\rho$
chemical potential	μ	$\epsilon_s \mu \text{ fm}^3$
number density	n	$n \text{ fm}^{-3}$
mass	M	$\dfrac{c^4}{\sqrt{G^3 \epsilon_s}} M$
radius	r	$\dfrac{c^2}{\sqrt{G \epsilon_s}} r$
angular frequency	ω	$\dfrac{\sqrt{G \epsilon_s}}{c} \omega$

Table A.1: Conversion from the dimensionless to physical quantities with ϵ_s in GeV fm^{-3} unit

APPENDIX B

Derivation of Infinitesimal Radial Pulsation Equations

In this appendix, we expressed the derivation of radial pulsation equations by using a harmonic-time-dependent perturbation, as originally formulated by Ref. [102], in great detail. Later, the radial pulsations could be rewritten in terms of $\xi = \Delta r/r$ or the variation of relative displacement given that the radial displacement of matter particles inside the star is denoted by Δr, and ΔP refers to the Lagrangian pressure perturbation, following Refs. [103, 104].

B.1 Infinitesimal Radial Pulsation

Recall that the metric tensor for any static and spherically symmetric stars, as expressed in Eq. (5.1), could be described by :

$$ds^2 = g_{\mu\nu}dx^\mu dx^\nu = e^{\nu(r)}dt^2 - e^{\lambda(r)}dr^2 - r^2 d\theta^2 - r^2\sin^2\theta d\phi^2.$$

Solving the Einstein's field equation

$$G^\alpha_\beta = 8\pi T^\alpha_\beta \tag{B.1}$$

up to the 0th order of perturbation by substituting the metric in Eq. (5.1) for the $t-t$, $r-r$ components and the relation $\nabla_i T^i_j = 0$ with $i, j = 1, 2, 3$ result in the following relations:

$$(re^{\lambda_0(r)})' = 1 - 8\pi r^2 \rho_0(r) \tag{B.2}$$

$$\frac{e^{-\lambda_0(r)}}{r}\nu'_0(r) = \frac{1}{r^2}(1 - e^{\lambda_0(r)}) + 8\pi P_0(r) \tag{B.3}$$

$$P'(r) = -\frac{1}{2}(P_0(r) + \rho_0(r))\nu'(r). \tag{B.4}$$

Considering the difference term $G^r_r - G^t_t$, we have

$$\frac{e^{-\lambda_0(r)}}{r}(\lambda_0(r) + \nu_0(r))' = 8\pi(P_0(r) + \rho_0(r)). \tag{B.5}$$

Recall the TOV equations for unperturbed static and spherically symmetric stars of the form

$$\frac{dP_0(r)}{dr} = -\left(1 - \frac{2M(r)}{r}\right)^{-1}(P_0(r) + \rho_0(r))\left(\frac{M(r)}{r^2} + 4\pi r P_0(r)\right), \tag{B.6}$$

$$M'(r) = 4\pi r^2 \rho_0(r). \tag{B.7}$$

B.1.1 Equations Governing Infinitesimal Radial Pulsation

Assuming that the pulsation is small, we had better used the 1$^{\text{st}}$ order perturbation and neglect all of the higher order terms. Then, the 4-velocity of the perfect fluid within the star could be written as

$$\begin{aligned}
u^t &= e^{-\nu_0(r)/2}, & u^r &= e^{-\nu_0(r)/2}v(r), \\
u_t &= -e^{\nu_0(r)/2}, & u_r &= e^{\lambda_0(r)-\nu_0(r)/2}v(r),
\end{aligned} \tag{B.8}$$

where the pulsating velocity is

$$v(r) \equiv \frac{dr}{dt}. \tag{B.9}$$

Correspondingly, the stress-energy tensor components of the fluid defined in the Eq. (5.2) could be written as

$$\begin{aligned}
T^t_t &= \rho(r), \quad \text{and} \quad T^r_r = T^\theta_\theta = T^\phi_\phi = -P(r), \tag{B.10} \\
T^t_r &= -(P_0(r) + \rho_0(r))u^t u_r = -e^{\lambda_0(r)-\nu_0(r)}(P_0(r) + \rho_0(r))v(r), \tag{B.11} \\
T^r_t &= -(P_0(r) + \rho_0(r))u^r u_t = (P_0(r) + \rho_0(r))v(r).
\end{aligned}$$

Then, we could define the infinitesimal radial pulsation of various quantities by the Eulerian perturbation, in which the observer locates at a specific point, as follows:

$$\begin{aligned}
\lambda(r) &\to \lambda_0(r) + \delta\lambda(r), & \nu(r) &\to \nu_0(r) + \delta\nu(r), \tag{B.12} \\
P(r) &\to P_0(r) + \delta P(r), & \rho(r) &\to \rho_0(r) + \delta\rho(r).
\end{aligned}$$

Accordingly, performing the radial perturbation (B.12) on (B.10), (B.3) and (B.2), we have

$$\partial_r(r e^{\lambda_0(r)}\delta\lambda(r)) = 8\pi r^2 \delta\rho(r) \tag{B.13}$$

$$\frac{e^{-\lambda_0(r)}}{r}(\partial_r\delta\nu(r) - \nu'_0(r)\delta\lambda(r)) = \frac{e^{-\lambda_0(r)}}{r^2}\Delta\lambda(r) + 8\pi\delta P(r) \tag{B.14}$$

while applying the radial perturbation on Eq. (B.11) and the conservation of stress-energy tensor $\nabla_i T^i_j = 0$ result in

$$\frac{e^{-\lambda_0(r)}}{r}\partial_t\delta\lambda(r,t) = -8\pi(P_0(r) + \rho_0(r))v(r,t), \tag{B.15}$$

and

$$
\begin{aligned}
e^{\lambda_0(r)-\nu_0(r)}(P_0(r)+\rho_0(r))\partial_t v(r,t) \quad &+ \quad \partial_r \delta P(r,t) \\
+\frac{1}{2}(P_0(r)+\rho_0(r))\partial_r \delta \nu(r,t) \quad &+ \quad \frac{1}{2}\nu_0'(r)(\delta P(r,t)+\delta\rho(r,t))=0.
\end{aligned}
\tag{B.16}
$$

It would be convenient to rewrite all equations governing the radial pulsation by introducing the "Lagrangian displacement" δr where the fluid velocity could be defined by

$$
v \equiv \frac{\partial \delta r}{\partial t}.
\tag{B.17}
$$

Eq. (B.15) could be integrated with respect to t. This gives

$$
\frac{e^{-\lambda_0(r)}}{r}\delta\lambda(r) \;\; = \;\; -8\pi(P_0(r)+\rho_0(r))\delta r(r).
\tag{B.18}
$$

Then, the Eq. (B.5) becomes

$$
\delta\lambda(r) \;\; = \;\; -\delta r(r)(\lambda_0(r)+\nu_0(r))'.
\tag{B.19}
$$

Eqs. (B.13) and (B.18) could then be written as

$$
\delta\rho(r) \;\; = \;\; -\frac{1}{r^2}\left[r^2(P_0(r)+\rho_0(r))\delta r(r)\right]',
\tag{B.20}
$$

or on the other hand,

$$
\delta\rho(r) \;\; = \;\; -\delta r(r)\rho_0'(r) - \delta r(r)P_0'(r) - (P_0(r)+\rho_0(r))\frac{1}{r^2}(r^2\delta r(r))'.
\tag{B.21}
$$

Replacing $P_0'(r)$ with Eq. (B.4), we have

$$
\delta\rho(r) \;\; = \;\; -\delta r(r)\rho_0'(r) - (P_0(r)+\rho_0(r))\frac{e^{\nu_0(r)/2}}{r^2}(r^2 e^{-\nu_0(r)/2}\delta r(r))'.
\tag{B.22}
$$

Next, with $\delta\lambda(r)$ getting replaced by that of Eq. (B.14), consider the replacement result together with the Eq. (B.18), we obtain

$$
\frac{e^{-\lambda_0(r)}}{r}(\delta\nu(r))' \;\; = \;\; 8\pi\left[\delta P(r) - (P_0(r)+\rho_0(r))\left(\nu_0'(r)+\frac{1}{r}\right)\delta r(r)\right],
\tag{B.23}
$$

or in the perspective of Eq. (B.5),

$$
(P_0(r)+\rho_0(r))(\delta\nu(r))' \;\; = \;\; \left[\delta P(r) - (P_0(r)+\rho_0(r))\left((\nu_0(r))'+\frac{1}{r}\right)\delta r(r)\right](\lambda_0'(r)+\nu_0'(r)).
\tag{B.24}
$$

Now, we shall assume that, under the radial pulsation, any time-dependent-perturbation quantities $\Box(r,t)$ could be written as

$$
\Box(r,t) = \Box(r)e^{\pm i\omega t}
\tag{B.25}
$$

where ω is the radial pulsating frequency and $\Box(r)$ represents the amplitudes $(\delta\lambda(r), \delta\nu(r), \delta P(r)$ and $\delta\rho(r))$ of the time-dependent perturbation. Consequently, we have

$$
\begin{aligned}
\omega^2 e^{\lambda_0(r)-\nu_0(r)}(P_0(r) + \rho_0(r))\delta r(r) &= \delta P'(r) + \delta P(r)(\frac{1}{2}\lambda_0'(r) + \nu_0'(r)) + \frac{1}{2}\nu_0'(r)\delta\rho(r) \\
&- \frac{1}{2}(P_0(r) + \rho_0(r))\left(\nu_0'(r) + \frac{1}{r}\right)(\lambda_0'(r) + \nu_0'(r))\,\delta r(r),
\end{aligned}
$$
(B.26)

where $(P_0(r) + \rho_0(r))\partial\delta\nu(r)/\partial r$ has been substituted with Eq. (B.24). Furthermore, $\delta\rho$ could be expressed in terms of δr and the unperturbed variables by Eqs. (B.21) and (B.22).

B.1.2 Conservation of the Baryon Number

To express δP in terms of δr consistently with the field equations, we need an additional assumption supplement to the field equations. As there is a flow of fluid with the displacement δr caused by the variation in pressure δP, there must be a conservation of the baryon number described as follows.

For the given baryon number per unit volume $n(r,t)$, its conservation could relativistically be expressed as

$$
\nabla_\mu(n(r,t)u^\mu) = 0,
$$
(B.27)

$$
\frac{1}{\sqrt{-g}}\partial_\mu(\sqrt{-g}n(r,t)u^\mu) = 0,
$$
(B.28)

$$
\partial_\mu(n(r,t)u^\mu) + n(r,t)u^\mu \frac{1}{\sqrt{-g}}\partial_\mu\sqrt{-g} = 0.
$$
(B.29)

With in the framework of the linearized, the non-zero terms given by Eqs. (B.8) and (B.29) becomes

$$
\begin{aligned}
&\partial_t(n(r,t)e^{-\nu_0(r)/2}) + \partial_r(n(r,t)v(r,t)e^{-\nu_0(r)/2}) \\
&+ \frac{n(r,t)e^{-\nu_0(r)}}{e^{(\lambda_0(r)+\nu_0(r))/2}r^2\sin\theta}\partial_t\left(e^{(\lambda_0(r)+\nu_0(r))/2}r^2\sin\theta\right) \\
&+ \frac{n(r,t)e^{-\nu_0(r)}}{e^{(\lambda_0(r)+\nu_0(r))/2}r^2\sin\theta}\partial_r\left(e^{(\lambda_0(r)+\nu_0(r))/2}r^2\sin\theta\right) = 0
\end{aligned}
$$
(B.30)

or alternatively,

$$
\begin{aligned}
&e^{-\nu_0(r)/2}\partial_t\delta n(r,t) + \frac{1}{r^2}\partial_r\left(n_0(r)v(r,t)e^{-\nu_0(r)/2}\right) + \frac{1}{2}n_0(r)e^{-\nu_0(r)/2}\partial_t\delta\lambda(r,t) \\
&+ \frac{1}{2}n_0(r)e^{-\nu_0(r)/2}v(r,t)\partial_r(\lambda_0(r) + \nu_0(r)) = 0.
\end{aligned}
$$
(B.31)

Consider the time-evolution number density $n(r,t)$ written as

$$
n(r,t) = n_0(r) + \delta n(r,t),
$$
(B.32)

then the Eq. (B.31) could be integrated into the following form

$$\delta n(r) + \frac{e^{\nu_0(r)/2}}{r^2}\left(n_0(r)r^2\delta r(r)e^{-\nu_0(r)/2}\right)' + \frac{1}{2}n_0(r)\left[\delta\lambda(r) + (\lambda_0'(r) + \nu_0'(r))\delta r(r)\right] = 0. \quad \text{(B.33)}$$

The last term on the Eq. (B.33) becomes zero due to Eq. (B.19), Thus, the remaining part could be written as

$$\delta n(r) = -\frac{e^{\nu_0(r)/2}}{r^2}\left(n_0(r)r^2\delta r(r)e^{-\nu_0(r)/2}\right)', \quad \text{(B.34)}$$

$$\delta n(r) = -\delta r(r)n_0'(r) - n_0(r)\frac{e^{\nu_0(r)/2}}{r^2}\left(r^2\delta r(r)e^{-\nu_0(r)/2}\right)' \quad \text{(B.35)}$$

or instead,

$$n(r) \equiv n(\rho, P), \quad \text{(B.36)}$$

$$n'(r) = \frac{\partial n(\rho, P)}{\partial \rho}\rho'(r) + \frac{\partial n(\rho, P)}{\partial P}P'(r). \quad \text{(B.37)}$$

Rearranging $P'(r)$ as the subject, we have

$$P_0'(r) = \frac{1}{\partial n(\rho, P)/\partial P}\left[n_0'(r) - \frac{\partial n_0(r)}{\partial \rho}\rho_0'(r)\right]. \quad \text{(B.38)}$$

With EoS written as

$$n \equiv n(\rho, P). \quad \text{(B.39)}$$

From (B.22)and (B.37), we obtain the variation in $P(r)$ as

$$\delta P(r) = \frac{1}{\partial n(\rho, P)/\partial P}\left[n_0'(r)\delta r(r) - n_0(r)\frac{e^{\nu_0(r)/2}}{r^2}\left(r^2 e^{-\nu_0(r)/2}\delta r(r)\right)'\right.$$
$$\left. - \frac{\partial n_0(r)}{\partial \rho}\left(-\rho_0'(r)\delta r(r) - (P_0(r) + \rho_0(r))\frac{e^{\nu_0(r)/2}}{r^2}\left(r^2 e^{-\nu_0(r)/2}\delta r(r)\right)'\right)\right].$$

Note that the first and the second terms in the squared bracket could be reduced further

$$\delta P(r) = -\delta r(r)\overbrace{\left[\frac{1}{\partial n(\rho, P)\partial P}\left(n_0'(r) - \frac{\partial n_0(r)}{\partial \rho}\rho_0'(r)\right)\right]}^{P_0'(r)}$$
$$-\underbrace{\left[\frac{1}{\partial n(\rho, P)/\partial P}\left(n_0(r) - (P_0(r) + \rho_0(r))\frac{\partial n_0(r)}{\partial \rho}\right)\right]}_{\Gamma(r)P_0(r)}\frac{e^{\nu_0(r)/2}}{r^2}\left(r^2 e^{-\nu_0(r)/2}\delta r(r)\right)',$$

$$\text{(B.40)}$$

then the variation in pressure could be rewritten as

$$\delta P(r) = -\delta r(r)P_0'(r) - \Gamma(r)P_0(r)\frac{e^{\nu_0(r)/2}}{r^2}\left(r^2 e^{-\nu_0(r)/2}\delta r(r)\right)' \quad \text{(B.41)}$$

where the adiabatic index for radial pulsation is defined by

$$\Gamma(r) \equiv \frac{1}{P(r)\partial n(\rho, P)/\partial P}\left(n_0(r) - (P_0(r) + \rho_0(r))\frac{\partial n_0(r)}{\partial \rho}\right). \quad \text{(B.42)}$$

B.1.3 The Pulsating Equation in Lagrangian Perturbation

To simplify the perturbation further, we translate the Eulerian perturbations to the Lagrangian perturbations where the observer is now comoving with the fluid. Correspondingly, we have

$$\underbrace{\delta P(r) + \delta r(r) P_0'(r)}_{\Delta P(r)} = -\Gamma(r) P_0(r) \frac{e^{\nu_0(r)/2}}{r^2} \left(r^3 e^{-\nu_0(r)/2} \underbrace{(\delta r(r)/r)}_{\xi(r)} \right)', \tag{B.43}$$

$$\Delta P(r) = -\Gamma(r) P_0(r) \frac{e^{\nu_0(r)/2}}{r^2} \left(3r^2 e^{-\nu_0(r)/2} \xi(r) + r^3 e^{-\nu_0(r)/2} \xi(r) \left(-\frac{1}{2} \nu_0'(r) \right) \right.$$
$$\left. + r^3 e^{-\nu_0(r)/2} \xi'(r) \right), \tag{B.44}$$

$$\Delta P(r) = -\Gamma(r) P_0(r) \left(3\xi(r) - r \frac{\xi(r)}{2} \nu_0'(r) + r\xi'(r) \right). \tag{B.45}$$

Note that we have used $\Delta \square(r) = \delta \square(r) + \delta r(r) \square_0'(r)$, and introduced the relative displacement $\xi \equiv \Delta r/r = \delta r/r$. Using the relation from TOV equation (5.9): $\frac{1}{2}\nu_0'(r) = -\frac{P_0'(r)}{(P(r)+\rho(r))}$, then the 1$^{\text{st}}$ fundamental equation for radial pulsations, expressed in terms of $\xi(r)$ as already represented in Eq. (7.1), is given by

$$\xi'(r) = -\frac{1}{r} \left(3\xi(r) + \frac{\Delta P(r)}{\Gamma(r)P(r)} \right) - P'(r) \frac{\xi(r)}{(P(r) + \rho(r))}.$$

From (B.22), (B.26) and (B.42), we obtain

$$\omega^2 e^{\lambda_0(r) - \nu_0(r)} (P_0(r) + \rho_0(r)) \delta r(r)$$

$$= (\delta r(r) P_0'(r))' - \left(\frac{1}{2} \lambda_0'(r) + \nu_0'(r) \right) \delta r(r) P_0'(r)$$

$$- \frac{1}{2} (P_0(r) + \rho_0(r)) \left(\nu_0'(r) + \frac{1}{r} \right) (\lambda_0'(r) + \nu_0'(r)) \delta r(r)$$

$$- \frac{1}{2} \nu_0'(r) \left\{ [(P_0(r) + \rho_0(r)) \delta r(r)]' + \frac{2}{r} (P_0(r) + \rho_0(r)) \delta r(r) \right\}$$

$$- e^{-(\lambda_0(r) + 2\nu_0(r))/2} \left[e^{-(\lambda_0(r) + 3\nu_0(r))/2} \frac{\Gamma(r) P_0(r)}{r^2} \left(r^2 e^{-\nu_0(r)/2} \delta r(r) \right)' \right]'. \tag{B.46}$$

Substituting $P_0'(r)$ with its value given by the Eq. (B.4), the first two terms on the RHS of the Eq. (B.46) could be combined into

$$\frac{1}{2} (P_0(r) + \rho_0(r)) \left(\nu_0''(r) - \frac{1}{2} \lambda_0'(r) \nu_0'(r) - \frac{1}{r} \lambda_0'(r) - \frac{3}{r} \nu_0'(r) \right) \delta r(r). \tag{B.47}$$

On the other hand, the G_r^r components of the Einstein's field equation under equilibrium condition is

$$16\pi P_0(r) e^{\lambda_0(r)} = \nu_0''(r) - \frac{1}{2} \lambda_0'(r) \nu_0'(r) + \frac{1}{2} (\nu_0'(r))^2 + \frac{1}{r} (\nu_0'(r) - \lambda_0'(r)). \tag{B.48}$$

With Eq. (B.48), the expression in Eq. (B.47) becomes

$$\frac{4}{r} P_0'(r) \delta r(r) + 8\pi e^{\lambda_0(r)} P_0(r) (P_0(r) + \rho_0(r)) \delta r(r) - \frac{1}{(P_0(r) + \rho_0(r))} (P_0'(r))^2 \delta r(r), \tag{B.49}$$

where we have used Eq. (B.4) again. With a reduction of the four terms, the Eq. (B.46) becomes

$$\omega^2 e^{\lambda_0(r)-\nu_0(r)}(P_0(r)+\rho_0(r))\delta r(r)$$

$$= \frac{4}{r}P_0'(r)\delta r(r) + 8\pi e^{\lambda_0(r)}P_0(r)(P_0(r)+\rho_0(r))\delta r(r) - \frac{1}{(P_0(r)+\rho_0(r))}(P_0'(r))^2\delta r(r)$$

$$- e^{-(\lambda_0(r)+2\nu_0(r))/2}\left[e^{-(\lambda_0(r)+3\nu_0(r))/2}\frac{\Gamma(r)P_0(r)}{r^2}\left(r^2 e^{-\nu_0(r)/2}\delta r(r)\right)'\right]'. \qquad \text{(B.50)}$$

Similarly, we rearrange the Eq. (B.50) by using the relative displacement $\xi \equiv \Delta r/r = \delta r/r$

$$\omega^2 e^{\lambda_0(r)-\nu_0(r)}(P_0(r)+\rho_0(r))r\,\overbrace{\delta r(r)/r}^{\xi(r)}$$

$$= 4P_0'(r)\overbrace{\delta r(r)/r}^{\xi(r)} + 8\pi e^{\lambda_0(r)}rP_0(r)(P_0(r)+\rho_0(r))\overbrace{\delta r(r)/r}^{\xi(r)}$$

$$- \frac{r}{(P_0(r)+\rho_0(r))}(P_0'(r))^2\overbrace{\delta r(r)/r}^{\xi(r)}$$

$$- e^{-(\lambda_0(r)+2\nu_0(r))/2}\left[e^{-(\lambda_0(r)+3\nu_0(r))/2}\frac{\Gamma(r)P_0(r)}{r^2}\left(r^3 e^{-\nu_0(r)/2}\overbrace{\delta r(r)/r}^{\xi(r)}\right)'\right]'.$$

$$\text{(B.51)}$$

Then, we could simplify the RHS of the Eq. (B.51) further by multiplying the whole equation with $1/P_0(r)$ which can be expressed as follows:

$$\xi(r)\left[\omega^2 r e^{\lambda_0(r)-\nu_0(r)}\frac{(P_0(r)+\rho_0(r))}{P_0(r)} - \frac{4}{P_0(r)}P_0'(r) - 8\pi r e^{\lambda_0(r)}(P_0(r)+\rho_0(r))\right.$$

$$\left.+ \frac{r}{P_0(r)(P_0(r)+\rho_0(r))}(P_0'(r))^2\right]$$

$$= -\frac{e^{-(\lambda_0(r)+2\nu_0(r))/2}}{P_0(r)}\left[e^{-(\lambda_0(r)+3\nu_0(r))/2}\frac{\Gamma(r)P_0(r)}{r^2}\left\{3r^2 e^{-\nu_0(r))/2}\xi(r) + r^3 e^{-\nu_0(r))/2}\xi'(r)\right.\right.$$

$$\left.\left.+ r^3 e^{-\nu_0(r))/2}\frac{\xi(r)}{(P_0(r)+\rho_0(r))}P_0'(r)\right\}\right]'$$

$$= -\frac{e^{-(\lambda_0(r)+2\nu_0(r))/2}}{P_0(r)}\left[e^{-(\lambda_0(r)+2\nu_0(r))/2}\Gamma(r)P_0(r)\left\{3\xi(r) + r\xi'(r) + r\frac{\xi(r)}{(P_0(r)+\rho_0(r))}P_0'(r)\right\}\right]'$$

$$= -\frac{e^{-(\lambda_0(r)+2\nu_0(r))/2}}{P_0(r)}\left[e^{-(\lambda_0(r)+2\nu_0(r))/2}\Gamma(r)P_0(r)\left\{3\xi(r) + \left(-3\xi(r) - \frac{\eta(r)}{\Gamma(r)}\right.\right.\right.$$

$$\left.\left.\left.- r\frac{\xi(r)}{(P_0(r)+\rho_0(r))}P_0'(r)\right) + r\frac{\xi(r)}{(P_0(r)+\rho_0(r))}P_0'(r)\right\}\right]'$$

$$= \frac{e^{-(\lambda_0(r)+2\nu_0(r))/2}}{P_0(r)}\left[e^{-(\lambda_0(r)+2\nu_0(r))/2}P_0(r)\eta(r)\right]'$$

$$= \frac{1}{P_0(r)}\left[\left(\frac{1}{2}\lambda_0'(r) + \nu_0'(r)\right)P_0(r)\eta(r) + P_0'(r)\eta(r) + P_0(r)\eta'(r)\right]$$

$$= \left(\frac{1}{2}(\lambda_0(r) + \nu_0(r))' + \frac{1}{2}\nu_0'(r)\right)\eta(r) + \frac{\eta(r)}{P_0(r)}P_0'(r) + \eta'(r)$$

$$= \left(\frac{1}{2}\left[8\pi(P_0(r)+\rho_0(r))r e^{\lambda_0(r)}\right] - \frac{1}{(P_0(r)+\rho_0(r))}P_0'(r)\right)\eta(r) + \frac{\eta(r)}{P_0(r)}P_0'(r) + \eta'(r)$$

$$= \eta(r)\left[4\pi(P_0(r)+\rho_0(r))r e^{\lambda_0(r)} + \left(\frac{1}{P_0(r)} - \frac{1}{(P_0(r)+\rho_0(r))}\right)P_0'(r)\right] + \eta'(r).$$

Consequently, we obtain

$$\xi(r)\left[\omega^2 r e^{\lambda_0(r)-\nu_0(r)}\frac{(P_0(r)+\rho_0(r))}{P_0(r)}-\frac{4}{P_0(r)}P_0'(r)-8\pi r e^{\lambda_0(r)}(P_0(r)+\rho_0(r))\right.$$
$$\left.+\frac{r}{P_0(r)(P_0(r)+\rho_0(r))}(P_0'(r))^2\right]$$
$$=\eta(r)\left[4\pi(P_0(r)+\rho_0(r))r e^{\lambda_0(r)}+\frac{\rho_0(r)}{P_0(r)(P_0(r)+\rho_0(r))}P_0'(r)\right]+\eta'(r). \tag{B.52}$$

Note that we have used Eqs. (B.4), (B.5) and

$$\eta(r)=\frac{\Delta P(r)}{P_0(r)} \tag{B.53}$$

$$\eta'(r)=\left(\frac{\Delta P(r)}{P_0(r)}\right)'$$
$$=\frac{1}{P_0(r)}(\Delta P(r))'-\frac{\Delta P(r)}{P_0^2(r)}P_0'(r)$$
$$=\frac{1}{P_0(r)}(\Delta P(r))'-\frac{1}{P_0(r)}\eta(r)P_0'(r), \tag{B.54}$$

then we could rearrange Eq. (B.52) by making $\eta'(r)$ as a subject

$$\eta'(r)=\xi(r)\left[\omega^2 r e^{\lambda_0(r)-\nu_0(r)}\frac{(P_0(r)+\rho_0(r))}{P_0(r)}-\frac{4}{P_0(r)}P_0'(r)\right]$$
$$+\xi(r)\left[\frac{r}{P_0(r)(P_0(r)+\rho_0(r))}(P_0'(r))^2-8\pi r e^{\lambda_0(r)}(P_0(r)+\rho_0(r))\right]$$
$$-\eta(r)\left[4\pi(P_0(r)+\rho_0(r))r e^{\lambda_0(r)}+\frac{\rho_0(r)}{P_0(r)(P_0(r)+\rho_0(r))}P_0'(r)\right] \tag{B.55}$$

or alternatively,

$$\frac{1}{P_0(r)}(\Delta P(r))'=\xi(r)\left[\omega^2 r e^{\lambda_0(r)-\nu_0(r)}\frac{(P_0(r)+\rho_0(r))}{P_0(r)}-\frac{4}{P_0(r)}P_0'(r)\right]$$
$$+\xi(r)\left[\frac{r}{P_0(r)(P_0(r)+\rho_0(r))}(P_0'(r))^2-8\pi r e^{\lambda_0(r)}(P_0(r)+\rho_0(r))\right]$$
$$+\frac{\Delta P(r)}{P_0(r)}\left[-4\pi(P_0(r)+\rho_0(r))r e^{\lambda_0(r)}+\left(\frac{1}{P_0(r)}-\frac{\rho_0(r)}{P_0(r)(P_0(r)+\rho_0(r))}\right)P_0'(r)\right].$$
$$\tag{B.56}$$

Therefore, the 2nd fundamental equation for radial pulsations, as expressed in terms of $\Delta P(r)$ as described in Eq. (7.2), is

$$(\Delta P(r))'=\xi(r)\left[\omega^2 r e^{\lambda_0(r)-\nu_0(r)}(P_0(r)+\rho_0(r))-4P_0'(r)\right]$$
$$+\xi(r)\left[(P_0'(r))^2\frac{r}{(P_0(r)+\rho_0(r))}-8\pi r e^{\lambda_0(r)}(P_0(r)+\rho_0(r))P_0(r)\right]$$
$$+\Delta P(r)\left[P_0'(r)\frac{1}{(P_0(r)+\rho_0(r))}-4\pi r e^{\lambda_0(r)}(P_0(r)+\rho_0(r))\right].$$

Bibliography

[1]   Eemeli Annala et al. "Evidence for quark-matter cores in massive neutron stars". In: *Nature Phys.* 16.9 (2020), pp. 907–910. DOI: 10.1038/s41567-020-0914-9. arXiv: 1903.09121 [astro-ph.HE].

[2]   Paul Demorest et al. "Shapiro Delay Measurement of A Two Solar Mass Neutron Star". In: *Nature* 467 (2010), pp. 1081–1083. DOI: 10.1038/nature09466. arXiv: 1010.5788 [astro-ph.HE].

[3]   John Antoniadis et al. "A Massive Pulsar in a Compact Relativistic Binary". In: *Science* 340 (2013), p. 6131. DOI: 10.1126/science.1233232. arXiv: 1304.6875 [astro-ph.HE].

[4]   P. Burikham, Auttakit Chatrabhuti, and E. Hirunsirisawat. "Exotic Multi-quark States in the Deconfined Phase from Gravity Dual Models". In: *JHEP* 05 (2009), p. 006. DOI: 10.1088/1126-6708/2009/05/006. arXiv: 0811.0243 [hep-ph].

[5]   P. Burikham, E. Hirunsirisawat, and S. Pinkanjanarod. "Thermodynamic Properties of Holographic Multiquark and the Multiquark Star". In: *JHEP* 06 (2010), p. 040. DOI: 10.1007/JHEP06(2010)040. arXiv: 1003.5470 [hep-ph].

[6]   Richard C. Tolman. "Effect of imhomogeneity on cosmological models". In: *Proc. Nat. Acad. Sci.* 20 (1934), pp. 169–176. DOI: 10.1073/pnas.20.3.169.

[7]   J. R. Oppenheimer and G. M. Volkoff. "On massive neutron cores". In: *Phys. Rev.* 55 (1939), pp. 374–381. DOI: 10.1103/PhysRev.55.374.

[8]   Subrahmanyan Chandrasekhar. "The maximum mass of ideal white dwarfs". In: *Astrophys. J.* 74 (1931), pp. 81–82. DOI: 10.1086/143324.

[9]   Feryal Ozel et al. "On the Mass Distribution and Birth Masses of Neutron Stars". In: *Astrophys. J.* 757 (2012), p. 55. DOI: 10.1088/0004-637X/757/1/55. arXiv: 1201.1006 [astro-ph.HE].

[10] N. Chamel et al. "On the Maximum Mass of Neutron Stars". In: *Int. J. Mod. Phys. E* 22 (2013), p. 1330018. DOI: 10.1142/S021830131330018X. arXiv: 1307.3995 [astro-ph.HE].

[11] Luciano Rezzolla, Elias R. Most, and Lukas R. Weih. "Using gravitational-wave observations and quasi-universal relations to constrain the maximum mass of neutron stars". In: *Astrophys. J. Lett.* 852.2 (2018), p. L25. DOI: 10.3847/2041-8213/aaa401. arXiv: 1711.00314 [astro-ph.HE].

[12]   H. T. Cromartie et al. "Relativistic Shapiro delay measurements of an extremely massive millisecond pulsar". In: *Nature Astron.* 4.1 (2019), pp. 72–76. DOI: `10.1038/s41550-019-0880-2`. arXiv: `1904.06759 [astro-ph.HE]`.

[13]   B. P. Abbott et al. "GW170817: Observation of Gravitational Waves from a Binary Neutron Star Inspiral". In: *Phys. Rev. Lett.* 119.16 (2017), p. 161101. DOI: `10.1103/PhysRevLett.119.161101`. arXiv: `1710.05832 [gr-qc]`.

[14]   B. P. Abbott et al. "GW170817: Measurements of neutron star radii and equation of state". In: *Phys. Rev. Lett.* 121.16 (2018), p. 161101. DOI: `10.1103/PhysRevLett.121.161101`. arXiv: `1805.11581 [gr-qc]`.

[15]   I. Tews et al. "Neutron matter at next-to-next-to-next-to-leading order in chiral effective field theory". In: *Phys. Rev. Lett.* 110.3 (2013), p. 032504. DOI: `10.1103/PhysRevLett.110.032504`. arXiv: `1206.0025 [nucl-th]`.

[16]   Jens O. Andersen et al. "Three-loop HTL QCD thermodynamics". In: *JHEP* 08 (2011), p. 053. DOI: `10.1007/JHEP08(2011)053`. arXiv: `1103.2528 [hep-ph]`.

[17]   Sylvain Mogliacci et al. "Equation of State of hot and dense QCD: Resummed perturbation theory confronts lattice data". In: *JHEP* 12 (2013), p. 055. DOI: `10.1007/JHEP12(2013)055`. arXiv: `1307.8098 [hep-ph]`.

[18]   Roel Aaij et al. "Observation of structure in the J/ψ -pair mass spectrum". In: *Sci. Bull.* 65.23 (2020), pp. 1983–1993. DOI: `10.1016/j.scib.2020.08.032`. arXiv: `2006.16957 [hep-ex]`.

[19]   S. S. Gubser, Igor R. Klebanov, and Alexander M. Polyakov. "Gauge theory correlators from noncritical string theory". In: *Phys. Lett. B* 428 (1998), pp. 105–114. DOI: `10.1016/S0370-2693(98)00377-3`. arXiv: `hep-th/9802109`.

[20]   Juan Martin Maldacena. "The Large N limit of superconformal field theories and supergravity". In: *Adv. Theor. Math. Phys.* 2 (1998), pp. 231–252. DOI: `10.1023/A:1026654312961`. arXiv: `hep-th/9711200`.

[21]   Edward Witten. "Anti-de Sitter space, thermal phase transition, and confinement in gauge theories". In: *Adv. Theor. Math. Phys.* 2 (1998). Ed. by L. Bergstrom and U. Lindstrom, pp. 505–532. DOI: `10.4310/ATMP.1998.v2.n3.a3`. arXiv: `hep-th/9803131`.

[22]   Edward Witten. "Baryons and branes in anti-de Sitter space". In: *JHEP* 07 (1998), p. 006. DOI: `10.1088/1126-6708/1998/07/006`. arXiv: `hep-th/9805112`.

[23]   Curtis G. Callan Jr., Alberto Guijosa, and Konstantin G. Savvidy. "Baryons and string creation from the five-brane world volume action". In: *Nucl. Phys. B* 547 (1999), pp. 127–142. DOI: `10.1016/S0550-3213(99)00057-7`. arXiv: `hep-th/9810092`.

[24] A. Brandhuber et al. "Baryons from supergravity". In: *JHEP* 07 (1998), p. 020. DOI: `10.1088/1126-6708/1998/07/020`. arXiv: `hep-th/9806158`.

[25] Theodoros Nakas and Konstantinos S. Rigatos. "Fermions and baryons as open-string states from brane junctions". In: *JHEP* 12 (2020), p. 157. DOI: `10.1007/JHEP12(2020)157`. arXiv: `2010.00025 [hep-th]`.

[26] Tadakatsu Sakai and Shigeki Sugimoto. "Low energy hadron physics in holographic QCD". In: *Prog. Theor. Phys.* 113 (2005), pp. 843–882. DOI: `10.1143/PTP.113.843`. arXiv: `hep-th/0412141`.

[27] Tadakatsu Sakai and Shigeki Sugimoto. "More on a holographic dual of QCD". In: *Prog. Theor. Phys.* 114 (2005), pp. 1083–1118. DOI: `10.1143/PTP.114.1083`. arXiv: `hep-th/0507073`.

[28] Ofer Aharony, Jacob Sonnenschein, and Shimon Yankielowicz. "A Holographic model of deconfinement and chiral symmetry restoration". In: *Annals Phys.* 322 (2007), pp. 1420–1443. DOI: `10.1016/j.aop.2006.11.002`. arXiv: `hep-th/0604161`.

[29] Oren Bergman, Gilad Lifschytz, and Matthew Lippert. "Holographic Nuclear Physics". In: *JHEP* 11 (2007), p. 056. DOI: `10.1088/1126-6708/2007/11/056`. arXiv: `0708.0326 [hep-th]`.

[30] Thierry Mora and Clifford M. Will. "A PostNewtonian diagnostic of quasiequilibrium binary configurations of compact objects". In: *Phys. Rev. D* 69 (2004). [Erratum: Phys.Rev.D 71, 129901 (2005)], p. 104021. DOI: `10.1103/PhysRevD.71.129901`. arXiv: `gr-qc/0312082`.

[31] Emanuele Berti, Sai Iyer, and Clifford M. Will. "A Post-Newtonian diagnosis of quasiequilibrium configurations of neutron star-neutron star and neutron star-black hole binaries". In: *Phys. Rev. D* 77 (2008), p. 024019. DOI: `10.1103/PhysRevD.77.024019`. arXiv: `0709.2589 [gr-qc]`.

[32] Eanna E. Flanagan and Tanja Hinderer. "Constraining neutron star tidal Love numbers with gravitational wave detectors". In: *Phys. Rev. D* 77 (2008), p. 021502. DOI: `10.1103/PhysRevD.77.021502`. arXiv: `0709.1915 [astro-ph]`.

[33] Tanja Hinderer. "Tidal Love numbers of neutron stars". In: *Astrophys. J.* 677 (2008), pp. 1216–1220. DOI: `10.1086/533487`. arXiv: `0711.2420 [astro-ph]`.

[34] Eemeli Annala et al. "Holographic compact stars meet gravitational wave constraints". In: *JHEP* 12 (2018), p. 078. DOI: `10.1007/JHEP12(2018)078`. arXiv: `1711.06244 [astro-ph.HE]`.

[35] Niko Jokela, Matti Järvinen, and Jere Remes. "Holographic QCD in the Veneziano limit and neutron stars". In: *JHEP* 03 (2019), p. 041. DOI: 10.1007/JHEP03(2019)041. arXiv: 1809.07770 [hep-ph].

[36] Kilar Zhang et al. "Compact Star of Holographic Nuclear Matter and GW170817". In: *Phys. Lett. B* 801 (2020), p. 135176. DOI: 10.1016/j.physletb.2019.135176. arXiv: 1902.08477 [hep-ph].

[37] Niko Jokela et al. "Unified weak and strong coupling framework for nuclear matter and neutron stars". In: *Phys. Rev. D* 103.8 (2021), p. 086004. DOI: 10.1103/PhysRevD.103.086004. arXiv: 2006.01141 [hep-ph].

[38] R. Abbott et al. "GW190814: Gravitational Waves from the Coalescence of a 23 Solar Mass Black Hole with a 2.6 Solar Mass Compact Object". In: *Astrophys. J. Lett.* 896.2 (2020), p. L44. DOI: 10.3847/2041-8213/ab960f. arXiv: 2006.12611 [astro-ph.HE].

[39] Shun Furusawa et al. "Supernova equations of state including full nuclear ensemble with in-medium effects". In: *Nucl. Phys. A* 957 (2017), pp. 188–207. DOI: 10.1016/j.nuclphysa.2016.09.002. arXiv: 1612.01852 [nucl-th].

[40] Shun Furusawa et al. "New equations of state based on the liquid drop model of heavy nuclei and quantum approach to light nuclei for core-collapse supernova simulations". In: *Astrophys. J.* 772 (2013), p. 95. DOI: 10.1088/0004-637X/772/2/95. arXiv: 1305.1508 [astro-ph.HE].

[41] Shun Furusawa et al. "A new baryonic equation of state at sub-nuclear densities for core-collapse simulations". In: *Astrophys. J.* 738 (2011), p. 178. DOI: 10.1088/0004-637X/738/2/178. arXiv: 1103.6129 [astro-ph.HE].

[42] R. P. Feynman, N. Metropolis, and E. Teller. "Equations of State of Elements Based on the Generalized Fermi-Thomas Theory". In: *Phys. Rev.* 75 (1949), pp. 1561–1573. DOI: 10.1103/PhysRev.75.1561.

[43] Gordon Baym, Christopher Pethick, and Peter Sutherland. "The Ground state of matter at high densities: Equation of state and stellar models". In: *Astrophys. J.* 170 (1971), pp. 299–317. DOI: 10.1086/151216.

[44] Gordon Baym, Hans A. Bethe, and Christopher Pethick. "Neutron star matter". In: *Nucl. Phys. A* 175 (1971), pp. 225–271. DOI: 10.1016/0375-9474(71)90281-8.

[45] K. Hebeler et al. "Equation of state and neutron star properties constrained by nuclear physics and observation". In: *Astrophys. J.* 773 (2013), p. 11. DOI: 10.1088/0004-637X/773/1/11. arXiv: 1303.4662 [astro-ph.SR].

[46] E. E. Salpeter. "Energy and Pressure of a Zero-Temperature Plasma". In: *Astrophys. J.* 134 (1961), pp. 669–682. DOI: 10.1086/147194.

[47]   Rosemary A. Coldwell-Horsfall and Alexei A. Maradudin. "Zero-Point Energy of an Electron Lattice". In: *Journal of Mathematical Physics* 1.5 (Sept. 1960), pp. 395–404. DOI: 10.1063/1.1703670.

[48]   Freeman J Dyson. "Chemical binding in classical Coulomb lattices". In: *Annals of Physics* 63.1 (1971), pp. 1–11. ISSN: 0003-4916. DOI: https://doi.org/10.1016/0003-4916(71)90294-6. URL: https://www.sciencedirect.com/science/article/pii/0003491671902946.

[49]   John W. Negele and D. Vautherin. "Neutron star matter at subnuclear densities". In: *Nucl. Phys. A* 207 (1973), pp. 298–320. DOI: 10.1016/0375-9474(73)90349-7.

[50]   Jr. Reid Roderick V. "Local phenomenological nucleon-nucleon potentials". In: *Annals of Physics* 50.3 (Dec. 1968), pp. 411–448. DOI: 10.1016/0003-4916(68)90126-7.

[51]   F. Coester et al. "Variation in Nuclear-Matter Binding Energies with Phase-Shift-Equivalent Two-Body Potentials". In: *Phys. Rev. C* 1 (1970), pp. 769–776. DOI: 10.1103/PhysRevC.1.769.

[52]   T. K. Dahlblom. "THREE-BODY CORRELATIONS IN NUCLEAR MATTER WITH PHENOMENOLOGICAL NUCLEON-NUCLEON POTENTIALS". In: (Sept. 1969).

[53]   B. D. Day. "Four-Hole-Line Diagrams in Nuclear Matter". In: *Physical Review* 187.4 (Nov. 1969), pp. 1269–1301. DOI: 10.1103/PhysRev.187.1269.

[54]   G. E. Brown and A. M. Green. "Three-body forces in nuclear matter". In: *Nucl. Phys. A* 137 (1969), pp. 1–19. DOI: 10.1016/0375-9474(69)90068-2.

[55]   Philip J. Siemens. "Nuclear-matter reaction matrix". In: *Nuclear Physics A* 141.2 (1970), pp. 225–248. ISSN: 0375-9474. DOI: https://doi.org/10.1016/0375-9474(70)90844-4. URL: https://www.sciencedirect.com/science/article/pii/0375947470908444.

[56]   Philip Siemens. "New Statistical Theory of the Nuclear Surface. I". In: *Phys. Rev. C* 1 (Jan. 1970). DOI: 10.1103/PhysRevC.1.98.

[57]   H. Bethe. "Thomas-Fermi Theory of Nuclei". In: *Physical Review - PHYS REV X* 167 (Mar. 1968), pp. 879–907. DOI: 10.1103/PhysRev.167.879.

[58]   H. Bethe and R. Bacher. "Nuclear Physics A. Stationary States of Nuclei". In: *Reviews of Modern Physics - REV MOD PHYS* 8 (Jan. 1936), pp. 82–229. DOI: 10.1103/RevModPhys.8.82.

[59]   Freeman J Dyson. "Chemical binding in classical Coulomb lattices". In: *Annals of Physics* 63.1 (1971), pp. 1–11. ISSN: 0003-4916. DOI: https://doi.org/10.1016/0003-4916(71)90294-6.

[60] K. Hebeler and A. Schwenk. "Chiral three-nucleon forces and neutron matter". In: *Phys. Rev. C* 82 (2010), p. 014314. DOI: `10.1103/PhysRevC.82.014314`. arXiv: `0911.0483 [nucl-th]`.

[61] S. Gandolfi, J. Carlson, and Sanjay Reddy. "The maximum mass and radius of neutron stars and the nuclear symmetry energy". In: *Phys. Rev. C* 85 (2012), p. 032801. DOI: `10.1103/PhysRevC.85.032801`. arXiv: `1101.1921 [nucl-th]`.

[62] M. H. van Kerkwijk, R. Breton, and S. R. Kulkarni. "Evidence for a Massive Neutron Star from a Radial-Velocity Study of the Companion to the Black Widow Pulsar PSR B1957+20". In: *Astrophys. J.* 728 (2011), p. 95. DOI: `10.1088/0004-637X/728/2/95`. arXiv: `1009.5427 [astro-ph.HE]`.

[63] M. Tanabashi et al. "Review of Particle Physics". In: *Phys. Rev. D* 98.3 (2018), p. 030001. DOI: `10.1103/PhysRevD.98.030001`.

[64] Marek Gaździcki and Mark I. Gorenstein. "Hagedorn's Hadron Mass Spectrum and the Onset of Deconfinement". In: *Melting Hadrons, Boiling Quarks - From Hagedorn Temperature to Ultra-Relativistic Heavy-Ion Collisions at CERN: With a Tribute to Rolf Hagedorn.* Ed. by Johann Rafelski. 2016, pp. 87–92. DOI: `10.1007/978-3-319-17545-4_11`. arXiv: `1502.07684 [nucl-th]`.

[65] R. Machleidt and D. R. Entem. "Chiral effective field theory and nuclear forces". In: *Phys. Rept.* 503 (2011), pp. 1–75. DOI: `10.1016/j.physrep.2011.02.001`. arXiv: `1105.2919 [nucl-th]`.

[66] Edwin Laermann and Owe Philipsen. "The Status of lattice QCD at finite temperature". In: *Ann. Rev. Nucl. Part. Sci.* 53 (2003), pp. 163–198. DOI: `10.1146/annurev.nucl.53.041002.110609`. arXiv: `hep-ph/0303042`.

[67] Shigeki Sugimoto. "Holographic QCD: Status and perspectives for the future". In: *PoS* ConfinementX (2012). Ed. by Matthias Berwein, Nora Brambilla, and Stephan Paul, p. 010. DOI: `10.22323/1.171.0010`.

[68] Youngman Kim, Ik Jae Shin, and Takuya Tsukioka. "Holographic QCD: Past, Present, and Future". In: *Prog. Part. Nucl. Phys.* 68 (2013), pp. 55–112. DOI: `10.1016/j.ppnp.2012.09.002`. arXiv: `1205.4852 [hep-ph]`.

[69] David J. Gross and Hirosi Ooguri. "Aspects of large N gauge theory dynamics as seen by string theory". In: *Phys. Rev. D* 58 (1998), p. 106002. DOI: `10.1103/PhysRevD.58.106002`. arXiv: `hep-th/9805129`.

[70] D. T. Son and M. A. Stephanov. "QCD and dimensional deconstruction". In: *Phys. Rev. D* 69 (2004), p. 065020. DOI: `10.1103/PhysRevD.69.065020`. arXiv: `hep-ph/0304182`.

[71] Michael R. Douglas. "Branes within branes". In: *NATO Sci. Ser. C* 520 (1999). Ed. by L. Baulieu et al., pp. 267–275. arXiv: `hep-th/9512077`.

[72] T. H. R. Skyrme. "A Nonlinear field theory". In: *Proc. Roy. Soc. Lond. A* 260 (1961), pp. 127–138. DOI: `10.1098/rspa.1961.0018`.

[73] M. F. Atiyah and N. S. Manton. "Skyrmions From Instantons". In: *Phys. Lett. B* 222 (1989), pp. 438–442. DOI: `10.1016/0370-2693(89)90340-7`.

[74] Gregory S. Adkins, Chiara R. Nappi, and Edward Witten. "Static Properties of Nucleons in the Skyrme Model". In: *Nucl. Phys. B* 228 (1983), p. 552. DOI: `10.1016/0550-3213(83)90559-X`.

[75] Norio Horigome and Yoshiaki Tanii. "Holographic chiral phase transition with chemical potential". In: *JHEP* 01 (2007), p. 072. DOI: `10.1088/1126-6708/2007/01/072`. arXiv: `hep-th/0608198`.

[76] Keun-Young Kim, Sang-Jin Sin, and Ismail Zahed. "Dense and Hot Holographic QCD: Finite Baryonic E Field". In: *JHEP* 07 (2008), p. 096. DOI: `10.1088/1126-6708/2008/07/096`. arXiv: `0803.0318 [hep-th]`.

[77] K. Hebeler et al. "Constraints on neutron star radii based on chiral effective field theory interactions". In: *Phys. Rev. Lett.* 105 (2010), p. 161102. DOI: `10.1103/PhysRevLett.105.161102`. arXiv: `1007.1746 [nucl-th]`.

[78] Sitthichai Pinkanjanarod and Piyabut Burikham. "Massive neutron stars with holographic multiquark cores". In: *Eur. Phys. J. C* 81.8 (2021), p. 705. DOI: `10.1140/epjc/s10052-021-09479-w`. arXiv: `2007.10615 [nucl-th]`.

[79] Carlos Hoyos et al. "Holographic quark matter and neutron stars". In: *Phys. Rev. Lett.* 117.3 (2016), p. 032501. DOI: `10.1103/PhysRevLett.117.032501`. arXiv: `1603.02943 [hep-ph]`.

[80] B. P. Abbott et al. "GW190425: Observation of a Compact Binary Coalescence with Total Mass $\sim 3.4 M_\odot$". In: *Astrophys. J. Lett.* 892.1 (2020), p. L3. DOI: `10.3847/2041-8213/ab75f5`. arXiv: `2001.01761 [astro-ph.HE]`.

[81] B. P. Abbott et al. "Properties of the binary neutron star merger GW170817". In: *Phys. Rev. X* 9.1 (2019), p. 011001. DOI: `10.1103/PhysRevX.9.011001`. arXiv: `1805.11579 [gr-qc]`.

[82] I. Arsene et al. "Quark gluon plasma and color glass condensate at RHIC? The Perspective from the BRAHMS experiment". In: *Nucl. Phys. A* 757 (2005), pp. 1–27. DOI: `10.1016/j.nuclphysa.2005.02.130`. arXiv: `nucl-ex/0410020`.

[83] Jaroslav Adam et al. "Enhanced production of multi-strange hadrons in high-multiplicity proton-proton collisions". In: *Nature Phys.* 13 (2017), pp. 535–539. DOI: `10.1038/nphys4111`. arXiv: `1606.07424 [nucl-ex]`.

[84] Mark G. Alford et al. "Color superconductivity in dense quark matter". In: *Rev. Mod. Phys.* 80 (2008), pp. 1455–1515. DOI: `10.1103/RevModPhys.80.1455`. arXiv: `0709.4635 [hep-ph]`.

[85] Robert L. Jaffe. "Perhaps a Stable Dihyperon". In: *Phys. Rev. Lett.* 38 (1977). [Erratum: Phys.Rev.Lett. 38, 617 (1977)], pp. 195–198. DOI: `10.1103/PhysRevLett.38.195`.

[86] Piyabut Burikham and Tossaporn Chullaphan. "Holographic Magnetic Star". In: *JHEP* 06 (2012), p. 021. DOI: `10.1007/JHEP06(2012)021`. arXiv: `1203.0883 [hep-th]`.

[87] Jeremy W. Holt, Mannque Rho, and Wolfram Weise. "Chiral symmetry and effective field theories for hadronic, nuclear and stellar matter". In: *Phys. Rept.* 621 (2016), pp. 2–75. DOI: `10.1016/j.physrep.2015.10.011`. arXiv: `1411.6681 [nucl-th]`.

[88] Madappa Prakash et al. "Composition and structure of protoneutron stars". In: *Phys. Rept.* 280 (1997), pp. 1–77. DOI: `10.1016/S0370-1573(96)00023-3`. arXiv: `nucl-th/9603042`.

[89] Jose A. Pons et al. "Evolution of protoneutron stars with quarks". In: *Phys. Rev. Lett.* 86 (2001), pp. 5223–5226. DOI: `10.1103/PhysRevLett.86.5223`. arXiv: `astro-ph/0102015`.

[90] Sitthichai Pinkanjanarod, Piyabut Burikham, and Supakchai Ponglertsakul. "Tidal deformation and radial pulsations of neutron star with holographic multiquark core". In: *Eur. Phys. J. C* 82.2 (2022), p. 141. DOI: `10.1140/epjc/s10052-022-10106-5`. arXiv: `2106.13450 [gr-qc]`.

[91] A.E.H. Love. In: *Some Problems of Geodynamics*. Cambridge University Press, 1911.

[92] Carl D. Murray and Stanley F. Dermott. "Tides, Rotation, and Shape". In: *Solar System Dynamics*. Cambridge University Press, 2000, pp. 130–188. DOI: `10.1017/CBO9781139174817.005`.

[93] Taylor Binnington and Eric Poisson. "Relativistic theory of tidal Love numbers". In: *Phys. Rev. D* 80 (2009), p. 084018. DOI: `10.1103/PhysRevD.80.084018`. arXiv: `0906.1366 [gr-qc]`.

[94] Andrea Sabatucci. "Tidal deformation of neutron stars". Unpublished Bachelor Thesis, Facoltà di Scienze Matematiche, Fisiche e Naturali, Università di Roma. 2017.

[95] Kip S. Thorne. "Tidal stabilization of rigidly rotating, fully relativistic neutron stars". In: *Phys. Rev. D* 58 (1998), p. 124031. DOI: `10.1103/PhysRevD.58.124031`. arXiv: `gr-qc/9706057`.

[96]   Carolyn Raithel, Feryal Özel, and Dimitrios Psaltis. "Tidal deformability from GW170817 as a direct probe of the neutron star radius". In: *Astrophys. J. Lett.* 857.2 (2018), p. L23. DOI: 10.3847/2041-8213/aabcbf. arXiv: 1803.07687 [astro-ph.HE].

[97]   Tullio Regge and John A. Wheeler. "Stability of a Schwarzschild singularity". In: *Phys. Rev.* 108 (1957), pp. 1063–1069. DOI: 10.1103/PhysRev.108.1063.

[98]   Tanja Hinderer et al. "Tidal deformability of neutron stars with realistic equations of state and their gravitational wave signatures in binary inspiral". In: *Phys. Rev. D* 81 (2010), p. 123016. DOI: 10.1103/PhysRevD.81.123016. arXiv: 0911.3535 [astro-ph.HE].

[99]   Kip S. Thorne and Alfonso Campolattaro. "Non-Radial Pulsation of General-Relativistic Stellar Models. I. Analytic Analysis for L >= 2". In: *Apj* 149 (Sept. 1967), p. 591. DOI: 10.1086/149288.

[100] R. Abbott et al. "Observation of Gravitational Waves from Two Neutron Star–Black Hole Coalescences". In: *Astrophys. J. Lett.* 915.1 (2021), p. L5. DOI: 10.3847/2041-8213/ac082e. arXiv: 2106.15163 [astro-ph.HE].

[101] Kent Yagi and Nicolas Yunes. "I-Love-Q". In: *Science* 341 (2013), pp. 365–368. DOI: 10.1126/science.1236462. arXiv: 1302.4499 [gr-qc].

[102] S. Chandrasekhar. "The Dynamical Instability of Gaseous Masses Approaching the Schwarzschild Limit in General Relativity". In: *Astrophys. J.* 140 (1964). [Erratum: Astrophys.J. 140, 1342 (1964)], pp. 417–433. DOI: 10.1086/147938.

[103] G. Chanmugam. "Radial oscillations of zero-temperature white dwarfs and neutron stars below nuclear densities." In: *Apj* 217 (Nov. 1977), pp. 799–808. DOI: 10.1086/155627.

[104] D. Gondek, P. Haensel, and J. L. Zdunik. "Radial pulsations and stability of protoneutron stars". In: *Astron. Astrophys.* 325 (1997), pp. 217–227. arXiv: astro-ph/9705157.

[105] J." "Cox. In: *Theory of Stellar Pulsations.* Princeton University Press, 1980.

[106] J. S. Clark et al. "Physical parameters of the high-mass X-ray binary 4U1700-37". In: *Astron. Astrophys.* 392 (2002), pp. 909–920. DOI: 10.1051/0004-6361:20021184. arXiv: astro-ph/0207334.

[107] Roger W. Romani et al. "PSR J1311-3430: A Heavyweight Neutron Star with a Flyweight Helium Companion". In: *Astrophys. J. Lett.* 760 (2012), p. L36. DOI: 10.1088/2041-8205/760/2/L36. arXiv: 1210.6884 [astro-ph.HE].

[108] Roger W. Romani. "2FGL J1311.7-3429 Joins the Black Widow Club". In: *Astrophys. J. Lett.* 754 (2012), p. L25. DOI: 10.1088/2041-8205/754/2/L25. arXiv: 1207.1736 [astro-ph.HE].

[109] Manuel Linares, Tariq Shahbaz, and Jorge Casares. "Peering into the dark side: Magnesium lines establish a massive neutron star in PSR J2215+5135". In: *Astrophys. J.* 859.1 (2018), p. 54. DOI: 10.3847/1538-4357/aabde6. arXiv: 1805.08799 [astro-ph.HE].

[110] Varun Bhalerao, Marten H van Kerkwijk, and Fiona Harrison. "Constraints on the Compact Object Mass in the Eclipsing HMXB XMMU J013236.7+303228 in M33". In: *Astrophys. J.* 757 (2012), p. 10. DOI: 10.1088/0004-637X/757/1/10. arXiv: 1207.0008 [astro-ph.SR].

[111] David J. Nice et al. "A 2.1 solar mass pulsar measured by relativistic orbital decay". In: *Astrophys. J.* 634 (2005), pp. 1242–1249. DOI: 10.1086/497109. arXiv: astro-ph/0508050.

[112] Paulo Cesar Carvalho Freire. "Super-Massive Neutron Stars". In: *AIP Conf. Proc.* 983.1 (2008). Ed. by Cees G. Bassa et al., pp. 459–463. DOI: 10.1063/1.2900274. arXiv: 0712.0024 [astro-ph].

[113] H. Quaintrell et al. "The mass of the neutron star in Vela X-1 and tidally induced non-radial oscillations in GP Vel". In: *Astron. Astrophys.* 401 (2003), pp. 313–324. DOI: 10.1051/0004-6361:20030120. arXiv: astro-ph/0301243.

[114] Kazem Bitaghsir Fadafan, Jesus Cruz Rojas, and Nick Evans. "Holographic description of color superconductivity". In: *Phys. Rev. D* 98.6 (2018), p. 066010. DOI: 10.1103/PhysRevD.98.066010. arXiv: 1803.03107 [hep-ph].

[115] Kazem Bitaghsir Fadafan, Jesús Cruz Rojas, and Nick Evans. "Holographic quark matter with colour superconductivity and a stiff equation of state for compact stars". In: *Phys. Rev. D* 103.2 (2021), p. 026012. DOI: 10.1103/PhysRevD.103.026012. arXiv: 2009.14079 [hep-ph].

Vitae

Mr Sitthichai Pinkanjanarod was born on March 13rd, 1980, and received his Bachelor's degree in Physics with honours from Kasetsart University in 2001. He received his Master's degree in Physics from Chulalongkorn University in 2010. His thesis's title for his Master's degree is the "Holographic Description of a Multiquark Star". His research interests are in theoretical elementary particle physics, especially in the area of Superstrings phenomenology and Astrophysics.

This thesis is his Ph.D. dissertation based on the following publications.

List of publications

1. S. Pinkanjanarod and P. Burikham,"Massive neutron stars with holographic multiquark cores", **Eur. Phys. J. C 81**, 8, 705 (2021) [arXiv:2007.10615 [nucl-th]].

2. S. Pinkanjanarod, P. Burikham and S. Ponglertsakul, "Tidal Deformation and Radial Pulsations of Neutron Star with Holographic Multiquark Core", **Eur. Phys. J. C 82**, 2, 141 (2022) [arXiv: 2106.13450 [gr-qc]].